TOPOLOGY OPTIMIZATION OF NON-LINEAR ELASTIC MICROSTRUCTURES

A Thesis Submitted to
the Graduate School of
İzmir Institute of Technology
in Partial Fulfillment of the Requirements for the Degree of

MASTER OF SCIENCE

in Civil Engineering

by
Murat GÜVEN

July 2023
İZMİR

We approve the thesis of **Murat GÜVEN**

Examining Committee Members:

Assoc. Prof. Dr. İzzet ÖZDEMİR
Department of Civil Engineering, IZTECH

Assoc. Prof. Dr. Çağlayan HIZAL
Department of Civil Engineering, Ege University

Asst. Prof. Dr. Selçuk SAATCI
Department of Civil Engineering, IZTECH

13 July 2023

Assoc. Prof. Dr. İzzet ÖZDEMİR
Supervisor, Department of Civil Engineering, IZTECH

Prof. Dr. Cemalettin DÖNMEZ
Head of the Department of
Civil Engineering

Prof. Dr. Mehtap EANES
Dean of the Graduate School

ACKNOWLEDGMENTS

First, I would like to express my most heartfelt gratitude to my supervisor Assoc. Prof. Dr. İzzet Özdemir, for his never-ending support, wisdom, and guidance throughout this study. I am truly fortunate to have the opportunity to work under his supervision, and I am deeply grateful for his mentorship.

I also want to thank my thesis committee members, Assoc. Prof. Dr. Çağlayan Hızal and Asst. Prof. Dr. Selçuk Saatcı for their precious comments on my thesis.

The numerical calculations reported in this thesis were partially performed at TUBITAK ULAKBIM, High Performance and Grid Computing Center (TRUBA resources). I am grateful to TUBITAK for providing the necessary infrastructure for the computations and financially supporting this thesis as a research project (Project No: 122M134). Furthermore, I want to thank Atakan Aydın for his exceptional work in producing the 3D-printed samples used in the experiments.

Last, but not least, I am profoundly grateful to my family for their unwavering love, understanding, and support throughout my life. Their encouragement, patience, and belief in me have been my constant source of motivation. I am forever indebted to them for the sacrifices they made and the values they have instilled in me.

ABSTRACT

TOPOLOGY OPTIMIZATION OF NON-LINEAR ELASTIC MICROSTRUCTURES

Topology optimization (TO) is used in a broad spectrum of engineering disciplines ranging from aerospace to civil engineering. A particular sub-field where topology optimization has been very instrumental is the design of microstructures that yield specific macroscopic properties, such as negative Poisson's ratio and negative magnetic permeability.

In this thesis, based on a recently proposed method for nonlinear homogenization, a framework for topology optimization of nonlinear elastic microstructures is developed and implemented as a computer program using the Julia programming language. Following a plane strain formulation, a two-dimensional unit cell with periodic boundary conditions is used in combination with a neo-Hookean elastic material response.

By exploiting the symmetry properties of the resulting orthotropic microstructure, it is shown that the computational domain can be reduced, and half of the original discretization is sufficient to carry out the optimization task. The obtained topologies from the developed computer program, the linear and nonlinear response comparison, and the computational gain achieved through domain reduction are presented along with the experiments on proof-of-concept type uni-axial tests.

ÖZET

DOĞRUSAL OLMAYAN ELASTİK MİKROYAPILARIN TOPOLOJİ OPTİMİZASYONU

Topoloji optimizasyonu (TO), havacılık ve uzay mühendisliğinden inşaat mühendisliğine kadar geniş bir yelpazede mühendislik disiplinlerinde kullanılmaktadır. Topoloji optimizasyonunun çok kullanışlı olduğu bir diğer alan da, negatif Poisson oranı ve negatif manyetik geçirgenlik gibi belirli makroskopik özellikler sağlayan mikroyapıların tasarımıdır.

Bu tezde, doğrusal olmayan homojenleştirme için yakın zamanda önerilen bir yönteme dayalı olarak, doğrusal olmayan elastik mikroyapıların topoloji optimizasyonu için bir çerçeve oluşturuldu ve Julia programlama dili kullanılarak bir bilgisayar programı geliştirildi. Periyodik sınır koşullarına sahip iki boyutlu bir birim hücre, düzlem gerinim ve neo-Hookean elastik malzeme davranışı gösterdiği varsayımıyla analizde kullanılmıştır.

Ortaya çıkan ortotropik mikroyapının simetri özelliklerinden yararlanılarak, çözüm alanının indirgenebileceği ve orijinal ayrıklaştırmanın yarısının optimizasyon görevini gerçekleştirmek için yeterli olduğu gösterilmiştir. Geliştirilen bilgisayar programından elde edilen topolojiler, doğrusal ve doğrusal olmayan davranışların karşılaştırması, çözüm alanının indirgenmesi yoluyla elde edilen hesaplama kazancı, sonuçların doğruluğunu gösteren tek eksenli deneyler ile beraber sunulmuştur.

This thesis is dedicated to my sister, Zeynep.

TABLE OF CONTENTS

LIST OF FIGURES

Figure **Page**

Figure **Page**

Figure **Page**

Figure **Page**

LIST OF TABLES

Table **Page**

LIST OF SYMBOLS

E, ν Modulus of elasticity, Poisson's ratio, respectively

ρ Relative density of microscopic constituents

$\mathbf{y}$, $\mathbf{X}$ Microscopic and macroscopic position vectors respectively

$\overline{\mathbf{u}}_m$ Macroscopic contribution on microscopic displacements

$\widetilde{\mathbf{u}}_m$ Microscopic displacement fluctuations

$\mathbf{u}_m$, $\mathbf{u}_M$ Microscopic total displacements, homogenized macroscopic total displacements, respectively

$\mathbf{F}_m, \mathbf{F}_M$ Microscopic and macroscopic deformation gradient, respectively

$\mathbf{x}_M, \mathbf{X}_M$ Point on a macroscopic body in deformed and undeformed configuration respectively

$\mathbf{P}_m, \mathbf{P}_M$ Microscopic and homogenized macroscopic 1^{st} Piola-Kirchhoff stress tensor respectively

$\mathbf{A}_m, \mathbf{A}_M$ Microscopic and homogenized macroscopic nominal stiffness tensor respectively

$\mathcal{H}(\cdot)$ Homogenization operator

$\nabla(\cdot)$ Gradient operator in Cartesian coordinates

$\nabla_y(\cdot), \nabla_x(\cdot)$ Gradient w.r.t. microscopic and macroscopic coordinates respectively

Ω_m, Ω_M Microscopic and macroscopic domain respectively

$\partial\Omega_m, \partial\Omega_M$ Boundary of the microscopic and macroscopic domain respectively

L_x, L_y Horizontal and vertical dimensions of the microstructure respectively

$\mathbf{e}_1, \mathbf{e}_2$ Unit basis vector along the horizontal and vertical direction respectively

P_m^{int}, P_M^{int} Microscopic and macroscopic internal virtual power respectively

$\chi_m^{(ij)}$ Microscopic incremental total displacements in the ij direction

$\otimes$ Tensor dyadic product

CHAPTER 1

INTRODUCTION

Environmental challenges caused by rapid development, industrialization, and urbanization in the current era made sustainability gain immense importance among all engineering practices. As a fundamental branch of engineering, civil engineering is one of the biggest contributors to pollution, producing unrecyclable waste and the over-consumption of limited natural resources. Therefore, civil engineering plays a crucial role in sustainable development by developing and implementing innovative techniques and strategies to address the ever-increasing demand for infrastructure in a sustainable way.

One of the most promising approaches for designing sustainable structures is through the use of Additive Manufacturing (AM) methods such as 3D printing (Javaid et al., 2021). Thanks to the versatility of additive manufacturing, many designs that were previously very complex or even impossible to manufacture can now be manufactured using AM with high accuracy, thus, reducing waste and improving resource utilization significantly. Additive manufacturing is considered one of the best ways to achieve sustainable manufacturing (Ford & Despeisse, 2016).

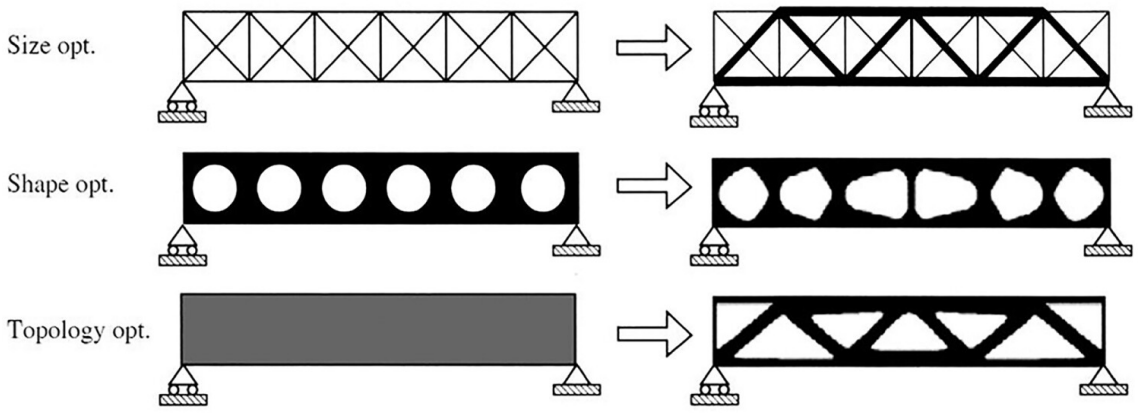

Figure 1.1: Illustrative examples of different structural optimization techniques; Size, shape, and topology optimization, respectively. Initial designs are on the left, and the final designs are on the right. (Source: Bendsøe and Sigmund, 2004)

Along with sustainability, design engineers must also take into account various design variables such as economy and reliability while designing structures. Unfortunately,

most of these variables have a trade-off relationship, e.g., building a reliable structure will often require forgoing the economic point of view. For this reason, engineers have developed various optimization methods to find the best possible structural designs with limited resources. These procedures are called structural optimization.

Structural optimization can be categorized into three parts (X. Zhang & Zhu, 2018): One of these methods is size optimization, which aims to find the optimal dimensions of a structural member. Similarly, shape optimization aims to identify the optimal geometry that a structural member should take. The third class of optimization problems, which is also the central theme of this thesis, is called topology optimization, and it deals with the distribution of limited material within a certain volume. These techniques are illustrated in 1.1.

Topology optimization is a design method used to find the optimal material distribution (topology) inside the design domain based on a given set of loads and design constraints. Topology optimization allows the creation of unique and efficient macroscale designs and has various applications, such as aircraft wings (Aage et al., 2017) and passive coolers (Alexandersen et al., 2018), please see Figure 1.2 and Figure 1.3, respectively.

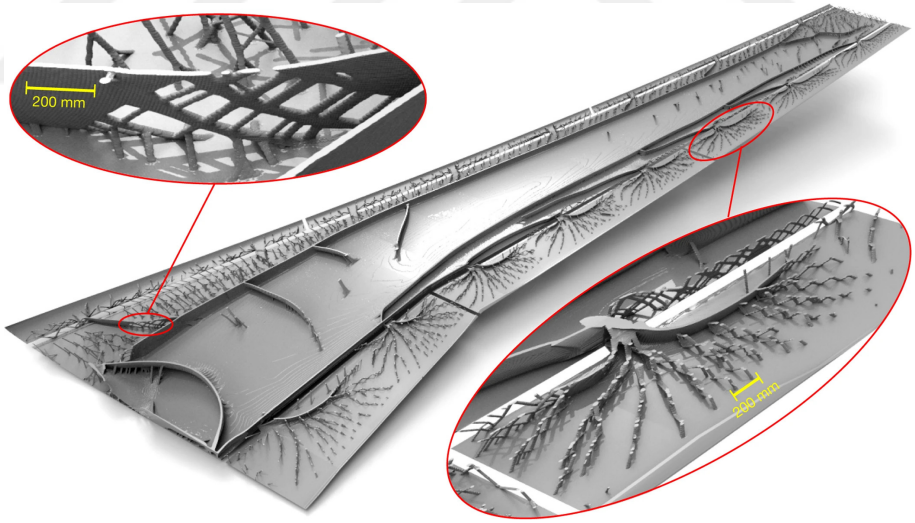

Figure 1.2: Topology optimized full-scale airplane wing. Apart from the wing shape, all internal structures, such as walls and curved spars, result from the optimization process (Source: Aage et al., 2017)

Another benefit of topology optimization is that it can also be used to design microscale structures. Using topology optimization, one can create materials that exhibit properties that do not exist or rarely exist in nature, called metamaterials. Materials with negative Poisson's ratio (Vogiatzis et al., 2017), negative thermal expansion coefficient

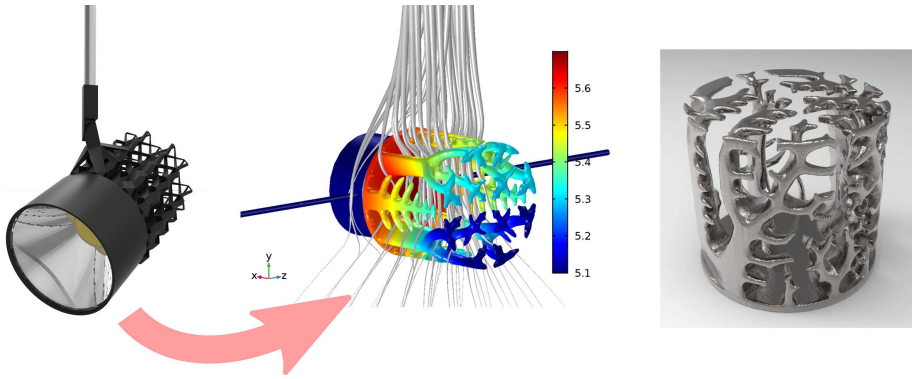

Figure 1.3: Topology optimized design for passive cooling of a light-emitting diode (LED) lamp (Source: Alexandersen et al., 2018)

(Sigmund & Torquato, 1997), and electromagnetic metamaterials with negative permeability (Diaz & Sigmund, 2009) can be given as examples of metamaterials. Microstructural topology optimization can also be used to create materials combining these properties (Y. Wang et al., 2016).

Most of the research in the literature has been focused on linear topology optimization due to its simplicity, ease of implementation, and the high computational power needed for nonlinear analysis (Kato et al., 2013; Zhu et al., 2017; M. M. Neves et al., 2002). For this reason, nonlinear topology optimization remained an untouched topic for a long time. As the computational power of computers increased and nonlinear topology optimization became feasible, nonlinear analysis gained more attention from researchers as it allowed for investigating the effect of geometric and material nonlinearities on the topologies of microstructures (Xia & Breitkopf, 2014).

Departing from this point, to explore this relatively untouched sub-field, this thesis aims to develop and implement a methodology to optimize the topology of nonlinear elastic microstructures using nonlinear homogenization and topology optimization techniques. The thesis consists of several chapters, each covering different aspects of topology optimization of nonlinear elastic microstructures. After the introduction, the second chapter investigates how microstructural topology optimization is conducted based on a top-down approach. The third chapter focuses on nonlinear homogenization, a technique used to evaluate the effective properties of a composite material from the properties of its constituent materials. The fourth chapter is dedicated to sensitivity analysis, focusing on how small perturbations in design variables affect the objective function and how this information is used in the optimization steps. The fifth chapter presents the computer implementation of the methods described in the previous chapters. The sixth chapter discusses the symmetry properties of proposed microstructures and how they can be ex-

ploited to reduce the computational cost of the optimization process. The seventh chapter presents several numerical case studies that illustrate the motivation of this thesis. The eighth chapter presents the experimental validations through 3D-printed samples of the nonlinear and linear topologies obtained from the developed computer program. Finally, in the last section, concluding remarks are drawn, and potential research problems that can be pursued in the future are briefly mentioned.

CHAPTER 2

MICROSTRUCTURAL TOPOLOGY OPTIMIZATION

In this chapter, the methodologies that have been used for the topology optimization of nonlinear elastic microstructures have been explained. To give a general overview of microstructural topology optimization, microstructural topology optimization, a top-down approach has been employed.

2.1. Structural Optimization

Structural optimization is an optimization technique that focuses on finding optimum designs for the structural members or the structural layout with the purpose of creating cost and material-efficient structures. Structural optimization can be categorized into three parts; size optimization, shape optimization, and topology optimization (TO) (Christensen & Klarbring, 2008). Design engineers can use these techniques to find the optimum structural dimensions, shapes, and topologies to achieve the desired behavior. In the following part, the differences between the techniques will be explained briefly.

Size optimization is a technique that deals with only the geometric parameters of a structure and does not change the actual geometry, such as the width and height of a beam or the radius of a circular slot in the structure. Shape optimization, on the other hand, searches for ideal shapes by manipulating the structure's geometry. For the case of optimizing the circular slot in the structure, one can use a parametric curve, such as a closed Bézier curve, and by optimizing the control points of the Bézier curve, the optimum shape can be obtained.

While shape optimization optimizes the structure's geometry, topology optimization (TO) optimizes the structure's layout (Bendsøe & Sigmund, 2004). Even though topology optimization and shape optimization may sound similar, in reality, they are entirely different techniques. In the circular slot example, shape optimization can change the geometry of the slot but can not change the number of slots. Topology optimization can add new slots or remove unnecessary ones, along with modifying the slot's geometry. Also, it can be performed without prior design knowledge, e.g., TO can start with a totally random design and achieve very complex designs. This capability of topology

optimization makes it an excellent method for designing complex structures.

2.2. Topology Optimization

Even though the history of topology optimization can be traced back to the work of (Maxwell, 1870) and (Michell, 1904), topology optimization in the modern sense was first introduced by the pioneering work of Bendsøe and Kikuchi in 1988 (Bendsøe & Kikuchi, 1988). Their work had a massive impact on the structural optimization literature. Since then, numerous improvements and new methods have been introduced to make topology optimization more robust and efficient, such as density-based, evolutionary, and level-set methods.

Although topology optimization is able to produce remarkable designs, due to the exceptional features of the designs, manufacturing them using traditional manufacturing techniques such as rolling, milling, turning, and molding is very complicated and even impossible in some cases.

Following the development of additive manufacturing, which is now being studied for almost four decades (Attaran, 2017) and has various uses in fields such as aerospace, automotive, architecture, medicine, and civil engineering, and the increase in computational power of computers, topology optimization gained immense importance decades after its first introduction. These developments enabled us to explore things that had never been done before, such as optimizing high-resolution topologies and investigating the effect of nonlinear behaviors on topologies.

The main goal of topology optimization is to find the optimum material distribution (topology) for a given design domain. The idea is to discretize the design domain into a large number of elements and remove the elements that do not contribute to the overall design from the domain using an appropriate optimization method. Over the years, numerous optimization methods have been developed for this purpose.

Depending on how they approach the optimization process, the methods can be divided into two categories; Gradient-based methods and gradient-free methods. A Gradient-based method optimizes the structure by calculating the necessary gradients, e.g., the gradient of the objective function and the constraints, using the design variables. Solid Isotropic Material Penalization (SIMP) (Bendsøe & Kikuchi, 1988) and Level-Set Method (M. Y. Wang et al., 2003) can be given as examples of methods utilizing gradient-based methods.

Evolutionary algorithms, however, do not use gradients for the optimization procedure but utilize the "survival of the fittest" strategy. Optimization is performed by, in each iteration, eliminating (or adding) based on the fitness of the elements to the desired behavior. Evolutionary Structural Optimization (ESO) (Xie & Steven, 1997) and Bi-directional Evolutionary Structural Optimization (BESO) (Querin et al., 1998) can be given as examples of methods utilizing gradient-free methods.

A commonly used approach to gradient-based methods in topology is density-based methods. Density-based methods assign a relative density value for each element in the design domain and use them as a design variable. For the density-based topology optimization process, the design domain is discretized into a large number of elements with binary relative density values representing whether the region it occupies is "filled" or "void." In literature, it is common to use "1" to represent "full" elements and "0" to represent "void" elements. This binary nature of the elements renders the problem into an integer programming problem (IP), and generally, these problems are significantly more challenging and unfavorable (Liang & Cheng, 2019). Because of this, an integer programming problem is often transformed into a nonlinear programming problem (NLP) by transforming design variables into continuous variables rather than discrete ones. This way, the optimization procedure is simplified.

The disadvantage of taking relative densities as continuous variables is that; since the elements now can take intermediate densities, e.g., density values between zero and one, the obtained topologies will be fuzzy and have unclear boundaries. In order to have black and white, crisp, and clear topologies, the intermediate densities must be eliminated. One way to accomplish this is to use the Solid Isotropic Material with Penalization (SIMP) method.

SIMP is a density-based and one of the most popular methods in the literature and has shown outstanding performance in numerous research (Tcherniak, 2002; Zuo and Saitou, 2017). SIMP method takes the relative density values of the elements and penalizes them using a penalty factor p; this way, the intermediate densities can be decreased significantly as the penalization forces intermediate densities into getting smaller. Hence black and white topologies can be obtained, please see Figure 2.1

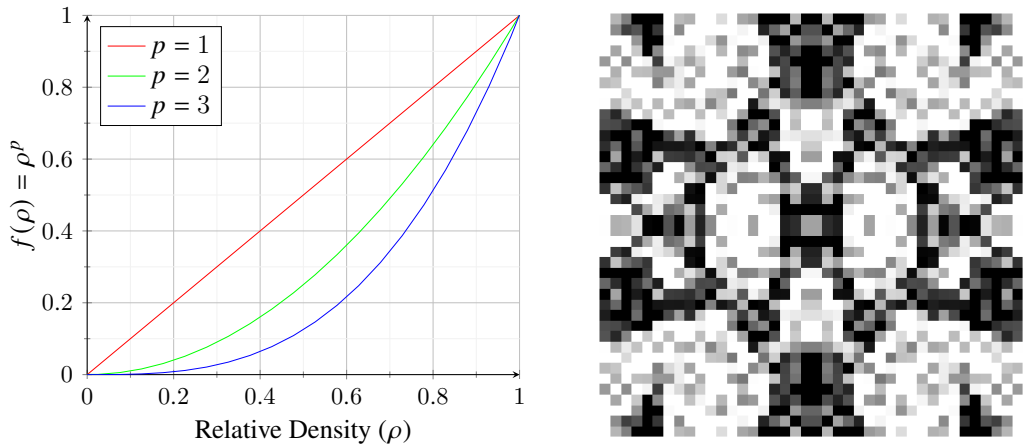

Figure 2.1: Figure showing the graph of the penalty factor p with different values on the left. Discretized unit cell with intermediate densities on the right

2.3. Microstructural Topology Optimization

Microstructural topology optimization is a computational method used to optimize the microstructure of materials. The term microstructure refers to the arrangement of the constituent elements, e.g., grains, inclusions, and pores in a material at a scale that is visible through a microscope. The microstructure of a material can significantly impact the material's mechanical, thermal, electrical, and other properties. In materials science, microstructures are considered one of the most critical factors that determine the properties of a material and its behavior under different conditions. Understanding and controlling the microstructure of a material is crucial for optimizing its performance in various applications. Using mathematical algorithms, one can generate complex, hierarchical structures optimized for specific material properties, such as stiffness, thermal conductivity, negative Poisson's ratio, or acoustical absorption. Despite its many advantages, the microstructural topology optimization process can be computationally intensive, making it difficult to use for large-scale problems (Martinez-Frutos et al., 2017). In the following part, the tools used in microstructural topology optimization are described in detail.

2.4. Concept of Unit Cell

There are various ways to model the behavior of a microstructure, such as the concept of a Representative Volume element (RVE) or a Unit Cell (Drago & Pindera, 2007). RVE is typically used for natural or man-made heterogeneous materials where the

microstructural features have a statistical distribution with significant variation. Whereas unit cell is preferred for the cases where an almost regular repeating pattern is observable at the micro-scale, e.g. 3D printed materials. In this thesis, the unit cell term is used, please see Figure 2.2

A unit cell is a small, representative portion of a material that is used to simulate the behavior of the material as a whole. The unit cell is typically chosen such that it contains a representative sample of the microstructure of the material, including its heterogeneity and material distribution.

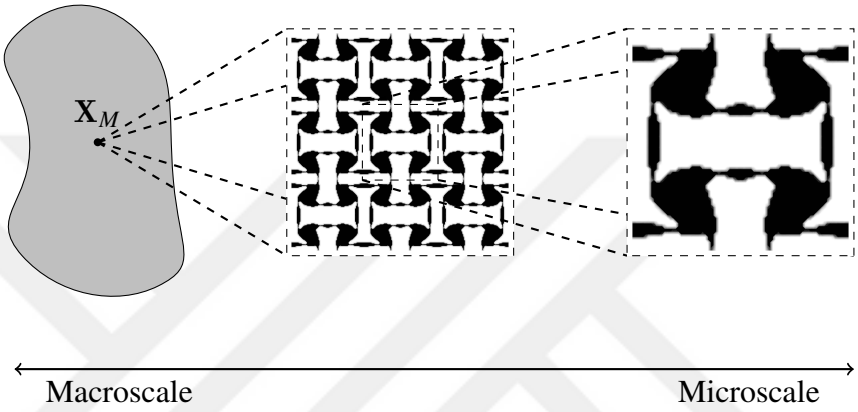

Figure 2.2: An illustrative example of macroscale to microscale linking (Dalklint et al., 2022)

The unit cell is used in analysis to study the mechanical behavior of a material under different loading conditions. The results from these analyses can be used to predict the material's behavior at larger scales and develop models for use in design and engineering applications.

The repeating pattern of periodic unit cells allows for reducing the computational cost of simulating the behavior of the microstructure while still accurately capturing its essential physics. Throughout this thesis, the term unit cell will be used synonymously with periodic unit cell unless specified.

Analysis of a unit cell is typically conducted using the Finite Element Method (FEM). An initial design is created by assigning each finite element a relative density value ρ; this can be done randomly, or an appropriate design can be given. Then, in order to eliminate the numerical instabilities, called checkerboard patterns, which may arise during the optimization process, a filtering scheme needs to be applied, e.g., Helmholtz filter. This filtering scheme also significantly reduces the mesh-dependency problem

(Lazarov & Sigmund, 2010).

Like all the other optimization problems, an objective function and constraints need to be selected for the topology optimization of microstructures. Typically, an objective function and constraints would depend on the components of the stiffness or the stress tensor of the microstructure. The problem is due to the fact that the microstructure is defined as highly heterogeneous; the stiffness and the stress tensors cannot be described straightforwardly. Hence, a homogenization technique needs to be applied. The homogenization procedure is discussed in detail in Chapter 3.

Afterward, since it is necessary to calculate the gradient of the objective and constraint functions, a sensitivity analysis needs to be employed. Sensitivity analysis allows us to determine which finite element's relative density value causes the most significant effect on the behavior of the unit cell. With the information obtained from sensitivity analysis, the finite elements are updated, and regarding their importance on the overall design, they are either "filled" or "emptied" by the algorithm. Until converging a desired objective function value, this iterative optimization process continues.

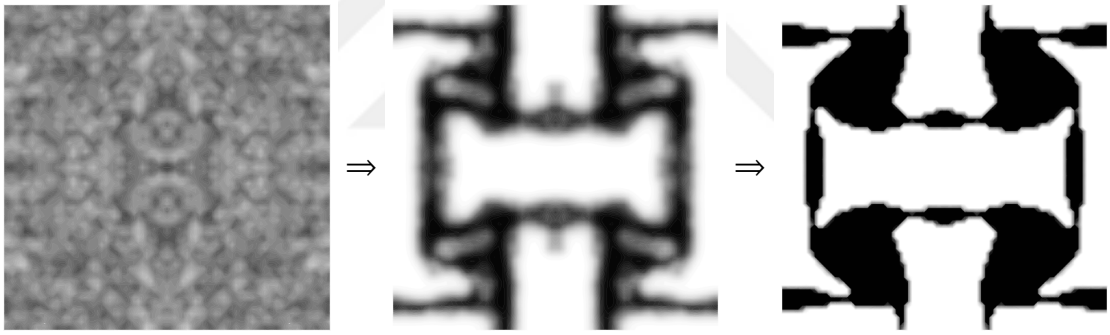

Figure 2.3: Left, Random initial topology; Middle, intermeditate topology; Right, Optimized topology

A flowchart summarizing the previously mentioned analysis steps has been given in Figure 2.4

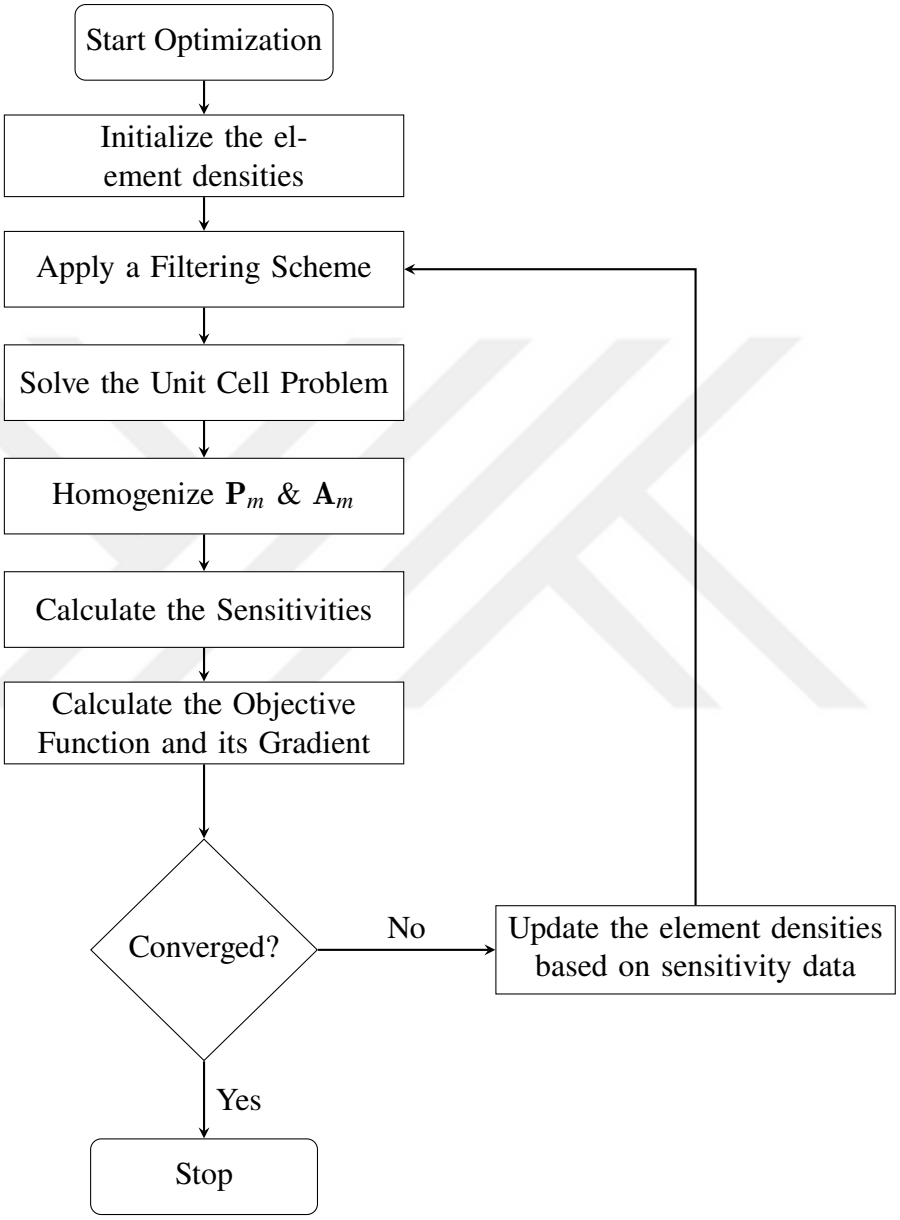

Figure 2.4: A flowchart describing the optimization procedure

CHAPTER 3

NONLINEAR HOMOGENIZATION

Nonlinear homogenization aims to develop a computational method for predicting the behavior of heterogeneous materials. As an extension of linear homogenization, it also takes into account the nonlinear behavior of the materials. Considering the fact that many materials exhibit nonlinear behavior, nonlinear homogenization plays a significant role in the analysis of microstructures.

As explained in the previous chapter, in the topology optimization of microstructures, components of the stiffness or stress tensor of the unit cell are required for the analysis. Because of this, it is necessary to employ a homogenization procedure to analyze heterogeneous microstructures.

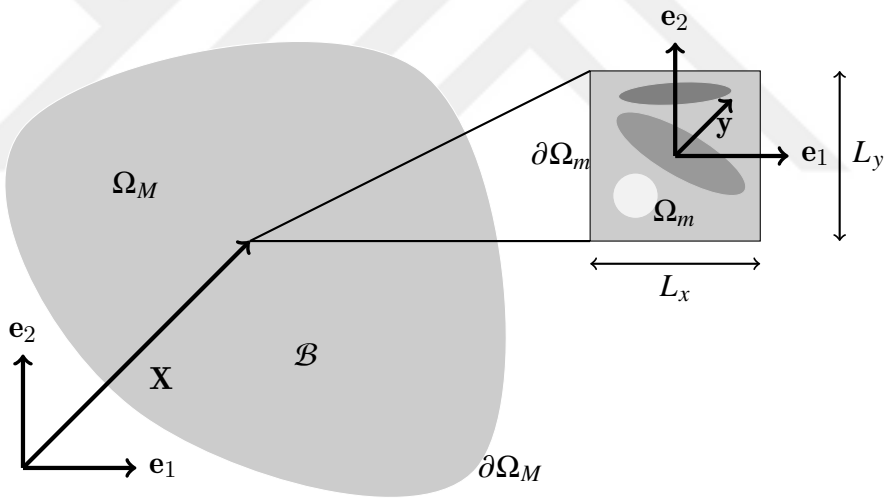

Figure 3.1: Example of a macroscopic structure and the corresponding microstructure at point **X** (Wallin & Tortorelli, 2020)

Over the years, several methods have been developed for the homogenization of microstructures, such as the Method of Multi-Scale Virtual Power (MMVP) (Blanco et al., 2014), Fourier-based Homogenization (Bignonnet et al., 2016) and Nonlinear inverse homogenization (F. Wang et al., 2014)

In this thesis, the Method of Multi-Scale Virtual Power has been used for homogenization purposes. As described in (Blanco et al., 2014; de Souza Neto et al., 2015), the

theory has been built on three concepts;

- Principle of kinematic admissibility
- Mathematical duality
- Principle of multiscale virtual power

These three concepts can be separated into two sections; macroscale to microscale linking and microscale to macroscale linking. The principle of kinematic admissibility will be investigated in the macroscale to microscale linking section. Mathematical duality and the principle of multiscale virtual power concepts will be investigated in the macroscale to microscale linking section.

3.1. Macroscale to Microscale Linking

3.1.1. Kinematic Admissibility

In the analysis of the nonlinear unit cell, a geometric and material nonlinear framework has been used both for the microscale and macroscale. The analyzed microstructure is idealized as a two-dimensional plane strain problem, and consisting of two phases, e.g. solid and void phases.

In order to describe the kinematic relations, an orthonormal coordinate system has been used, and for simplicity, it is assumed that it is the same for both macroscale and microscale. The position vectors for macroscopic and microscopic scales are denoted by $\mathbf{x}$ and $\mathbf{y}$, respectively, and the position vector $\mathbf{x}$ points at the center of the unit cell.

Consider a highly heterogeneous nonlinear elastic macroscopic body, $\mathcal{B}$, let Ω_M be the space occupied by this body, and let $\partial\Omega_M$ be the boundary of this body. Assume all the points inside Ω_M are associated with a microscopic unit cell. When the macroscopic material point is subjected to a macroscopic deformation gradient $\mathbf{F}_M$, this will cause the associated microstructure at that point to experience a deformation gradient $\mathbf{F}_m$.

Following the same convention as (Wallin & Tortorelli, 2020) the total microscopic displacement vector is represented as,

$$\mathbf{u}_m(\mathbf{y}) = \overline{\mathbf{u}}_m(\mathbf{y}) + \widetilde{\mathbf{u}}_m(\mathbf{y}) \tag{3.1}$$

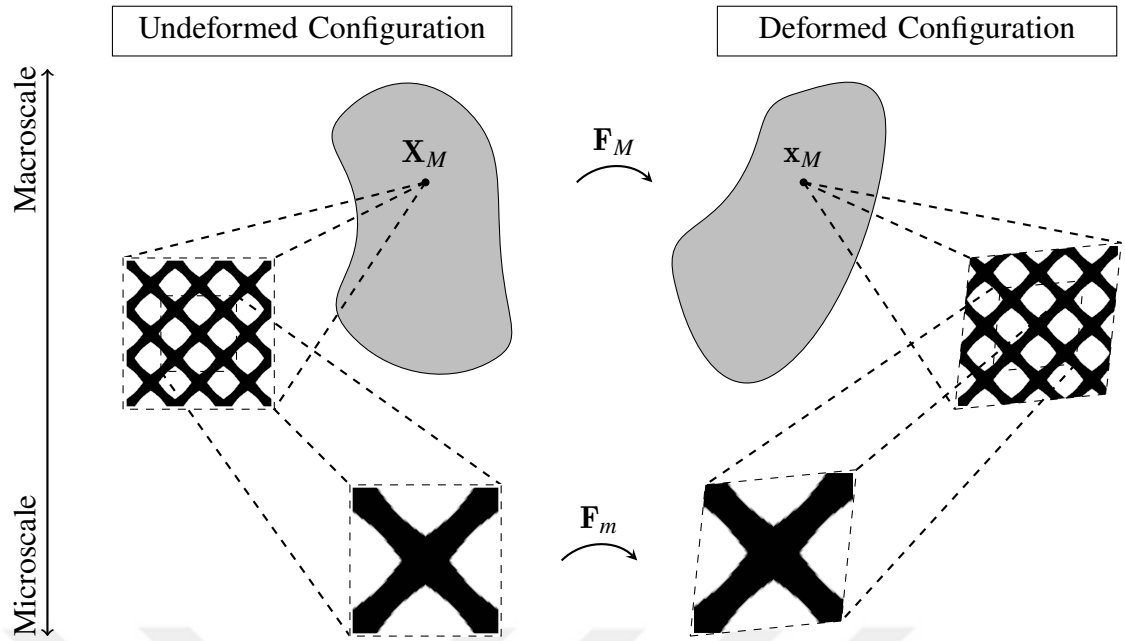

Figure 3.2: A figure showing the effect of macroscopic deformation on the periodic microstructure (Dalklint et al., 2022)

Here, $\overline{\mathbf{u}}_m(\mathbf{y})$, describes the effect of macroscopic displacement on the microstructure, and it is defined as

$$\overline{\mathbf{u}}_m(\mathbf{y}) = \mathbf{u}_M(\mathbf{x}) + \nabla_x \mathbf{u}_M \cdot \mathbf{y} \tag{3.2}$$

Furthermore, the term $\widetilde{\mathbf{u}}_m(\mathbf{y})$ represents the microscopic fluctuations inside the microstructure due to the heterogeneities. Using Eq.(3.1) and Eq.(3.2) one can rewrite $\mathbf{u}_m(\mathbf{y})$ as

$$\begin{aligned} \mathbf{u}_m(\mathbf{y}) &= \overline{\mathbf{u}}_m(\mathbf{y}) + \widetilde{\mathbf{u}}_m(\mathbf{y}) \\ &= \mathbf{u}_M(\mathbf{x}) + \nabla_x \mathbf{u}_M \cdot \mathbf{y} + \widetilde{\mathbf{u}}_m(\mathbf{y}) \end{aligned} \tag{3.3}$$

similarly $\nabla_y \mathbf{u}_m(\mathbf{y})$ can be rewritten as

$$\begin{aligned} \nabla_y \mathbf{u}_m(\mathbf{y}) &= \nabla_y \mathbf{u}_M(\mathbf{x}) + \nabla_y(\nabla_x \mathbf{u}_M \cdot \mathbf{y}) + \nabla_y \widetilde{\mathbf{u}}_m(\mathbf{y}) \\ &= \nabla_x \mathbf{u}_M(\mathbf{x}) + \nabla_y \widetilde{\mathbf{u}}_m(\mathbf{y}) \end{aligned} \tag{3.4}$$

Using these relations, an expression for microscopic deformation gradient in terms of macroscopic deformation gradient can be obtained

$$\begin{aligned}\mathbf{F}_m &= \nabla_y \mathbf{u}_m(\mathbf{y}) + \mathbf{I} \\ &= \nabla_x \mathbf{u}_M(\mathbf{x}) + \nabla_y \widetilde{\mathbf{u}}_m(\mathbf{y}) + \mathbf{I} \\ &= \mathbf{F}_M + \nabla_y \widetilde{\mathbf{u}}_m(\mathbf{y}) \end{aligned} \tag{3.5}$$

Hence the kinematic relation between the macroscale and the microscale has been established. It should be noted that $\mathbf{F}_m$ is also a function of $\nabla_y \widetilde{\mathbf{u}}_m(\mathbf{y})$, gradient of microscopic fluctuations along with the macroscopic deformation gradient $\mathbf{F}_M$, please see Figure 3.2.

3.2. Microscale to Macroscale Linking

3.2.1. Mathematical Duality

In order to create a link between the microscopic and macroscopic scales, it is necessary to describe a macroscopic quantity in terms of the corresponding homogenized microscopic quantity. Using the definition of microscopic total displacement, one can write the homogenization of the microscopic total displacement as follows (see Appendix A for the details of derivations):

$$\begin{aligned}\mathcal{H}(\mathbf{u}_m) &= \frac{1}{|\Omega_m|} \int_{\Omega_m} \mathbf{u}_m(\mathbf{y})\, dv \\ &= \mathbf{u}_M(\mathbf{x}) + \nabla_x \mathbf{u}_M \cdot \frac{1}{|\Omega_m|} \int_{\Omega_m} \mathbf{y}\, dv + \frac{1}{|\Omega_m|} \int_{\Omega_m} \widetilde{\mathbf{u}}_m(\mathbf{y})\, dv \end{aligned} \tag{3.6}$$

Similarly, the homogenization of the gradient of the microscopic total displacement takes the following form

$$\begin{aligned}\mathcal{H}(\nabla_y \mathbf{u}_m) &= \frac{1}{|\Omega_m|} \int_{\Omega_m} \nabla_y \mathbf{u}_m(\mathbf{y})\, dv \\ &= \nabla_y \mathbf{u}_M(\mathbf{x}) + \frac{1}{|\Omega_m|} \int_{\Omega_m} \nabla_y \widetilde{\mathbf{u}}_m(\mathbf{y})\, dv \end{aligned} \tag{3.7}$$

Since the origin of the microstructure is located at the geometric center of the unit

cell, the second part of Eq.(3.6) can be simplified by using the following equation

$$\int_{\Omega_m} \mathbf{y}\ dv = \mathbf{0} \tag{3.8}$$

and therefore Eq.(3.6) and Eq.(3.7) simplify to

$$\mathcal{H}(\mathbf{u}_m) = \mathbf{u}_M(\mathbf{x}) + \frac{1}{|\Omega_m|}\int_{\Omega_m} \widetilde{\mathbf{u}}_m(\mathbf{y})\ dv \tag{3.9}$$

$$\mathcal{H}(\nabla_y \mathbf{u}_m) = \nabla_y \mathbf{u}_M(\mathbf{x}) + \frac{1}{|\Omega_m|}\int_{\Omega_m} \nabla_y \widetilde{\mathbf{u}}_m(\mathbf{y})\ dv \tag{3.10}$$

This means that the homogenization of the microscopic total displacement is equal to the summation of the macroscopic displacement at $\mathbf{x}$ and the homogenization of the microscopic fluctuations over the domain. By imposing specific boundary conditions and restrictions on the symmetry properties of the unit-cell, the following integrals can be set to zero

$$\frac{1}{|\Omega_m|}\int_{\Omega_m} \widetilde{\mathbf{u}}_m(\mathbf{y})\ dv \equiv 0 \tag{3.11}$$

$$\frac{1}{|\Omega_m|}\int_{\Omega_m} \nabla_y \widetilde{\mathbf{u}}_m(\mathbf{y})\ dv \equiv 0 \tag{3.12}$$

therefore, Eq.(3.9) and Eq.(3.10) become

$$\mathbf{u}_M(\mathbf{x}) = \frac{1}{|\Omega_m|}\int_{\Omega_m} \mathbf{u}_m(\mathbf{y})\ dv \tag{3.13}$$

$$\nabla_y \mathbf{u}_M(\mathbf{x}) = \frac{1}{|\Omega_m|}\int_{\Omega_m} \nabla_y \mathbf{u}_m(\mathbf{y})\ dv \tag{3.14}$$

Eq.(3.13) and Eq.(3.14) state that one can calculate the macroscopic total displacement and its gradient by taking the volume average of microscopic total displacement. This is called the "Principle of kinematic admissibility" since it provides the necessary framework to link the microscopic and macroscopic scales.

3.2.2. Principle of Multiscale Virtual Power (PMVP)

The principle of multiscale virtual power is based on the Hill-Mandel principle (Hill, 1963; Mandel, 1971), which states that virtual power at some point $\mathbf{X}$ on the

macrostructure and the microstructure must be equal.

$$P_M^{int} \equiv P_m^{int} \tag{3.15}$$

Macroscopic internal virtual power at the point $\mathbf{x}$ is defined as follows

$$P_M^{int} = \mathbf{P}_M(\mathbf{x}) : \nabla_x \hat{\mathbf{u}}_M(\mathbf{x}) \tag{3.16}$$

where $\mathbf{P}_M(\mathbf{x})$ is the homogenized macroscopic 1^{st} Piola-Kirchhoff stress tensor and $\hat{\mathbf{u}}_M(\mathbf{x})$ is the gradient of the macroscopic virtual displacement. The terms with $\hat{(\cdot)}$ represent the virtual quantities.

Moreover, the microscopic internal virtual power is defined as the volume average of the multiplication of the microscopic 1^{st} Piola-Kirchhoff stress tensor and the gradient of the microscopic virtual displacement

$$P_m^{int} = \frac{1}{|\Omega_m|} \int_{\Omega_m} \mathbf{P}_m(\mathbf{y}) : \nabla_y \hat{\mathbf{u}}_m(\mathbf{y}) \, dv \tag{3.17}$$

which can be put into the following form

$$\begin{aligned} P_m^{int} &= \frac{1}{|\Omega_m|} \int_{\Omega_m} \mathbf{P}_m : (\nabla_x \hat{\mathbf{u}}_M(\mathbf{x}) + \nabla_y \hat{\tilde{\mathbf{u}}}_m(\mathbf{y})) \, dv \\ &= \frac{1}{|\Omega_m|} \int_{\Omega_m} \mathbf{P}_m : \nabla_x \hat{\mathbf{u}}_M(\mathbf{x}) + \mathbf{P}_m : \nabla_y \hat{\tilde{\mathbf{u}}}_m(\mathbf{y}) \, dv \\ &= \frac{1}{|\Omega_m|} \int_{\Omega_m} \mathbf{P}_m : \nabla_x \hat{\mathbf{u}}_M(\mathbf{x}) \, dv + \frac{1}{|\Omega_m|} \int_{\Omega_m} \mathbf{P}_m : \nabla_y \hat{\tilde{\mathbf{u}}}_m(\mathbf{y}) \, dv \end{aligned} \tag{3.18}$$

by substituting Eq.(3.4) into Eq.(3.17). To ensure the Hill-Mandel principle, microscopic and macroscopic virtual powers are equated.

$$\mathbf{P}_M(\mathbf{x}) : \nabla_x \hat{\mathbf{u}}_M(\mathbf{x}) \equiv \frac{1}{|\Omega_m|} \int_{\Omega_m} \mathbf{P}_m \, dv : \nabla_x \hat{\mathbf{u}}_M(\mathbf{x}) + \frac{1}{|\Omega_m|} \int_{\Omega_m} \mathbf{P}_m : \nabla_y \hat{\tilde{\mathbf{u}}}_m(\mathbf{y}) \, dv \tag{3.19}$$

which is after rearranging yields

$$\left(\mathbf{P}_M(\mathbf{x}) - \frac{1}{|\Omega_m|} \int_{\Omega_m} \mathbf{P}_m \, dv \right) : \nabla_x \hat{\mathbf{u}}_M(\mathbf{x}) - \frac{1}{|\Omega_m|} \int_{\Omega_m} \mathbf{P}_m : \nabla_y \hat{\tilde{\mathbf{u}}}_m(\mathbf{y}) \, dv = 0 \tag{3.20}$$

From the above equation, two identities can be obtained by setting each variation

term equal to zero consecutively. First one can be obtained by setting, $\nabla_x \hat{\mathbf{u}}_M(\mathbf{x}) = 0$

$$\frac{1}{|\Omega_m|} \int_{\Omega_m} \mathbf{P}_m : \nabla_y \hat{\tilde{\mathbf{u}}}_m(\mathbf{y})\, dv \equiv 0 \tag{3.21}$$

which states that virtual microscopic fluctuations do not do work on the microstructure. The second one, can be obtained by setting, $\nabla_y \hat{\tilde{\mathbf{u}}}_m(\mathbf{y}) = 0$

$$\left(\mathbf{P}_M(\mathbf{x}) - \frac{1}{|\Omega_m|} \int_{\Omega_m} \mathbf{P}_m\, dv\right) : \nabla_x \hat{\mathbf{u}}_M(\mathbf{x}) = 0 \tag{3.22}$$

Since $\nabla_x \hat{\mathbf{u}}_M(\mathbf{x})$ is arbitrary, Eq.(3.22) implies that the macroscopic 1^{st} Piola-Kirchhoff stress tensor is the volume average of the microscopic 1^{st} Piola-Kirchhoff stress tensor.

$$\mathbf{P}_M(\mathbf{x}) = \frac{1}{|\Omega_m|} \int_{\Omega_m} \mathbf{P}_m\, dv \tag{3.23}$$

In the calculation of homogenized tangent stiffness tensor, since the problem is nonlinear, a unique expression for tangent stiffness tensor does not exist; thus, using the work conjugate $\mathbf{P}_M$ and $\mathbf{F}_M$ pair, $\mathbf{A}_M$ is defined as

$$\mathbf{A}_M = \frac{\partial \mathbf{P}_M}{\partial \mathbf{F}_M} \tag{3.24}$$

Similarly, the microscopic scale is nonlinear as well, the microscopic tangent stiffness tensor is also defined as

$$\mathbf{A}_m = \frac{\partial \mathbf{P}_m}{\partial \mathbf{F}_m} \tag{3.25}$$

these tangent stiffness tensors can be used to express the first-order stress differential $d\mathbf{P}_M$ and $d\mathbf{P}_m$ as

$$d\mathbf{P}_M = \mathbf{A}_M(\mathbf{F}_M) \cdot d\mathbf{F}_M \tag{3.26}$$

$$d\mathbf{P}_m = \mathbf{A}_m(\mathbf{F}_m, \mathbf{y}) \cdot d\mathbf{F}_m \tag{3.27}$$

respectively. Using Eq.(3.23), the differential homogenized macroscopic stress expression can be obtained as

$$d\mathbf{P}_M = \frac{1}{|\Omega_m|} \int_{\Omega_m} d\mathbf{P}_m\, dv \tag{3.28}$$

which takes the following form by the aid of Eq.(3.27)

$$d\mathbf{P}_M = \frac{1}{|\Omega_m|}\int_{\Omega_m} \mathbf{A}_m \cdot d\mathbf{F}_m \, dv \tag{3.29}$$

Using Eq.(3.5), the expression for differential microscopic deformation gradient can be obtained

$$d\mathbf{F}_m = d\mathbf{F}_M + \nabla_y d\widetilde{\mathbf{u}}_m(\mathbf{F}_M; d\mathbf{F}_M) \tag{3.30}$$

Notice that the second part of Eq.(3.30) is also a function of $d\mathbf{F}_M$; this is because the differential displacement field $d\widetilde{\mathbf{u}}_m$ is a function of the microscopic deformation gradient $\mathbf{F}_m$, which itself is a function of the macroscopic deformation gradient $\mathbf{F}_M$. By taking the gradient of $d\widetilde{\mathbf{u}}_m$, the gradient $\nabla_y d\widetilde{\mathbf{u}}_m(\mathbf{F}_M; d\mathbf{F}_M)$, is obtained by evaluating at the current deformation macroscopic deformation level in the direction of $d\mathbf{F}_M$.

Substituting Eq.(3.30) into Eq.(3.29) with the aid of Eq.(3.26) the resulting expression for $d\mathbf{P}_M$ emerges

$$d\mathbf{P}_M = \mathbf{A}_M \cdot d\mathbf{F}_M = \frac{1}{|\Omega_m|}\int_{\Omega_m} \mathbf{A}_m \cdot (d\mathbf{F}_M + \nabla_y d\widetilde{\mathbf{u}}_m(\mathbf{F}_M; d\mathbf{F}_M)) \, dv \tag{3.31}$$

which has an implicit differentiation. As it is not straightforward to deal with the implicit differentiation, in the following part, how the implicit differential $d\mathbf{F}_M$ inside $\nabla_y d\widetilde{\mathbf{u}}_m(\mathbf{F}_M; d\mathbf{F}_M)$ can be annihilated will be discussed, and after that, the main discussion is going to be continued.

As a first step, Eq.(3.21) is linearized as follows

$$\frac{1}{|\Omega_m|}\int_{\Omega_m} d\mathbf{P}_m \cdot \nabla_x \hat{\widetilde{\mathbf{u}}}_m(\mathbf{y}) \, dv = 0 \tag{3.32}$$

using the definition of $d\mathbf{P}_m = \mathbf{A}_m \cdot d\mathbf{F}_m$ and substituting it into Eq.(3.30) gives

$$\frac{1}{|\Omega_m|}\int_{\Omega_m} \mathbf{A}_m \cdot (d\mathbf{F}_M + \nabla_y d\widetilde{\mathbf{u}}_m(\mathbf{F}_M; d\mathbf{F}_M)) \cdot \nabla_x \hat{\widetilde{\mathbf{u}}}_m \, dv = 0 \tag{3.33}$$

using indicial notation and Einstein summation convention, $d\mathbf{F}_M$ can be expressed in indicial notation as

$$d\mathbf{F}_M = (dF_M)_{ij} \cdot \mathbf{e}_i \otimes \mathbf{e}_j = (dF_M)_{ij} \, \mathbf{E}_{ij} \tag{3.34}$$

$$(dF_M)_{ij} = \mathbf{e}_i \cdot \mathbf{F}_M \cdot \mathbf{e}_j = d\mathbf{F}_M \cdot \mathbf{E}_{ij} \tag{3.35}$$

where $i, j = 1, 2$.

Substituting Eq.(3.34) and Eq.(3.35) into Eq.(3.33) gives

$$\frac{1}{|\Omega_m|}\int_{\Omega_m} \mathbf{A}_m \cdot \Big((dF_M)_{ij}\ \mathbf{E}_{ij} + \nabla_y d\widetilde{\mathbf{u}}_m(\mathbf{F}_M; (dF_M)_{ij}\ \mathbf{E}_{ij}) \Big) \cdot \nabla_x \hat{\widetilde{\mathbf{u}}}_m\ dv = 0 \tag{3.36}$$

here, since $\nabla_y d\widetilde{\mathbf{u}}_m$ is a linear function of $(dF_M)_{ij}$, the following identity

$$\nabla_y d\widetilde{\mathbf{u}}_m(\mathbf{F}_M; d\mathbf{F}_M) = \nabla_y d\widetilde{\mathbf{u}}_m(\mathbf{F}_M; (dF_M)_{ij}\ \mathbf{E}_{ij}) \tag{3.37}$$

$$= (dF_M)_{ij}\ \nabla_y d\widetilde{\mathbf{u}}_m(\mathbf{F}_M; \mathbf{E}_{ij}) \tag{3.38}$$

holds. Substituting this relation into Eq.(3.36) gives

$$(dF_M)_{ij}\ \frac{1}{|\Omega_m|}\int_{\Omega_m} \mathbf{A}_m \cdot \Big(\mathbf{E}_{ij} + \nabla_y d\widetilde{\mathbf{u}}_m(\mathbf{F}_M; \mathbf{E}_{ij}) \Big) \cdot \nabla_x \hat{\widetilde{\mathbf{u}}}_m\ dv = 0 \tag{3.39}$$

Since the term $(dF_M)_{ij}$ is arbitrary, it is clear that the integral term must vanish for four different values of $(ij = 11, 22, 12, 21)$. Here, $ij = 11$ corresponds to non-zero 11 component of incremental deformation gradient tensor and the others are defined similarly.

Rearranging Eq.(3.44) gives the following equation

$$\int_{\Omega_m} \mathbf{A}_m \cdot \nabla_y d\widetilde{\mathbf{u}}_m(\mathbf{F}_M; \mathbf{E}_{ij}) \cdot \nabla_x \hat{\widetilde{\mathbf{u}}}_m\ dv = -\int_{\Omega_m} \mathbf{A}_m \cdot \mathbf{E}_{ij} \cdot \nabla_x \hat{\widetilde{\mathbf{u}}}_m\ dv \tag{3.40}$$

and the following expressions are introduced to simplify the notation

$$\widetilde{\chi}_m^{(ij)} = d\widetilde{\mathbf{u}}_m(\mathbf{F}_M; \mathbf{E}_{ij}) \tag{3.41}$$

$$\chi_m^{(ij)} = \mathbf{E}_{ij} \cdot \mathbf{y} + d\widetilde{\mathbf{u}}_m(\mathbf{F}_M; \mathbf{E}_{ij}) \tag{3.42}$$

$$\nabla_y \chi_m^{(ij)} = \mathbf{E}_{ij} + \nabla_y d\widetilde{\mathbf{u}}_m(\mathbf{F}_M; \mathbf{E}_{ij}) = \mathbf{E}_{ij} + \nabla_y \widetilde{\chi}_m^{(ij)} \tag{3.43}$$

where, $\widetilde{\chi}_m^{(ij)}$ is the incremental displacement fluctuation field and $\chi_m^{(ij)}$ is the incremental total displacement field. Thus, Eq.(3.40) can be rewritten as

$$\int_{\Omega_m} \mathbf{A}_m \cdot \nabla_y \widetilde{\chi}_m^{(ij)} \cdot \nabla_x \hat{\widetilde{\mathbf{u}}}_m\ dv = -\int_{\Omega_m} \mathbf{A}_m \cdot \mathbf{E}_{ij} \cdot \nabla_x \hat{\widetilde{\mathbf{u}}}_m\ dv \quad \text{for all } \hat{\widetilde{\mathbf{u}}}_m \tag{3.44}$$

It is important to realize that, in the above equation, $\mathbf{A}_m \cdot \nabla_y \widetilde{\chi}_m^{(ij)}$ is a stress-like quantity, therefore this equation actually represents the weak form of a self equilibrating stress state within the unit cell. $\nabla_y \widetilde{\chi}_m^{(ij)}$ represents a strain-like quantity, and $\mathbf{E}_{ij}$ represents

the "unit strain" that is driving this system. In 2D, this equation must be solved for four different "unit strain" conditions ($\mathbf{E}_{11}, \mathbf{E}_{22}, \mathbf{E}_{12}, \mathbf{E}_{21}$). In Figure 3.3, these unit strain conditions are illustrated.

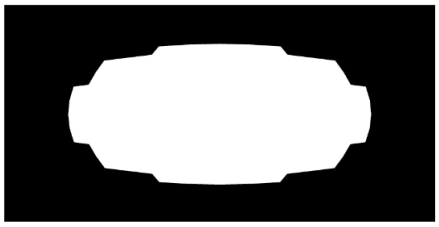

(a) Unit strain condition $\mathbf{E}_{11}$

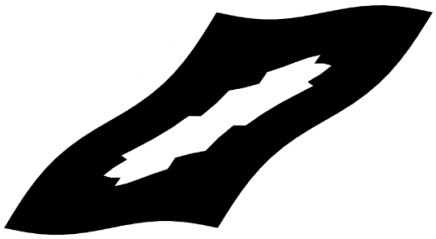

(b) Unit strain condition $\mathbf{E}_{12}$

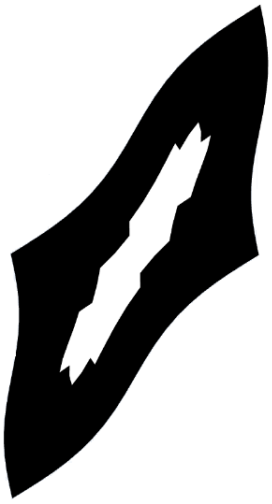

(c) Unit strain condition $\mathbf{E}_{21}$

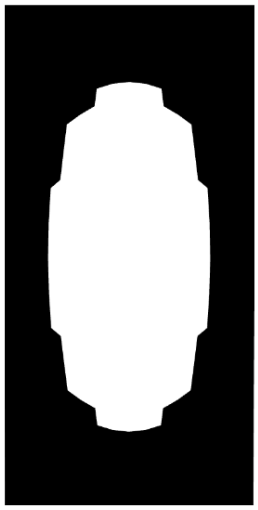

(d) Unit strain condition $\mathbf{E}_{22}$

Figure 3.3: Unit strain conditions

Using the definitions introduced above, it is also possible to write Eq.(3.44) in terms of total incremental displacement field as follows.

$$\int_{\Omega_m} \mathbf{A}_m \cdot \nabla_y \chi_m^{(ij)} \cdot \nabla_x \hat{\tilde{\mathbf{u}}}_m \, dv = 0 \quad \text{for all } \hat{\tilde{\mathbf{u}}}_m \tag{3.45}$$

after solving Eq.(3.45) for every $\chi_m^{(ij)}$ ($\chi_m^{(11)}$, $\chi_m^{(22)}$,$\chi_m^{(12)}$, $\chi_m^{(21)}$), or Eq.(3.44) for $\tilde{\chi}_m^{(ij)}$, the results can be substituted into Eq.(3.31) and the implicit differential $d\mathbf{F}_M$ can be annihilated.

Using the definitions introduced above, Eq,.(3.31) can also be simplified as follows

$$\mathbf{A}_M \cdot d\mathbf{F}_M = \frac{1}{|\Omega_m|} \int_{\Omega_m} \mathbf{A}_m \cdot \left((dF_M)_{ij}\, \mathbf{E}_{ij} + (dF_M)_{ij}\, \nabla_y \widetilde{\chi}_m^{(ij)} \right) dv \tag{3.46}$$

$$= (dF_M)_{ij}\, \frac{1}{|\Omega_m|} \int_{\Omega_m} \mathbf{A}_m \cdot \left(\mathbf{E}_{ij} + \nabla_y \widetilde{\chi}_m^{(ij)} \right) dv \tag{3.47}$$

which, after rearranging (and with the aid of $(dF_M)_{ij} = d\mathbf{F}_M \cdot \mathbf{E}_{ij} = \mathbf{E}_{ij} \cdot d\mathbf{F}_M$), becomes

$$\mathbf{A}_M \cdot d\mathbf{F}_M = \frac{1}{|\Omega_m|} \int_{\Omega_m} \mathbf{A}_m \cdot \left(\mathbf{E}_{ij} \otimes \mathbf{E}_{ij} + \nabla_y \widetilde{\chi}_m^{(ij)} \otimes \mathbf{E}_{ij} \right) dv \cdot d\mathbf{F}_M \tag{3.48}$$

therefore, the expression for homogenized macroscopic tangent stiffness tensor is found to be

$$\mathbf{A}_M = \frac{1}{|\Omega_m|} \int_{\Omega_m} \mathbf{A}_m \cdot \left(\mathbf{E}_{ij} \otimes \mathbf{E}_{ij} + \nabla_y \widetilde{\chi}_m^{(ij)} \otimes \mathbf{E}_{ij} \right) dv \tag{3.49}$$

if necessary, e.g., a specific component of $\mathbf{A}_M$ is used in the objective function, an indicial form of this equation can be obtained as

$$(A_M)_{mnrs} = \frac{1}{|\Omega_m|} \int_{\Omega_m} \mathbf{E}_{mn} \cdot \mathbf{A}_m \cdot \left(\mathbf{E}_{rs} + \nabla_y \widetilde{\chi}_m^{(rs)} \right) dv \tag{3.50}$$

for which the identity $(A_M)_{mnrs} = \mathbf{E}_{mn} \cdot \mathbf{A}_M \cdot \mathbf{E}_{mn}$ is used. It is also possible to write this equation in terms of total incremental displacements as follows

$$(A_M)_{mnrs} = \frac{1}{|\Omega_m|} \int_{\Omega_m} \mathbf{E}_{mn} \cdot \mathbf{A}_m \cdot \nabla_y \chi_m^{(rs)}\, dv \tag{3.51}$$

this equation can be transformed into a more common form in the literature (M. Neves et al., 2000), by adding a slightly modified form of Eq.(3.45), i.e., assigning $\hat{\widetilde{\mathbf{u}}}_m = \chi_m^{(mn)}$, into Eq. (3.51)

$$(A_M)_{mnrs} = \frac{1}{|\Omega_m|} \int_{\Omega_m} \nabla_y \chi_m^{(mn)} \cdot \mathbf{A}_m \cdot \nabla_y \chi_m^{(rs)}\, dv \tag{3.52}$$

To summarize the procedure for homogenization of tangent stiffness tensor, first, solve the displacement field and find $\mathbf{u}_m$, then solve the Eq.(3.45), so-called unit strain problem, for four unit strain $\mathbf{E}_{ij}$ to get $\chi_m^{(ij)}$ $(ij = 11, 22, 12, 21)$. After that, substitute $\chi_m^{(ij)}$ into Eq.(3.52) to find homogenized macroscopic tangent stiffness tensor, $\mathbf{A}_M$

CHAPTER 4

SENSITIVITY ANALYSIS

Sensitivity analysis is a technique for evaluating the response of the analyzed function to small perturbations in the design variables. Small perturbations in each finite element, e.g., a small change in the relative density of the element, will result in a change of response of the unit cell, e.g., a change in stress tensor and tangent stiffness tensor, please see Figure 4.1. Sensitivity analysis aims to measure the effect of these perturbations. (Tortorelli & Michaleris, 1994)

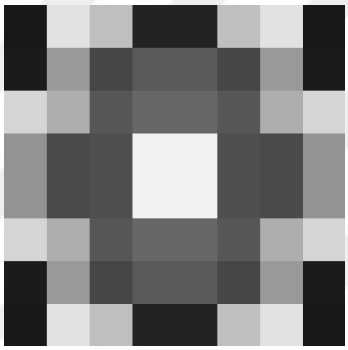

Figure 4.1: Figure illustrating the topology of an 8x8 discretized unit cell. Sensitivity analysis is done by perturbing the relative density of each element and measuring the response of the unit cell.

As noted in earlier chapters, an objective function and constraints are needed for the topology optimization process. The necessary gradients, e.g., the gradient of the tangent stiffness, can be calculated using sensitivity analysis. Typically, in the case of solid mechanics, the objective function is chosen to have components of stiffness and stress tensor. The sensitivity analysis is used to find the responses of these components to changes in the material distribution. To calculate sensitivities, several methods can be used, each with different advantages and disadvantages. These include the finite difference method, the direct differentiation method, and the adjoint method (Gu & Wang, 2013).

The finite difference method, which evaluates the objective function for small perturbations in the design variables, is the most straightforward approach to computing sensitivities. Despite its simplicity, it is computationally expensive as it requires multiple analyses and is prone to numerical errors arising from the perturbation size.

The direct differentiation method involves computing the sensitivities using the chain rule of differentiation. Although computationally efficient and precise, implementing this method can be challenging or even impossible for complex nonlinear systems.

In the adjoint method, sensitivities are computed by defining an auxiliary problem called the adjoint problem and solving the adjoint equation, which is derived from the governing equations of the original problem (Errico, 1997). Because of the properties of the adjoint equation, this method provides an advantage for cases where the number of design variables is much larger than the number of constraint equations and uses fewer computational resources than the other methods (Giles & Pierce, 2000) —making it suitable for topology optimization. The use of the adjoint method in the topology optimization of nonlinear elastic microstructures has been exploited in recent years, and it has been shown to have outstanding performance. In the next sections, the derivations of the sensitivity expressions for homogenized stress tensor and homogenized stiffness tensor will be investigated using the adjoint method.

4.1. Sensitivity of Homogenized Stress Tensor

The sensitivity of each component of the homogenized stress tensor can be obtained by multiplying Eq.(3.23) with $\mathbf{E}_{ij}$, where $\theta_P(\rho)$ is called the response function for $(P_M)_{ij}$

$$\theta_P(\rho) = (P_M)_{ij} = \frac{1}{|\Omega_m|} \int_{\Omega_m} \mathbf{E}_{ij} \cdot \mathbf{P}_m(\mathbf{F}_m, \rho)\, dv \tag{4.1}$$

taking the variation of this equation yields

$$\delta\theta_P(\rho;\delta\rho) = \frac{1}{|\Omega_m|} \int_{\Omega_m} \mathbf{E}_{ij} \cdot \left(\delta\mathbf{P}_m(\mathbf{F}_m, \rho;\delta\rho) + \frac{\partial \mathbf{P}_m(\mathbf{F}_m,\rho)}{\partial \mathbf{F}_m} \cdot \delta\mathbf{F}_m(\rho;\delta\rho)\right) dv \tag{4.2}$$

$$= \frac{1}{|\Omega_m|} \int_{\Omega_m} \mathbf{E}_{ij} \cdot \left(\delta\mathbf{P}_m(\mathbf{F}_m, \rho;\delta\rho) + \mathbf{A}_m(\mathbf{F}_m,\rho) \cdot \nabla_y \delta\widetilde{\mathbf{u}}(\rho;\delta\rho)\right) dv \tag{4.3}$$

in the above expression, every term except the implicit differential $\delta\widetilde{\mathbf{u}}(\rho;\delta\rho)$ can be calculated. In order to find $\delta\widetilde{\mathbf{u}}(\rho;\delta\rho)$ we take the variation of Eq.(3.21)

$$\frac{1}{|\Omega_m|} \int_{\Omega_m} \left(\delta\mathbf{P}_m(\mathbf{F}_m, \rho;\delta\rho) + \mathbf{A}_m(\mathbf{F}_m,\rho) \cdot \nabla_y \delta\widetilde{\mathbf{u}}(\rho;\delta\rho)\right) \cdot \nabla_y \hat{\widetilde{\mathbf{u}}}_m\, dv = 0 \tag{4.4}$$

adding this integral into the Eq.(4.3) gives

$$\delta\theta_P(\rho;\delta\rho) = \frac{1}{|\Omega_m|}\int_{\Omega_m} \mathbf{E}_{ij} \cdot \Big(\delta\mathbf{P}_m(\mathbf{F}_m,\rho;\delta\rho) + \mathbf{A}_m(\mathbf{F}_m,\rho)\cdot\nabla_y\delta\widetilde{\mathbf{u}}(\rho;\delta\rho)\Big)\, dv + \frac{1}{|\Omega_m|}\int_{\Omega_m} \Big(\delta\mathbf{P}_m(\mathbf{F}_m,\rho;\delta\rho) + \mathbf{A}_m(\mathbf{F}_m,\rho)\cdot\nabla_y\delta\widetilde{\mathbf{u}}(\rho;\delta\rho)\Big)\cdot\nabla_y\hat{\tilde{\mathbf{u}}}_m\, dv \quad (4.5)$$

and after rearranging, the following integral expression

$$\delta\theta_P(\rho;\delta\rho) = \frac{1}{|\Omega_m|}\int_{\Omega_m} (\nabla_y\hat{\tilde{\mathbf{u}}}_m + \mathbf{E}_{ij})\cdot\delta\mathbf{P}_m(\mathbf{F}_m,\rho;\delta\rho)\, dv + \frac{1}{|\Omega_m|}\int_{\Omega_m} \mathbf{A}_m(\mathbf{F}_m,\rho)\cdot(\nabla_y\hat{\tilde{\mathbf{u}}}_m + \mathbf{E}_{ij})\cdot\nabla_y\delta\widetilde{\mathbf{u}}(\rho;\delta\rho)\, dv \quad (4.6)$$

is obtained. It is easy to see that the second part of this equation is the same as Eq.(3.45). Thus, it is known that

$$\int_{\Omega_m} \mathbf{A}_m(\mathbf{F_m},\rho)\cdot(\nabla_y\hat{\tilde{\mathbf{u}}}_m + \mathbf{E}_{ij})\cdot\nabla_y\delta\widetilde{\mathbf{u}}_m(\rho;\delta\rho)\, dv = 0 \quad (4.7)$$

using this knowledge, Eq.(4.6) now becomes

$$\delta\theta_P(\rho;\delta\rho) = \frac{1}{|\Omega_m|}\int_{\Omega_m} (\nabla_y\widetilde{\chi}_m^{(ij)} + \mathbf{E}_{ij})\cdot\delta\mathbf{P}_m(\mathbf{F}_m,\rho;\delta\rho)\, dv \quad (4.8)$$

$$= \frac{1}{|\Omega_m|}\int_{\Omega_m} \nabla_y\chi_m^{(ij)}\cdot\delta\mathbf{P}_m(\mathbf{F}_m,\rho;\delta\rho)\, dv \quad (4.9)$$

which is the expression for calculating the sensitivity of the ij^{th} component of the stress tensor $\mathbf{P}$.

4.2. Sensitivity of Homogenized Tangent Stiffness Tensor

The sensitivity of each component of the homogenized stiffness tensor can be obtained by using Eq.(A.4), where $\theta_A(\rho)$ is called the response function for $(\mathbf{A}_M)_{ijrs}$

$$\theta_A(\rho) = (\mathbf{A}_M)_{ijrs}(\rho) = \frac{1}{|\Omega_m|}\int_{\Omega_m} \mathbf{E}_{ij}\cdot\mathbf{A}_m(\mathbf{F}_m,\rho)\cdot\nabla_y\chi_m^{(rs)}(\rho)\, dv \quad (4.10)$$

taking the variation of this equation gives

$$\delta\theta_A(\rho;\delta\rho) = \frac{1}{|\Omega_m|}\int_{\Omega_m} \mathbf{E}_{ij}\cdot\Big(\delta\mathbf{A}_m(\mathbf{F}_m,\rho;\delta\rho)\cdot\nabla_y\chi_m^{(rs)}(\rho) + \frac{\partial\mathbf{A}_m(\mathbf{F}_m,\rho)}{\partial\mathbf{F}_m}\cdot\nabla_y\delta\widetilde{\mathbf{u}}(\rho;\delta\rho)\cdot\nabla_y\chi_m^{(rs)}(\rho) + \mathbf{A}_m(\mathbf{F}_m,\rho)\cdot\nabla_y\delta\chi_m^{(rs)}(\rho)\Big)\,dv \quad (4.11)$$

here, the adjoint method is also used to eliminate the variations of implicit responses. Following the same procedure as in the sensitivity of $\mathbf{P}$, the zero integral Eq.(3.21) has been used. Note that, since $\delta\widetilde{\mathbf{u}}_m(\rho;\delta\rho)$ is arbitrary it has been designated by another function $\mathbf{z}$ to avoid confusion

$$\int_{\Omega_m}\mathbf{A}_m(\mathbf{F}_m,\rho)\cdot\nabla_y\chi_m^{(rs)}(\rho)\cdot\nabla_y\mathbf{z}\,dv = 0 \quad (4.12)$$

Taking the variation of this equation gives

$$\int_{\Omega_m}\Big(\delta\mathbf{A}_m(\mathbf{F}_m,\rho)\cdot\nabla_y\chi_m^{(rs)}(\rho) + \frac{\partial\mathbf{A}_m(\mathbf{F}_m,\rho)}{\partial\mathbf{F}_m}\cdot\nabla_y\delta\widetilde{\mathbf{u}}(\rho;\delta\rho)\cdot\nabla_y\chi_m^{(rs)}(\rho) + \mathbf{A}_m(\mathbf{F}_m,\rho)\cdot\nabla_y\delta\chi^{(rs)}(\rho)\cdot\nabla_y\mathbf{z}\Big)\cdot\nabla_y\mathbf{z}\,dv = 0 \quad (4.13)$$

Adding Eq.(4.11) and Eq.(4.13) together and rearranging the relevant terms, makes it possible to split the resulting equation into three parts.

$$\delta\theta_A(\rho;\delta\rho) = \delta_\rho\theta_A(\rho;\delta\rho) + \delta_\chi\theta_A(\rho;\delta\rho) + \delta_u\theta_A(\rho;\delta\rho) \quad (4.14)$$

where each term contains relevant variations. More precisely, the part containing the $\delta\rho$ variations is

$$\delta_\rho\theta_A(\rho;\delta\rho) = \frac{1}{|\Omega_m|}\int_{\Omega_m}\Big(\mathbf{E}_{ij}\cdot\delta\mathbf{A}_m(\mathbf{F}_m,\rho;\delta\rho)\cdot\nabla_y\chi_m^{(rs)}(\rho) + \delta\mathbf{P}_m(\mathbf{F}_m,\rho;\delta\rho)\cdot\nabla_y\hat{\widetilde{\mathbf{u}}}_m + \delta\mathbf{A}_m(\mathbf{F}_m,\rho;\delta\rho)\cdot\nabla_y\chi_m^{(rs)}(\rho)\cdot\nabla_y\mathbf{z}\Big)\,dv \quad (4.15)$$

the part containing the $\delta\widetilde{\mathbf{u}}$ variations is

$$\delta_u\theta_A(\rho;\delta\rho) = \frac{1}{|\Omega_m|}\int_{\Omega_m}\left(\frac{\partial \mathbf{A}_m(\mathbf{F}_m,\rho)}{\partial \mathbf{F}_m}\cdot\nabla_y\delta\widetilde{\mathbf{u}}(\rho;\delta\rho)\cdot\nabla_y\chi_m^{(rs)}(\rho)\cdot(\mathbf{E}_{ij}+\nabla_y\mathbf{z})\right.$$
$$\left.+\,\mathbf{A}_m(\mathbf{F}_m,\rho)\cdot\nabla_y\delta\widetilde{\mathbf{u}}(\rho;\delta\rho)\cdot\nabla_y\hat{\widetilde{\mathbf{u}}}_m\right)dv \tag{4.16}$$

and the part containing the $\delta\chi$ variations is

$$\delta_\chi\theta_A(\rho;\delta\rho) = \frac{1}{|\Omega_m|}\int_{\Omega_m}\mathbf{A}_m(\mathbf{F}_m,\rho)\cdot\nabla_y\delta\chi_m^{(rs)}(\rho;\delta\rho)\cdot(\mathbf{E}_{ij}+\nabla_y\mathbf{z})\,dv \tag{4.17}$$

For the derivation of these terms please see Eq.(A.8). At first glance, calculating $\delta\theta_A(\rho;\delta\rho)$ seems to be a difficult task, as it requires evaluating multiple integrals containing unknown variables, such as $\mathbf{z}$ and $\hat{\widetilde{\mathbf{u}}}_m$. As it turns out, by using an adjoint method, $\delta\theta_A(\rho;\delta\rho)$ can be computed quite efficiently. In the next part this adjoint method will be described.

Using the arbitrariness of $\mathbf{z}$, it is chosen as $\mathbf{z} = \widetilde{\chi}_m^{(ij)}$, this way the expression for $\delta_\chi\theta_A(\rho;\delta\rho)$ becomes identical to the Eq.(3.45), thus Eq.(4.17) is found to be

$$\delta_\chi\theta_A(\rho;\delta\rho) = \frac{1}{|\Omega_m|}\int_{\Omega_m}\nabla_y\chi_m^{(ij)}(\rho)\cdot\mathbf{A}_m(\mathbf{F}_m,\rho)\cdot\nabla_y\delta\chi_m^{(rs)}(\rho;\delta\rho)\,dv = 0 \tag{4.18}$$

Again, substituting $\mathbf{z} = \widetilde{\chi}_m^{(ij)}$ into Eq.(4.15) $\delta_\rho\theta_A(\rho;\delta\rho)$ simplifies to

$$\delta_u\theta_A(\rho;\delta\rho) = \frac{1}{|\Omega_m|}\int_{\Omega_m}\left(\nabla_y\delta\widetilde{\mathbf{u}}(\rho;\delta\rho)\cdot\frac{\partial \mathbf{A}_m(\mathbf{F}_m,\rho)}{\partial \mathbf{F}_m}\cdot\nabla_y\chi_m^{(rs)}(\rho)\cdot\nabla_y\chi_m^{(ij)}(\rho)\right.$$
$$\left.+\,\mathbf{A}_m(\mathbf{F}_m,\rho)\cdot\nabla_y\delta\widetilde{\mathbf{u}}(\rho;\delta\rho)\cdot\nabla_y\hat{\widetilde{\mathbf{u}}}_m\right)dv \tag{4.19}$$

It is easy to see that, using the arbitrariness of $\hat{\widetilde{\mathbf{u}}}_m$, and selecting an appropriate $\hat{\widetilde{\mathbf{u}}}_m$, it is possible to set Eq.(4.19)

$$\delta_u\theta_A(\rho;\delta\rho) = \frac{1}{|\Omega_m|}\int_{\Omega_m}\left(\nabla_y\delta\widetilde{\mathbf{u}}(\rho;\delta\rho)\cdot\frac{\partial \mathbf{A}_m(\mathbf{F}_m,\rho)}{\partial \mathbf{F}_m}\cdot\nabla_y\chi_m^{(rs)}(\rho)\cdot\nabla_y\chi_m^{(ij)}(\rho)\right.$$
$$\left.+\,\mathbf{A}_m(\mathbf{F}_m,\rho)\cdot\nabla_y\delta\widetilde{\mathbf{u}}(\rho;\delta\rho)\cdot\nabla_y\hat{\widetilde{\mathbf{u}}}_m\right)dv = 0 \tag{4.20}$$

equal to zero. Rearranging above gives the following linear equation

$$\int_{\Omega_m} \nabla_y \delta\widetilde{\mathbf{u}}(\rho;\delta\rho)\cdot\mathbf{A}_m(\mathbf{F}_m,\rho)\cdot\nabla_y\hat{\widetilde{\mathbf{u}}}_m\, dv = \\ -\int_{\Omega_m} \underbrace{\nabla_y \delta\widetilde{\mathbf{u}}(\rho;\delta\rho)\cdot\overbrace{\frac{\partial\mathbf{A}_m(\mathbf{F}_m,\rho)}{\partial\mathbf{F}_m}\cdot\nabla_y\chi_m^{(ij)}(\rho)\cdot\nabla_y\chi_m^{(rs)}(\rho)}^{\text{Stress-like}}}_{\text{Force-like}}\, dv \quad (4.21)$$

which has to be solved for $\widetilde{u}_m$. Upon obtaining $\widetilde{u}_m$ and inserting into Eq.(4.20), the variation term, $\delta_u\theta_A(\rho;\delta\rho)$ term can be annihilated. Therefore, combining with Eq.(4.18), Eq.(4.14) simplifies to

$$\begin{aligned}\delta\theta_A(\rho;\delta\rho) &= \delta_\rho\theta_A(\rho;\delta\rho)+\delta_\chi\theta_A(\rho;\delta\rho)+\delta_u\theta_A(\rho;\delta\rho)\\ &= \delta_\rho\theta_A(\rho;\delta\rho)\end{aligned} \quad (4.22)$$

this means that, if the adjoint equation Eq.(4.21) were to be solved, the variation of tangent stiffness response, θ_A, can be represented by only using the variations with respect to the relative densities.

Using the same substitution, i.e., $\mathbf{z} = \widetilde{\chi}_m^{(ij)}$, $\delta_\rho\theta_A(\rho;\delta\rho)$ becomes

$$\delta_\rho\theta_A(\rho;\delta\rho) = \frac{1}{|\Omega_m|}\int_{\Omega_m}\Big((\mathbf{E}_{ij}+\nabla_y\widetilde{\chi}_m^{(ij)})\cdot\delta\mathbf{A}_m(\mathbf{F}_m,\rho)\cdot(\mathbf{E}_{rs}+\nabla_y\widetilde{\chi}_m^{(rs)}) \\ +\delta\mathbf{P}_m(\mathbf{F}_m,\rho;\delta\rho)\cdot\nabla_y\hat{\widetilde{\mathbf{u}}}_m\Big)\, dv \quad (4.23)$$

or in terms of $\nabla_y\chi_m^{(ij)} = \mathbf{E}_{ij}+\nabla_y\widetilde{\chi}_m^{(ij)}$, $\delta_\rho\theta_A(\rho;\delta\rho)$ can be rewritten as

$$\delta_\rho\theta_A(\rho;\delta\rho) = \frac{1}{|\Omega_m|}\int_{\Omega_m}\Big(\nabla_y\chi_m^{(ij)}(\rho)\cdot\delta\mathbf{A}_m(\mathbf{F}_m,\rho)\cdot\nabla_y\chi_m^{(rs)}(\rho) \\ +\delta\mathbf{P}_m(\mathbf{F}_m,\rho;\delta\rho)\cdot\nabla_y\hat{\widetilde{\mathbf{u}}}_m\Big)\, dv \quad (4.24)$$

therefore the sensitivity of homogenized tangent stiffness tensor becomes

$$\delta\theta_A(\rho;\delta\rho) = \frac{1}{|\Omega_m|}\int_{\Omega_m}\Big(\nabla_y\chi_m^{(ij)}(\rho)\cdot\delta\mathbf{A}_m(\mathbf{F}_m,\rho)\cdot\nabla_y\chi_m^{(rs)}(\rho) + \delta\mathbf{P}_m(\mathbf{F}_m,\rho;\delta\rho)\cdot\nabla_y\hat{\tilde{\mathbf{u}}}_m\Big)\,dv \quad (4.25)$$

This expression describes that, the sensitivity of homogenized tangent stiffness tensor is not only depends on the local tangent stiffness tensors but also the variation of the local stress tensors and the corresponding displacements satisfying Eq.(4.21). This coupling term is expected as the analysis consists of both geometric and material nonlinearity.

It should also be noted that if $\mathbf{P}_m$ is a linear function of $\mathbf{F}_m$ then the partial derivative of $\mathbf{A}_m$ with respect to the microscopic deformation gradient will be zero. As can be seen from Eq.(4.21), this will result in $\hat{\tilde{\mathbf{u}}}_m = 0$, thus Eq.(4.25) simplifies into

$$\delta\theta_A(\rho;\delta\rho) = \frac{1}{|\Omega_m|}\int_{\Omega_m}\nabla_y\chi_m^{(ij)}(\rho)\cdot\delta\mathbf{A}_m(\mathbf{F}_m,\rho)\cdot\nabla_y\chi_m^{(rs)}(\rho)\,dv \quad (4.26)$$

which is the same result obtained by (Watts & Tortorelli, 2016)

CHAPTER 5

COMPUTER IMPLEMENTATION

In this chapter, the practical implementation of the mathematical methodologies discussed in the preceding chapters and the necessary tools for obtaining satisfactory results, such as density filtering and density projection, are discussed. The main goal of this chapter is to transform these theoretical concepts into a computational framework for the topology optimization of nonlinear elastic microstructures.

In this thesis, the finite element method (FEM) is used to construct this computational framework. In the previous chapters, the mathematical equations are derived under the assumption that the unit cell is continuous. These obtained equations now need to be discretized using FEM in order to implement them in a computer.

The following part provides a general overview of the optimization process without entering the details. Optimization consists of the following five major steps; Helmholtz filtering, solution of the nonlinear displacement field, solution of four different $\chi_m^{(ij)}$ fields ($\chi_m^{(11)}, \chi_m^{(22)}, \chi_m^{(12)}, \chi_m^{(21)}$), homogenization of stress and stiffness tensors, and the calculation of sensitivities, please see Algorithm (5.1)

Helmholtz filtering (Lazarov & Sigmund, 2010), is a density filtering method used for reducing the mesh-dependency problem and the numerical instabilities, e.g., checkerboard patterns, that arise during the optimization process. For this purpose, a Helmholtz-type partial differential equation (PDE) must be solved, and filtered densities must be calculated. In the finite element method, this problem can easily be transformed into a linear system of equations and thus can be efficiently solved. To find the nonlinear displacement field $\mathbf{u}_m$, an iterative Newton-Raphson method has been employed. As the assumed material model is nonlinear, the macroscopic deformation gradient, $\mathbf{F}_M$, is incrementally applied to the unit cell to ensure convergence. The problem for the χ field, like the Helmholtz filtering, can also be converted into a linear system of equations following the same finite element procedure. As described in the previous chapter, the homogenization of stress and tangent stiffness tensors differs. While the homogenized stress tensor can be calculated directly using Eq.(3.23), calculating the homogenized tangent stiffness tensor requires solving an adjoint problem, e.g., finding virtual quantity $\hat{\tilde{\mathbf{u}}}_m$. Again, similar to the Helmholtz filtering and χ problem, this problem is linear and

causes minimal concern for the performance of the computation.

Algorithm 5.1 An algorithm showing the five major steps of the optimization

1: Apply the Helmholtz filter: Find $\widetilde{\rho}$
2: Solve the displacement field: $\mathbf{u}_m$
3: Solve the $\chi_m^{(ij)}$ fields for four different cases: $\chi_m^{(11)}, \chi_m^{(22)}, \chi_m^{(12)}, \chi_m^{(21)}$
4: Homogenization: Calculate $\mathbf{A}_M$ and $\mathbf{P}_M$
5: Calculate the sensitivities of the elements

After the sensitivities are obtained, the relative densities need to be updated by an optimization algorithm; the specific algorithm chosen for this thesis is the Method of Moving Asymptotes (MMA) (Svanberg, 1987). The reason for choosing MMA is that it is extensively used in topology optimization, and its robustness in the context of topology optimization problems is validated, (Fanni et al., 2013). As the detailed explanation of MMA is beyond the scope of this thesis, a rough explanation of MMA is provided. MMA is a method developed for optimizing nonlinear programming problems in the context of structural optimization. As an iterative process, in each iteration, MMA creates and solves convex sub-problems of the highly non-convex structural optimization problem. Each convex sub-problem approximates the original problem and is characterized by the asymptotes specified by a set of parameters. In each iteration, the asymptotes are controlled by updating these parameters, and the convergence of the optimization is stabilized through these asymptotes. If the asymptotes are "far apart," the method is forced to be less conservative to speed up to process, and as the asymptotes become "close," the method is forced to be more conservative to ensure convergence. This controllability of MMA makes it an excellent method for highly non-convex structural optimization problems (Christensen & Klarbring, 2008).

Before introducing these algorithmic steps, the discretization of the unit cell, the constitutive model used, and the imposition of the periodic boundary conditions are discussed in the next section.

5.1. Constitutive Model and Discretization of the Unit Cell

In order to represent the nonlinear nature of the problem, the material model for the microstructure is chosen as a compressible neo-Hookean isotropic hyper-elastic two-phase material. Hyper-elasticity is often used to model large deformations (strains), and their

stress-strain relationship is derived from a strain energy density function, ψ (Bonet & Wood, 2008). An isotropic hyper-elastic material must have identical material properties in every material direction; thus, this implies that strain energy density function ψ must be a function of invariants of the right Cauchy-Green deformation tensor $\mathbf{C} = \mathbf{F}^T \cdot \mathbf{F}$

$$\psi(\mathbf{C}) = \psi(I_1, I_2, I_3) \tag{5.1}$$

where, $\mathbf{F}$ is the deformation gradient tensor

$$\mathbf{F} = \nabla_X \mathbf{u} + \mathbf{I} \tag{5.2}$$

and $\nabla_X \mathbf{u}$ is the displacement gradient with respect to material coordinates, and $\mathbf{I}$ is the second-order identity tensor.

The invariants of the Right Cauchy-Green deformation tensor can be calculated as

$$I_1 = \mathrm{tr}(\mathbf{C}) \qquad I_2 = \frac{1}{2}\Big[\mathrm{tr}(\mathbf{C})^2 - \mathrm{tr}(\mathbf{C}^2)\Big] \qquad I_3 = \det(\mathbf{C}) = J^2 \tag{5.3}$$

where $J = \det(\mathbf{F})$. Following (Bonet & Wood, 2008), the strain-energy density function, satisfying the previously mentioned properties, can be defined as follows

$$\psi(\mathbf{F}) = \frac{\mu}{2}(I_1 - 2) - \mu \ln J + \frac{\lambda}{2}(\ln J)^2 \tag{5.4}$$

where μ and λ are the Lamé coefficients and they are defined as

$$\mu = \frac{E}{2(1+\nu)} \qquad \lambda = \frac{E\nu}{(1+\nu)(1-2\nu)} \tag{5.5}$$

throughout the analysis of the microstructure, the Eq.(5.4) will be used as the strain-energy density function,

Using the definition of ψ, 1^{st} Piola-Kirchhoff stress tensor can be found by taking the derivative of $\psi(\mathbf{F})$ with respect to the deformation gradient $\mathbf{F}$

$$\mathbf{P}(\mathbf{F}) = \frac{\partial \psi(\mathbf{F})}{\partial \mathbf{F}} = \mu\mathbf{F} - (\mu - \lambda \ln J)\mathbf{F}^{-T} \tag{5.6}$$

The nominal material tangent stiffness tensor can be found by taking the derivative of 1^{st} Piola-Kirchhoff stress tensor with respect to the deformation gradient $\mathbf{F}$. Components

of tangent stiffness tensor can be expressed in indicial notation as follows

$$A_{ijkl} = \frac{\partial P_{ij}}{\partial F_{kl}} = \mu\delta_{jl}\delta_{ik} + \lambda F_{ij}^{-T} F_{kl}^{-T} + (\mu - \lambda \ln J) F_{il}^{-T} F_{kj}^{-T} \tag{5.7}$$

it should be noted that when $\mathbf{F} = \mathbf{I}$, Eq.(5.7) takes the form

$$A_{ijkl} = \mu(\delta_{il}\delta_{jk} + \delta_{jl}\delta_{ik}) + \lambda\delta_{ij}\delta_{kl} \tag{5.8}$$

which is the same as the linear elastic stiffness tensor $\mathbb{C}$ for small strains. In the following part, the discretization of the unit cell is described. As a side note, from now on, the matrices used in the analysis will be represented in Voigt notation.

For the finite element analysis, the unit cell domain is discretized evenly both in the vertical and horizontal directions using four-node bi-linear quadrilateral finite elements. The analyzed unit cell is assumed to be a square made of a two-phase neo-Hookean material under plane strain conditions. Unless specified, the modulus of elasticity and Poisson's ratio of the assumed Neo-Hookean material are set to be $E = 100$ and $\nu = 0.3$, respectively.

As mentioned in the previous sections, periodic boundary conditions (PBCs) play an essential part when analyzing a periodic unit cell. PBCs can be imposed in various ways; a master-slave approach has been used in this thesis. In the master-slave approach, to implement the PBCs, matching points on each side of the unit cell are needed. For this purpose, a numbering scheme suitable for master-slave relations has been used for node numbers.

The nodes have been divided into three categories; master, slave, and internal nodes, and they have been enumerated in consecutive order. A visual representation of the node numbering can be seen in Figure 5.1. A detailed description of the master-slave categories is given below.

- Master Nodes: Bottom left corner, Bottom edge nodes -except the bottom right corner, Left edge nodes -except the top left corner
- Slave Nodes: Bottom right corner, Top right corner, Top left corner, Top edge nodes, Right edge nodes
- Internal Nodes: All the other remaining nodes in the domain

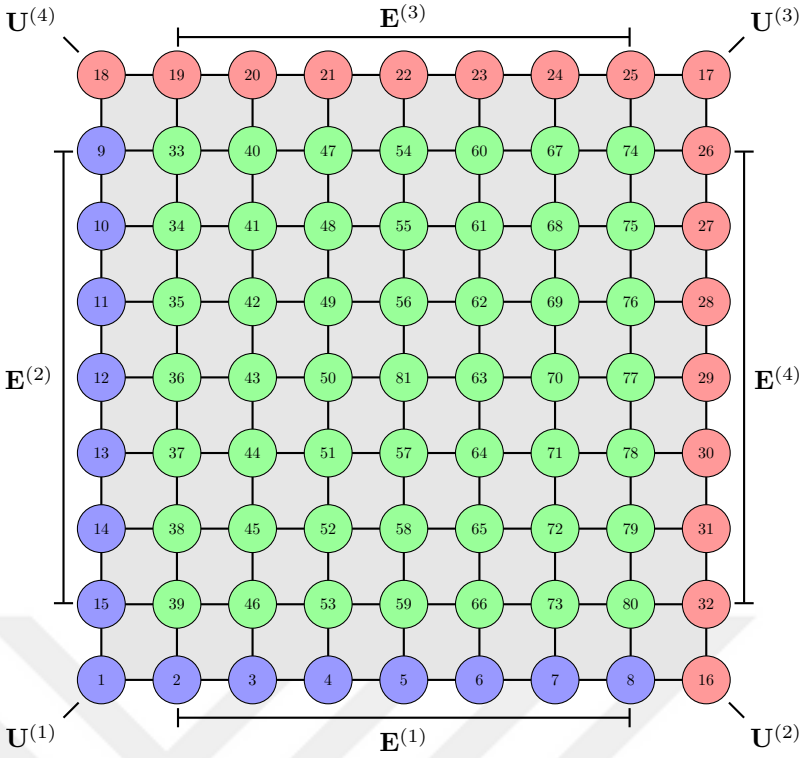

Figure 5.1: Node numbering of an 8x8 discretized domain. The blue, red, and green nodes are master, slave, and internal nodes, respectively.

5.2. Implementation of Periodic Boundary Conditions (PBCs)

To enforce the periodic boundary conditions on the unit cell, master-slave type relations are used. In the following part, these relations are described in detail.

After the numbering scheme is done in the way it is described in the previous section, the following Bloch-type boundary conditions are defined. These equations prescribe the differences in displacements between left-right and top-down edges

$$\mathbf{U}^{(Right)} - \mathbf{U}^{(Left)} = (\mathbf{F}_M - \mathbf{I})(\mathbf{X}^{(Right)} - \mathbf{X}^{(Left)}) = (\mathbf{F}_M - \mathbf{I}) \cdot \mathbf{L}_1 \tag{5.9}$$

$$\mathbf{U}^{(Top)} - \mathbf{U}^{(Bottom)} = (\mathbf{F}_M - \mathbf{I})(\mathbf{X}^{(Top)} - \mathbf{X}^{(Bottom)}) = (\mathbf{F}_M - \mathbf{I}) \cdot \mathbf{L}_2 \tag{5.10}$$

where $\mathbf{L}_1$ and $\mathbf{L}_2$ are defined as $\mathbf{L}_1 = L_x\mathbf{e}_1$ and $\mathbf{L}_2 = L_y\mathbf{e}_2$

As can be seen in Eq.(5.9) and Eq.(5.10), $\mathbf{U}^{(Right)}$ is dependent on $\mathbf{U}^{(Left)}$ and $\mathbf{U}^{(Top)}$ is dependent on $\mathbf{U}^{(Bottom)}$. In other words $\mathbf{U}^{(Right)}$ and $\mathbf{U}^{(Top)}$ are the slaves of $\mathbf{U}^{(Left)}$ and $\mathbf{U}^{(Bottom)}$ respectively. For the imposition of periodicity of the unit cell, this dependency has been established by the master-slave node numbering scheme.These

equations state that when master nodes are solved, using these simple relations, the slave nodes can be calculated. The selected node numbering scheme makes it possible to accomplish this efficiently.

The dependency relations between master and slave nodes can be written explicitly using these simple relations and the master-slave node classification. (Please see appendix for details). To achieve this, Eq.(A.12) and Eq.(A.15) can be combined into a single expression describing the master and slave dependency relations. The resulting dependency relations are presented in a compact manner below.

$$\underbrace{\begin{bmatrix} \mathbf{U}^{(2)} \\ \mathbf{U}^{(3)} \\ \mathbf{U}^{(4)} \\ \hdashline \mathbf{E}^{(3)} \\ \mathbf{E}^{(4)} \end{bmatrix}}_{\mathbf{U}_S} = \underbrace{\left[\begin{array}{c:c} \begin{bmatrix} \mathbf{I} \\ \mathbf{I} \\ \mathbf{I} \end{bmatrix} & [\mathbf{0}] \\ \hdashline [\mathbf{0}] & \begin{bmatrix} \mathbf{I} & \mathbf{0} \\ \mathbf{0} & \mathbf{I} \end{bmatrix} \end{array}\right]}_{\mathbf{D_1}} \underbrace{\begin{bmatrix} \mathbf{U}^{(1)} \\ \hdashline \mathbf{E}^{(1)} \\ \mathbf{E}^{(2)} \end{bmatrix}}_{\mathbf{U}_M} + \overbrace{\underbrace{\left[\begin{array}{c:c} \mathbf{I} & \mathbf{0} \\ \mathbf{I} & \mathbf{I} \\ \mathbf{0} & \mathbf{I} \\ \hdashline \mathbf{0} & \mathbf{I} \\ \mathbf{I} & \mathbf{0} \end{array}\right]}_{\mathbf{D_2}} \underbrace{\begin{bmatrix} (\mathbf{F}_M - \mathbf{I}) \cdot \mathbf{L}_1 \\ (\mathbf{F}_M - \mathbf{I}) \cdot \mathbf{L}_2 \end{bmatrix}}_{\mathbf{U}_{\text{Prescribed}}}}^{\mathbf{H}} \tag{5.11}$$

where subscript "S" stand for "slave" and subscript "M" stand for master nodes. $\mathbf{D}_1$ and $\mathbf{D}_2$ are called dependency matrices.

This equation can be rewritten in a more concise form

$$\mathbf{U}_S = \mathbf{D}_1 \cdot \mathbf{U}_M + \mathbf{D}_2 \cdot \mathbf{U}_{\text{Prescribed}} \tag{5.12}$$

$$\mathbf{U}_S = \mathbf{D}_1 \cdot \mathbf{U}_M + \mathbf{H} \tag{5.13}$$

5.3. Determination of Nonlinear Response of the Unit Cell

Due to both material and geometric nonlinearity, calculation of total microscopic displacement field $\mathbf{u}_m$, and microscopic fluctuation field $\tilde{\mathbf{u}}_m$ requires solving a nonlinear finite element problem. In the solution of this nonlinear problem, the Newton-Raphson algorithm is used, the loading is applied incrementally and the equilibrium position corresponding to each loading step tried to be obtained iteratively. In the solution of this nonlinear problem, periodic boundary conditions must also be taken into account. As mentioned before, since the master-slave approach is applied, the solution of the system is made for the master degree of freedoms, the slave degree of freedoms is derived from the

masters using dependency equations given in Eq.(5.13). While performing these steps, the fully assembled stiffness matrix is then reduced to correspond to the master degree of freedoms. Details regarding this have been given in Appendix A as well.

Algorithm 5.2 Newton-Raphson Algorithm

Initialize $\mathbf{U}$, Δt, TOL, |R|
while $t < 1$ **do**
    $t \leftarrow t + \Delta t$
    $\mathbf{H} \leftarrow \mathbf{H}(\mathbf{F}_M, t)$
    $\mathbf{U} \leftarrow \mathrm{Reduction}(\mathbf{U}, \mathbf{H})$
    Assemble $\mathbf{K}, \mathbf{F}$
    while $|R| >$ TOL **do**
        Solve $\mathbf{K} \cdot \mathbf{dU} = \mathbf{R}$
        $\mathbf{U} \leftarrow \mathbf{U} + \mathbf{dU}$
        Assemble $\mathbf{K}, \mathbf{F}$
    end while
end while
return $\mathbf{U}$

The nonlinear behavior of the problem requires to use of an iterative approach to find the displacements. For this purpose, the Newton-Raphson method has been used. The residual force vector $\mathbf{R}$ for the Newton-Raphson Method is defined as

$$\mathbf{R} = \mathbf{F}^{Ext} - \mathbf{F}^{Int} \tag{5.14}$$

where $\mathbf{F}^{Ext} = 0$ for the problem in hand. Based on the incremental loading procedure, for each step, $\mathbf{H}$ matrix is calculated. Then, using the dependency relations initial displacement field and global stiffness and force matrices are calculated. Upon the solution of the equilibrium equation the corrective displacements are obtained by solving

$$\mathbf{K} \cdot \mathbf{dU} = \mathbf{R} \tag{5.15}$$

and the displacements are updated in an additive manner, please see Algorithm (5.2) for the overall solution procedure. Using the master-slave relation in Eq.(5.13) and the procedures

explained in Appendix A, it is possible to rewrite the matrix equation in Eq.(5.15) as

$$\left[\begin{array}{c|c} \mathbf{K}_{MM}+\mathbf{K}_{MS}\mathbf{D}_1+ & \mathbf{K}_{MI}+\mathbf{D}_1^T\mathbf{K}_{SI} \\ \mathbf{D}_1^T\mathbf{K}_{SM}+\mathbf{D}_1^T\mathbf{K}_{SS}\mathbf{D}_1 & \\ \hline \mathbf{K}_{IM}+\mathbf{K}_{IS}\mathbf{D}_1 & \mathbf{K}_{II} \end{array}\right]\left[\begin{array}{c} d\mathbf{U}_M \\ \hline d\mathbf{U}_I \end{array}\right]=\left[\begin{array}{c} -(\mathbf{R}_M+\mathbf{D}_1^T\mathbf{R}_S) \\ \hline -(\mathbf{R}_I) \end{array}\right] \tag{5.16}$$

where, $d\mathbf{U}$ represents the incremental total displacements

5.4. "Unit Strain" Problems for Incremental Response

The unit strain problems, χ, are solved similarly with the help of FEM. In order to obtain the incremental response, four "unit strain problems" must be solved as a two-dimensional problem. It is important to note that the incremental displacement field differs from the one that appears in the Newton-Raphson incremental, iterative solution setting; here, it means the linear response of the material at the state imposed by the macroscopic deformation gradient.

The equations in Appendix A are adopted in FEM straightforwardly for the computer implementation of unit strain problems. In the computer implementation, the equation with the total incremental response, Eq.(3.45), is used to find the incremental response. In the solution of this linear response, four different $\chi_m^{(ij)}$ must be solved using standard finite element procedure by imposing the periodic boundary conditions. For this, tangent stiffness corresponding to the deformation level reached by the system is required.

Similar to the displacement field solution, the linear problem to calculate χ can be expressed as

$$\left[\begin{array}{c|c} \mathbf{K}_{MM}+\mathbf{K}_{MS}\mathbf{D}_1+ & \mathbf{K}_{MI}+\mathbf{D}_1^T\mathbf{K}_{SI} \\ \mathbf{D}_1^T\mathbf{K}_{SM}+\mathbf{D}_1^T\mathbf{K}_{SS}\mathbf{D}_1 & \\ \hline \mathbf{K}_{IM}+\mathbf{K}_{IS}\mathbf{D}_1 & \mathbf{K}_{II} \end{array}\right]\left[\begin{array}{c} \chi_M \\ \hline \chi_I \end{array}\right]=\left[\begin{array}{c} -(\mathbf{K}_{MS}+\mathbf{D}_1^T\mathbf{K}_{SS})\cdot\mathbf{H} \\ \hline -\mathbf{K}_{IS}\cdot\mathbf{H} \end{array}\right] \tag{5.17}$$

thus the solution to this problem corresponds to the nodal χ responses. Notice that the below equation is similar to Eq.(5.16), with the difference that instead of residuals driving the system, the driving term in this equation is the unit strain terms imposed on the unit cell. For the derivation of this equation, please see Appendix A.

5.5. Density Projection and Helmholtz Filtering

Density Filtering is a process in topology optimization to reduce the number of elements with intermediate densities. In order to have a topology that has a black (full) and white (void) design, density filtering has been developed, and it has proven its effectiveness in numerous studies. Therefore, now it has become a standard process in topology optimization.

Density filtering can be applied by multiplying the stress and stiffness expression by a function, $g(\widetilde{\rho})$, where $\widetilde{\rho}$ represents the filtered densities

$$\mathbf{P}_m(\mathbf{F}_m, \widetilde{\rho}) = g(\widetilde{\rho}) \cdot \mathbf{P}_m(\mathbf{F}_m) \tag{5.18}$$

$$\mathbf{A}_m(\mathbf{F}_m, \widetilde{\rho}) = g(\widetilde{\rho}) \cdot \mathbf{A}_m(\mathbf{F}_m) \tag{5.19}$$

where $g(\widetilde{\rho})$ defined as

$$g(\widetilde{\rho}) = \max(H_{\beta,\omega}(\widetilde{\rho})^p, \epsilon) \tag{5.20}$$

and, $H_{\beta,\omega}(\widetilde{\rho})$ is defined as the smoothed Heaviside step function (Wallin & Tortorelli, 2020)

$$H_{\beta,\omega}(\widetilde{\rho}) = \frac{\tanh(\beta\,\omega) + \tanh(\beta\,(\widetilde{\rho} - \omega))}{\tanh(\beta\,\omega) + \tanh(\beta\,(1 - \omega))} \tag{5.21}$$

where β and ω controlling the steepness and the center of the function respectively. Figure 5.2 illustrates the effect of these parameters.

Even though density filtering helps eliminate intermediate densities and creates black-and-white designs, in most cases, the design achieved by only this method is unsatisfactory and often includes meaningless patterns. This pattern is known as the "checkerboard effect" in the literature. A Helmholtz-type filter (Lazarov & Sigmund, 2010) can be used to eliminate this checkerboard effect. The Helmholtz-type filter is defined by the following equation.

$$\underbrace{\int_{\Omega_m} (\nabla w \cdot r^2 \nabla \widetilde{\rho} + w \cdot \widetilde{\rho})\, dV}_{A(\widetilde{\rho}(\rho), w)} = \underbrace{\int_{\Omega_m} w \cdot \rho\, dV}_{B(\rho, w)} \tag{5.22}$$

where r is the so-called "Helmholtz radius" and increasing r results in less chattering.

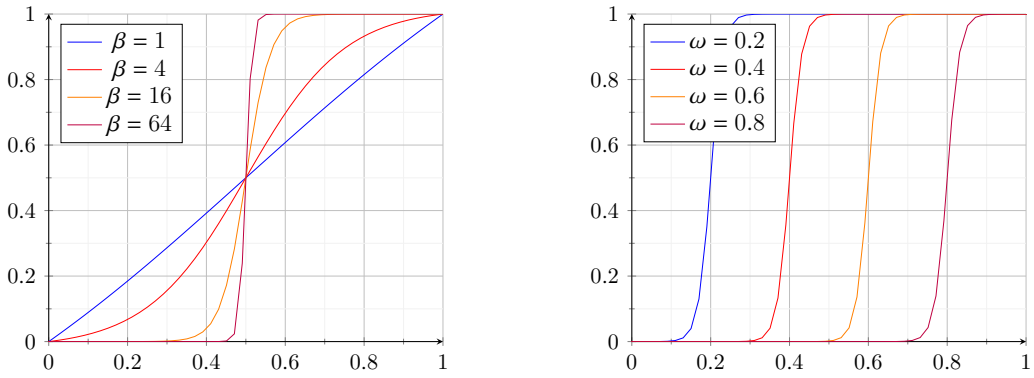

(a) (b)

Figure 5.2: (a) Smoothed Heaviside function centered at $\omega = 0.5$ showing the effect of different β values. (b) Smoothed Heaviside function with a fixed steepness value, $\beta = 32$, showing the effect of different ω values.

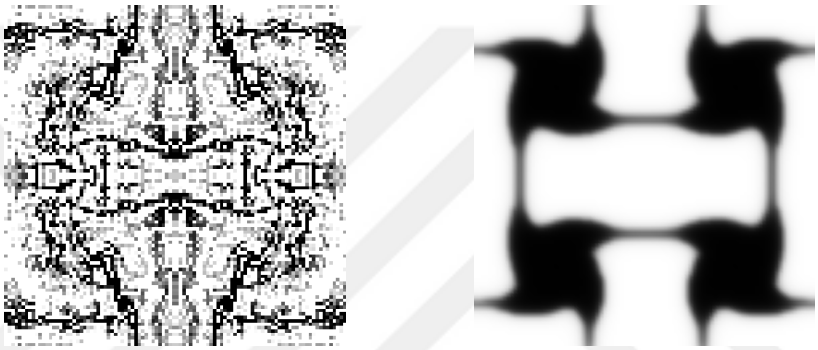

Figure 5.3: Optimum topology of a unit cell optimized without using Helmholtz filter (Left). Optimum topology of the same unit cell, optimized using Helmholtz filter (Right). Both unit cells have been optimized for negative Poisson's ratio under linear analysis, and the domain is discretized into 100x100 mesh.

Figure 5.3 shows that the Helmholtz filter eliminates the checkerboard patterns and gives clean topologies, even though both topologies have density projection, it could not eliminate the intermediate densities as much as the Helmholtz filter. Because of the effectiveness of the filtering techniques, they have been used almost always in the literature. The advantages of the Helmholtz filter come from its ease of implementation in FEM and memory efficiency.

It is important to note that, after application of the Helmholtz filter, the sensitivities of the elements will be changed; thus, special care must be taken to calculate unfiltered element sensitivities. The procedures to find unfiltered sensitivities using filtered sensitivities have been explained in detail in Appendix A.

5.6. Element Distortion Problem

Throughout the optimization iterations, very small element densities can be assigned to elements. In that case, particularly for nonlinear analysis, elements would get distorted such that the determinant of the jacobian associated with the isoparametric mapping becomes negative. In order to suppress this, the material response is slightly altered such that the stress response is composed of two contributions

$$\mathbf{P}_m(\mathbf{F}_m, \widetilde{\rho}) = g(\widetilde{\rho}) \cdot \Bigg(\underbrace{H_{\hat{\beta},\hat{\omega}}(\widetilde{\rho}^p) \cdot \mathbf{P}_m(\mathbf{F}_m)}_{\text{Nonlinear Stress}} + \underbrace{\Big(1 - H_{\hat{\beta},\hat{\omega}}(\widetilde{\rho}^p)\Big) \cdot D^2\hat{\Psi}_m(\mathbf{I}) \cdot (\mathbf{F}_m - \mathbf{I})}_{\text{Linear Stress}} \Bigg) \tag{5.23}$$

and stifffness definition becomes

$$\mathbf{A}_m(\mathbf{F}_m, \widetilde{\rho}) = g(\widetilde{\rho}) \cdot \Bigg(\underbrace{H_{\hat{\beta},\hat{\omega}}(\widetilde{\rho}^p) \cdot \mathbf{A}_m(\mathbf{F}_m)}_{\text{Nonlinear Stiffness}} + \underbrace{\Big(1 - H_{\hat{\beta},\hat{\omega}}(\widetilde{\rho}^p)\Big) \cdot D^2\hat{\Psi}_m(\mathbf{I})}_{\text{Linear Stiffness}} \Bigg) \tag{5.24}$$

where $D^2\hat{\Psi}_m(\mathbf{I})$ is the elasticity tensor

$$D^2\hat{\Psi}_m(\mathbf{I}) = \mu(\delta_{jl}\delta_{ik} + \delta_{il}\delta_{kj}) + \lambda\delta_{ij}\delta_{kl} \tag{5.25}$$

obtained by substituting $\mathbf{I}$ into Eq.(5.7). Here, $H_{\hat{\beta},\hat{\omega}}(\widetilde{\rho}^p)$ is the Eq.(5.21) with $\hat{\beta} = 200$ and $\hat{\omega} = 0.05$. If the density of an element becomes closer to zero, as can be seen from Figure 5.2a and Figure 5.2b, $H_{\hat{\beta},\hat{\omega}}(\widetilde{\rho}^p)$ gets closer to zero as well, thus the effect of nonlinear part in $\mathbf{P}_m(\mathbf{F}_m, \widetilde{\rho})$ vanishes. At the same time, $\big(1 - H_{\hat{\beta},\hat{\omega}}(\widetilde{\rho}^p)\big)$ term gets closer to 1. Thus the effect of the linear part becomes dominant, and the element behaves like a linear elastic element. This behavior is also valid for the stiffness expression since it utilizes the same functions as coefficients.

With these new definitions of stress and stiffness, the sensitivities need to be modified as well. Taking the sensitivity of $\mathbf{P}_m(\mathbf{F}_m, \widetilde{\rho})$ gives

$$\begin{aligned} \delta\mathbf{P}_m(\mathbf{F}_m, \widetilde{\rho}; \delta\widetilde{\rho}) = {} & \frac{g'(\widetilde{\rho})}{g(\widetilde{\rho})} \cdot \mathbf{P}_m(\mathbf{F}_m, \widetilde{\rho}) \cdot \delta\widetilde{\rho} \\ & + p \cdot \widetilde{\rho}^{(p-1)} \cdot g(\widetilde{\rho}) \cdot H'_{\hat{\beta},\hat{\omega}}(\widetilde{\rho}^p) \cdot \Big(\mathbf{P}_m(\mathbf{F}_m) - D^2\hat{\Psi}_m(\mathbf{I}) \cdot (\mathbf{F}_m - \mathbf{I}) \Big) \cdot \delta\widetilde{\rho} \end{aligned} \tag{5.26}$$

and sensitivity of $\mathbf{A}_m(\mathbf{F}_m, \widetilde{\rho})$ becomes.

$$\delta\mathbf{A}_m(\mathbf{F}_m, \widetilde{\rho}; \delta\widetilde{\rho}) = \frac{g'(\widetilde{\rho})}{g(\widetilde{\rho})} \cdot \mathbf{A}_m(\mathbf{F}_m, \widetilde{\rho}) \cdot \delta\widetilde{\rho} + p \cdot \widetilde{\rho}^{(p-1)} \cdot g(\widetilde{\rho}) \cdot H'_{\hat{\beta},\hat{\omega}}(\widetilde{\rho}^p) \cdot \left(\mathbf{A}_m(\mathbf{F}_m) - D^2\hat{\Psi}_m(\mathbf{I}) \right) \cdot \delta\widetilde{\rho} \quad (5.27)$$

thus, expressions for $\mathbf{A}_m$ and $\mathbf{P}_m$ sensitivities are obtained.

5.7. Finite Difference Validation of the Sensitivities

One of the most critical steps of topology optimization is to calculate the sensitivities correctly. If sensitivities are calculated wrong the element densities will be updated incorrectly and thus the optimization algorithm could not find an optimum topology. For this reason, the adjoint sensitivity method derived in the previous section must be validated by using another method such as finite differences. As the finite difference is slow and inefficient, in the context of this thesis, it is used as a validation method for the sensitives obtained from the finite-element-based method. To validate the adjoint sensitivities, a unit cell with the parameters given in the table below is analyzed. As an example, a unit cell discretized by 4 by 4 elements is considered. Due to the orthotropy of the unit cell, the optimization problem has four independent design variables (densities) as shown in Figure 5.4.

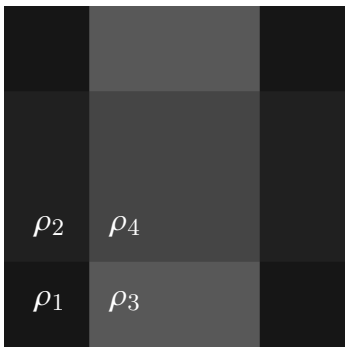

Figure 5.4: Example unit cell with 4 by 4 discretization. Due to orthotropy, there are four design variables, i.e., ρ_1, ρ_2, ρ_3, and ρ_4.

Table 5.1: Table presenting the parameters used for the finite difference verification.

$\mathbf{F}_M$	(L_x, L_y)	$(\text{Nel}_x, \text{Nel}_y)$	(E, ν)	r	p	(β, ω)	$(\hat{\beta}, \hat{\omega})$
$\left[\begin{smallmatrix} 1.05 & 0.05 \\ 0.05 & 1.05 \end{smallmatrix}\right]$	$(3.0, 3.0)$	$(4, 4)$	$(100.0, 0.3)$	2.0	3.0	$(32.0, 0.5)$	$(200.0, 0.05)$

To calculate element sensitivities through the finite difference method, one of the design variables is perturbed by a small value $\epsilon = 10^{-6}$. In other words, a finite element analysis with an unperturbed design variable and another with a perturbed design variable is conducted. The resulting homogenized stiffness values are sued to calculate sensitivities in a discrete sense. Since the perturbation is small, this procedure is considered to be the reference solution. These reference values are compared with the sensitivities calculated through the procedure outlined in Chapter 4, i.e., adjoint sensitivities.

The difference between adjoint sensitivities and finite difference sensitivities of $\mathbf{A}_M$ are presented in the Table below.

Table 5.2: Table presenting the difference of the adjoint sensitivities obtained from FEM and Finite Difference Method (FDM).

	$\delta\mathbf{A}_M^{(\text{FDM})} - \delta\mathbf{A}_M^{(\text{FEM})}$			
$\frac{\partial \mathbf{A}_M}{\partial \rho_1}$	−1.19413e−8	8.03324e−9	8.85485e−11	−1.68781e−9
	−6.17762e−9	1.64802e−8	2.75308e−9	1.86491e−9
	8.85485e−11	2.75308e−9	−6.87168e−9	4.86368e−9
	−2.1319e−9	9.76728e−10	4.86368e−9	−2.10825e−8
$\frac{\partial \mathbf{A}_M}{\partial \rho_2}$	3.31205e−8	−1.00631e−8	1.07408e−9	1.96226e−9
	4.14777e−9	3.31203e−8	−7.02278e−10	1.07409e−9
	1.07408e−9	−1.59046e−9	1.2485e−8	5.60034e−9
	1.51817e−9	1.85908e−10	5.60034e−9	1.2485e−8
$\frac{\partial \mathbf{A}_M}{\partial \rho_3}$	5.59858e−8	1.1285e−8	−2.07719e−9	−1.18901e−9
	4.1796e−9	−4.34904e−8	−2.52129e−9	−1.18901e−9
	−2.07719e−9	−1.63311e−9	−2.00182e−8	−1.8235e−9
	−3.00831e−10	−1.18901e−9	−5.37622e−9	−1.29127e−8
$\frac{\partial \mathbf{A}_M}{\partial \rho_4}$	−4.23966e−8	−4.60837e−9	7.42357e−10	−1.4582e−10
	9.60248e−9	2.86574e−8	2.07462e−9	2.07463e−9
	7.42357e−10	1.18644e−9	2.30647e−8	−1.07738e−9
	−1.4582e−10	2.96281e−9	2.47533e−9	1.74843e−9

Negligible differences between adjoint sensitivities and finite difference sensitivities prove that the adjoint sensitivities are correct and can be safely used to update element densities. A flowchart summarizing the procedures discussed in this chapter is given below.

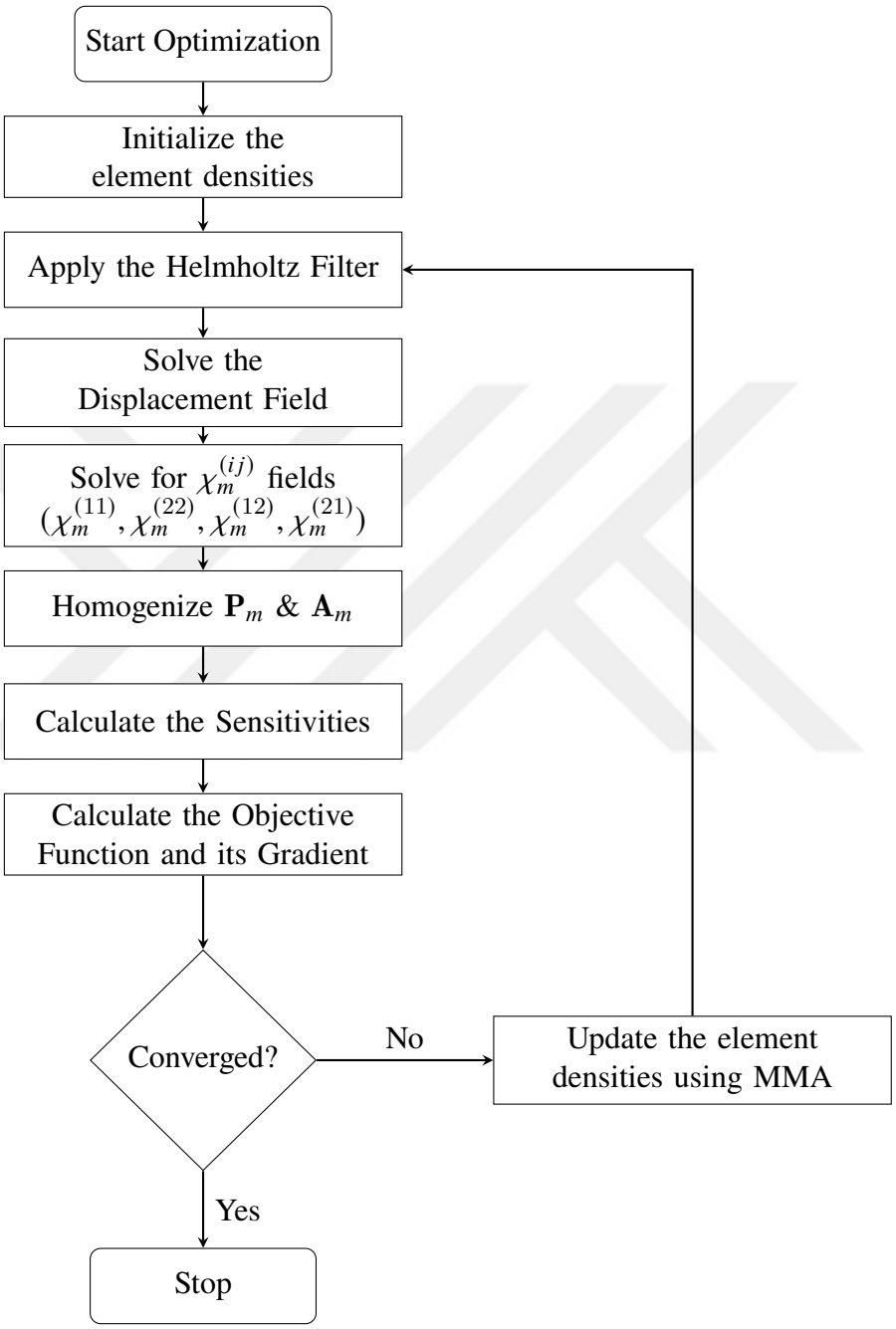

Figure 5.5: A flowchart describing the optimization procedure.

CHAPTER 6

SYMMETRY PROPERTIES AND DOMAIN REDUCTION

As seen in previous chapters, discretizing the unit cell domain into a large number of elements is essential in order to unleash the full potential of topology optimization. Unit cells with more elements have more freedom to capture the most minor and intricate details necessary to obtain optimum topology.

Unfortunately, as the number of elements increases, the computational intensity of the topology optimization also increases. This effect is even more pronounced in the nonlinear analysis, as the nonlinear FEM requires an iterative solution scheme. Fortunately, if a unit cell has symmetry properties, it can be used to reduce the computational cost, as symmetry reduces the size of system matrices. In fact, symmetry conditions have been exploited extensively in conventional FEM analyses in principle to reduce the computational cost. However, regarding the topology optimization literature, only a few studies exploit symmetry properties in the context of the unit cell analysis (Ohno et al., 2001; Saavedra Flores and de Souza Neto, 2010). These exploitations are called domain reduction techniques. The goal of domain reduction techniques is to reduce the design domain size without losing the exactness of the solutions by exploiting the symmetry properties of the unit cell.

The intention of this chapter is to make use of the domain reduction method in the context of topology optimization. In the next section, the implication of microstructural symmetry properties on the microscopic response will be discussed, and how they can be exploited to reduce the domain size will be presented.

6.1. Point Symmetric Unit Cells

Symmetry types used in domain reduction techniques can be divided into three categories: point symmetry, translational symmetry, and combined symmetry (Saavedra Flores & de Souza Neto, 2010). The type of symmetry, in the case of this thesis, is "point symmetry," as the unit cell is enforced to orthotropy by mirroring the bottom left quadrant both vertically and horizontally, which will create a point symmetry with respect to the center of the unit cell. In other words, point symmetry is satisfied if the same microstructure is obtained upon a rotation of 180 degrees around the geometric center of the unit cell, please see Figure 6.1

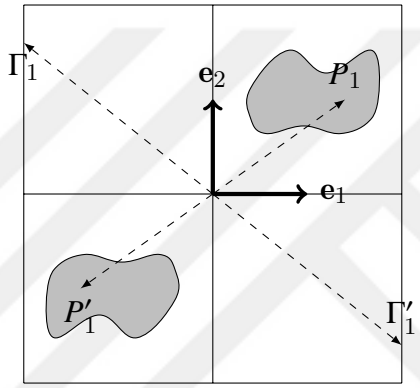

Figure 6.1: Illustration of a point symmetric unit cell. Points (P_1, P'_1) and (Γ_1 and Γ'_1) are corresponding point symmetric pairs within the domain and on the boundary, respectively. $\mathbf{e}_1$ and $\mathbf{e}_2$ are the base vectors (Saavedra Flores & de Souza Neto, 2010).

6.2. Introduction of Semi-Unit Cell

It can be shown that under periodic boundary conditions, for unit cells that satisfy point symmetry, a displacement fluctuation field emerges, which is also point symmetric with respect to the center of the cell (Saavedra Flores & de Souza Neto, 2010). Consequently, the displacement fluctuations on the middle points of the unit cell edges and the center point are found to be zero. In addition, again, as a consequence of periodicity and point symmetry, the displacement fluctuation field along the edges of the unit cell is point symmetric with respect to their corresponding middle point of the edges, please see Figure 6.2.

According to (Ohno et al., 2001), the presence of the symmetry conditions allows the unit cell domain to be reduced to one symmetric half, called a semi-unit cell, by imposing a new boundary condition on the symmetry boundary, please see Figure 6.2.

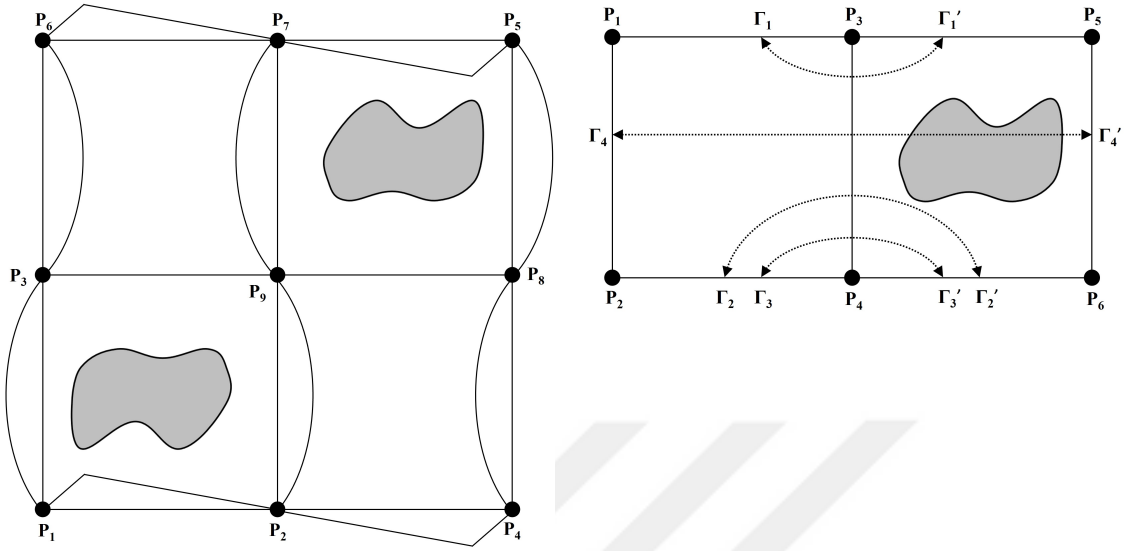

Figure 6.2: (a) Illustration showing the distribution of an example periodic displacement fluctuation field over a unit cell (b) Illustration of a semi-unit cell showing the one to one correspondence of points due to the exploitation of the symmetry of periodic fluctuation field (Saavedra Flores & de Souza Neto, 2010).

In order to enforce this new boundary condition, the periodic boundary conditions must be revised such that the nodes will be connected with respect to a vertical axis passing through the center of the unit cell, please see Figure 6.3. For this reason, in the finite element implementation, the node numbering must be changed accordingly to apply the domain reduction procedure on the unit cell.

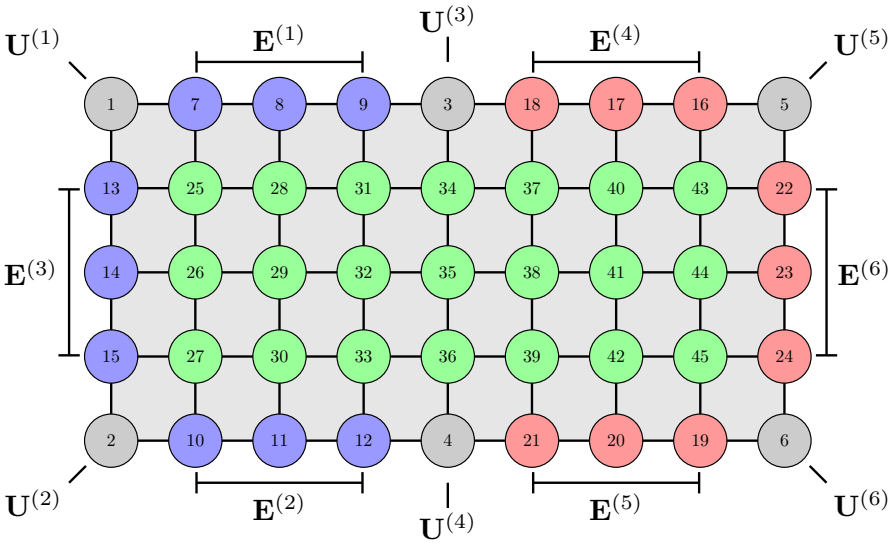

Figure 6.3: Node numbering of an 8 by 8 discretized domain. The gray, blue, red, and green nodes are prescribed, as master, slave, and internal nodes, respectively.

After constructing the dependency matrices similar to Eq.(5.11), the analysis of the unit cell and the optimization can be done similarly after the same procedures are followed in the full domain case. As it turns out, in nonlinear topology optimization, the computational gain from domain reduction will be very significant compared to linear topology optimization. The following part presents figures comparing the effect of domain reduction on the elapsed time per optimization step for different unit cell discretizations. It is clear from the figures that the domain reduction technique reduces computation time significantly, as expected. Please note that the elapsed times in figures are "per iteration." Considering an optimization process will take several hundred iterations, even a tiny change in elapsed time in each iteration can cause substantial changes in the overall process.

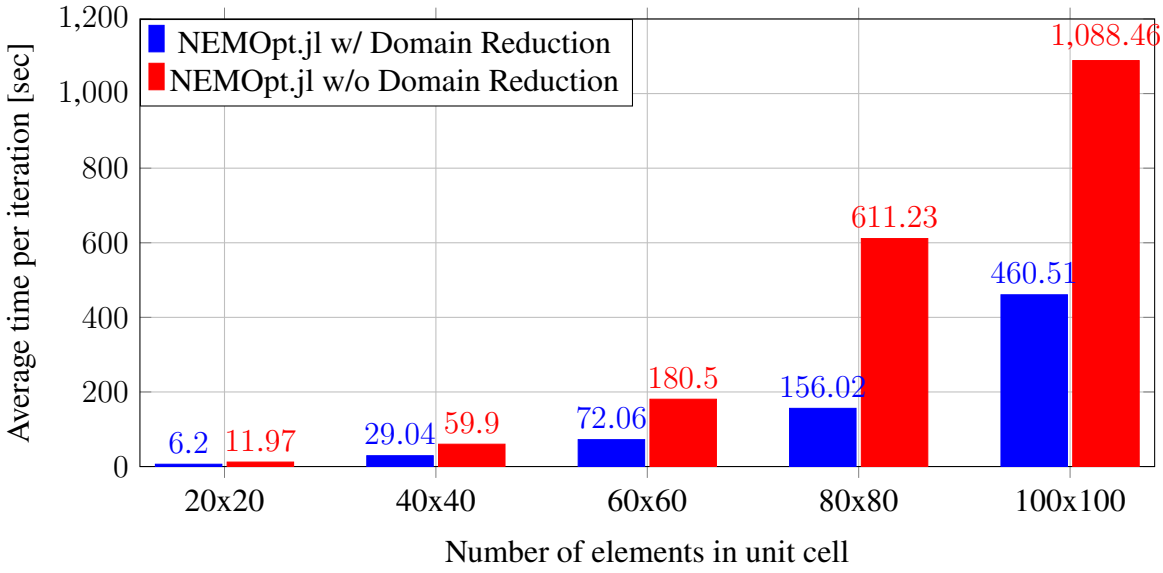

Figure 6.4: Comparison of elapsed times for each optimization step using developed non-linear topology optimization package, NEMOpt.jl. Each analysis was run in TRUBA HPC Clusters.

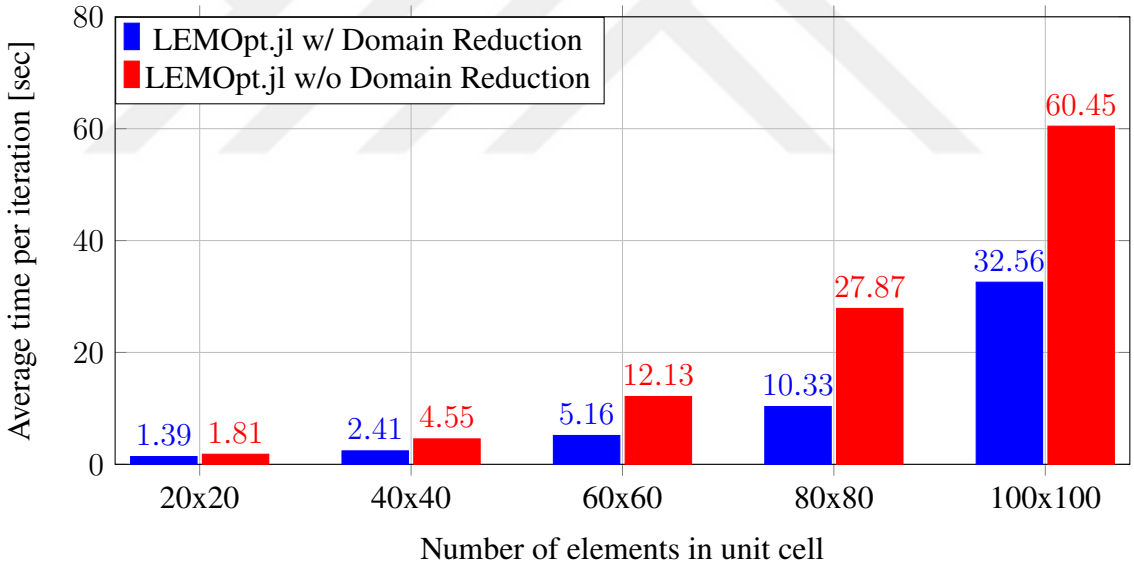

Figure 6.5: Comparison of elapsed times for each optimization step using developed linear topology optimization package, LEMOpt.jl. Each analysis was run in TRUBA HPC Clusters.

CHAPTER 7

NUMERICAL CASE STUDIES

In this chapter, the results obtained from the computer program that is developed are discussed. With the help of different case studies, the significance of nonlinear response in topology optimization is presented.

For simplicity, all presented unit cells are assumed to have the same properties unless specified. The design domain is defined as a 2D rectangular area of size 2.0 units by 2.0 units discretized by 80 x 80 elements. The unit cell is assumed to be made of a nonlinear elastic (Neo-Hookean) material with a Young's modulus of $E = 100$ GPa and a Poisson's ratio of $\nu = 0.3$.

As the optimization algorithm, the Globally Convergent Method of Moving Asymptotes (GCMMA) (Svanberg, 2002) is used. This method is similar to the ordinary Method of Moving Asymptotes (MMA), but as stated by (Svanberg, 2002), it outperforms ordinary MMA both in theory and practice, and it is globally convergent, meaning that for any initial design, it converges to a point for which a necessary condition of optimality holds. It is important to point out that the term "globally convergent" does not mean convergence to a global optimum for all initial designs (Lanckriet & Sriperumbudur, 1970). For the stopping criteria of the optimization, Karush-Kuhn-Tucker (KKT) optimality conditions are used. The default MMA parameters presented by (Svanberg, 1987) are used in MMA. For convenience, Helmholtz radius values are presented in terms of element size, e.g., $r = L/80$. A continuation procedure is implemented to overcome the local minima problem, i.e., the penalty factor p and β increase gradually over the optimization process. For p, it is increased by 0.5 for every 5 iterations until $p = 3$; after that, β is increased by 2 for every 10 iterations until a terminal value of $\beta = 32$. The unit cells are optimized using a maximum volume fraction of 0.5 as a constraint. As an upper limit for the number of iterations, 250 is selected. After 250 iterations, the optimization is terminated.

7.1. Maximizing the Axial Stiffness

In this section, the axial stiffness of the unit cell is optimized for both the horizontal and vertical directions. The details of the optimization problems are presented in the following subsections.

7.1.1. Maximizing A_{1111}

The optimization problem is formulated to maximize the A_{1111} component of the stiffness tensor with a constraint on the volume fraction of the unit cell. The objective function, constraint, and limits are presented below.

$$\begin{aligned} \min_{\rho} \quad & -A_{1111} \\ \text{subject to} \quad & \frac{1}{|\Omega_m|}\int_{\Omega_m} H_{\beta,\omega}(\widetilde{\rho})\, dv - 0.5 \leq 0 \\ & 0 \leq \rho \leq 1 \end{aligned} \tag{7.1}$$

Table 7.1: Table presenting the parameters used in the optimization process for the current case. Please note that $\beta = 1$ and $p = 1$ values represent the initial value of β. The actual value changes according to the continuation scheme throughout the optimization.

$\mathbf{F}_M$	(L_x, L_y)	$(\text{Nel}_x, \text{Nel}_y)$	(E, ν)	r	p	(β, ω)	$(\hat{\beta}, \hat{\omega})$
$\left[\begin{smallmatrix} 1.05 & 0.00 \\ 0.00 & 1.00 \end{smallmatrix}\right]$	$(2, 2)$	$(80, 80)$	$(100.0, 0.3)$	1.5	1.0	$(1.0, 0.5)$	$(200.0, 0.05)$

As given in Table 7.1, imposed deformation gradient corresponds to a 5% stretch in the horizontal direction. Initial random density distribution is shown in Figure 7.1, which after 250 iterations, reached the optimized unit cell shown as well in the same Figure. As the objective was to reach the highest stiffness in the horizontal direction, optimum topology in the form of parallel "bars" in the horizontal direction seems intuitively sensible. The evolution of the objective function throughout y optimization iterations is shown in Figure 7.2. The "steps" observed in the graph correspond to the iterations where the parameters, e.g., p and β, are updated as part of the continuation process. It is worth noting that after a particular iteration number, both the objective function and the volume

fraction stay almost constant, please see Figure 7.3. The bursts observed in the volume fraction evolution curve are typical in density-based topology optimization case studies and also reported by many other studies (Y. Wang and Sigmund, 2023; Li and Khandelwal, 2015).

(a) (b) (c)

Figure 7.1: (a) Initial design, (b) Optimized design, (c) 3x3 array of optimized design

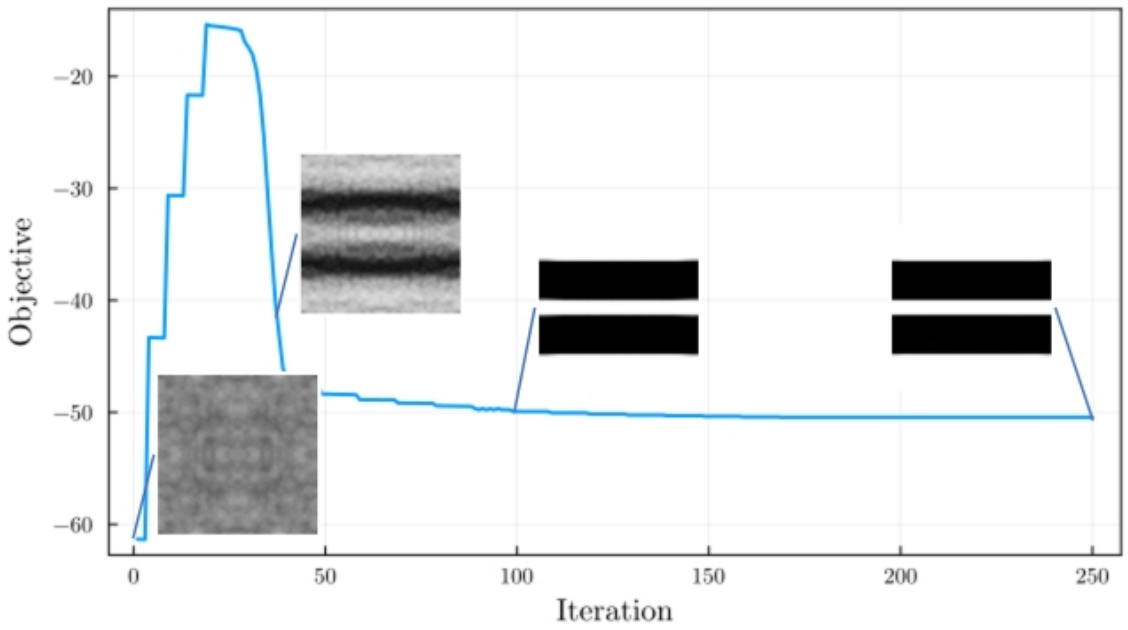

Figure 7.2: Figure illustrating the optimization history, initial topology, intermediate topologies at 35th and 100th iterations and final topology.

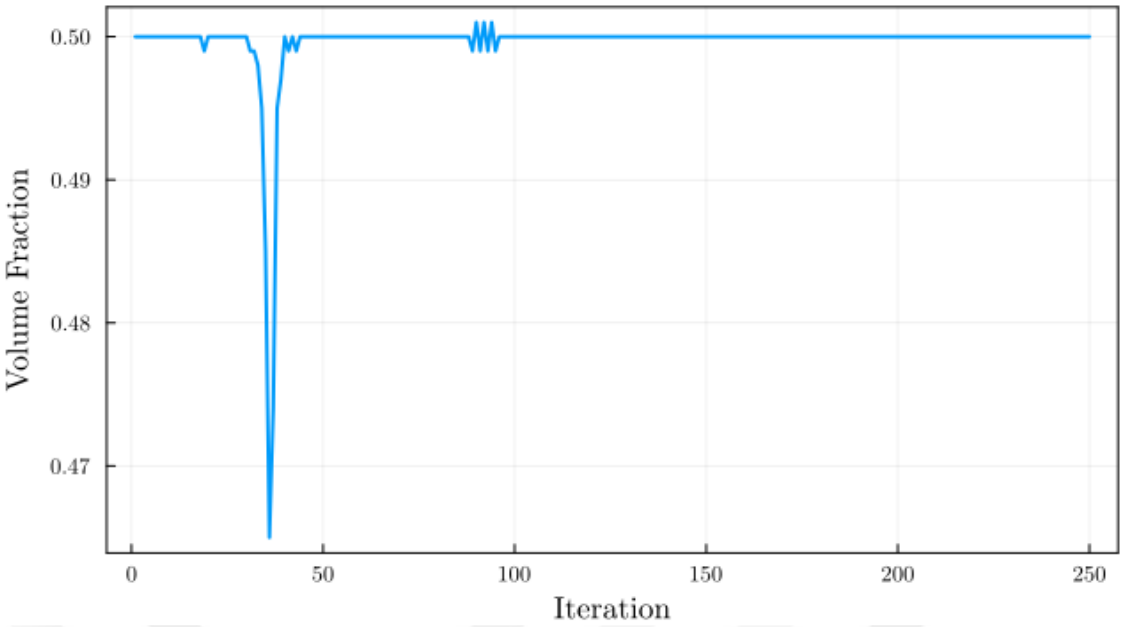

Figure 7.3: Figure illustrating the volume fraction history of the optimization process.

7.1.2. Maximizing A_{2222}

The optimization problem is formulated to maximize the A_{2222} component of the stiffness tensor with a constraint on the volume fraction of the unit cell. The objective function, constraint, and limits are presented below.

$$\begin{aligned} \min_{\rho} \quad & -A_{2222} \\ \text{subject to} \quad & \frac{1}{|\Omega_m|}\int_{\Omega_m} H_{\beta,\omega}(\widetilde{\rho})\, dv - 0.5 \leq 0 \\ & 0 \leq \rho \leq 1 \end{aligned} \tag{7.2}$$

To test whether the optimization will give the same topology with the A_{1111} case, the previous initial design is rotated $90°$ and optimized using the same parameters.

Table 7.2: A table presenting the parameters used in the optimization process for the current case. Please note that $\beta = 1$ and $p = 1$ values represent the initial value of β. The actual value changes according to the continuation scheme throughout the optimization.

$\mathbf{F}_M$	(L_x, L_y)	$(\text{Nel}_x, \text{Nel}_y)$	(E, ν)	r	p	(β, ω)	$(\hat{\beta}, \hat{\omega})$
$\left[\begin{smallmatrix} 1.00 & 0.00 \\ 0.00 & 1.05 \end{smallmatrix}\right]$	$(2, 2)$	$(80, 80)$	$(100.0, 0.3)$	1.5	1.0	$(1.0, 0.5)$	$(200.0, 0.05)$

(a) (b) (c)

Figure 7.4: (a) Initial design, (b) Optimized design, (c) 3x3 array of optimized design

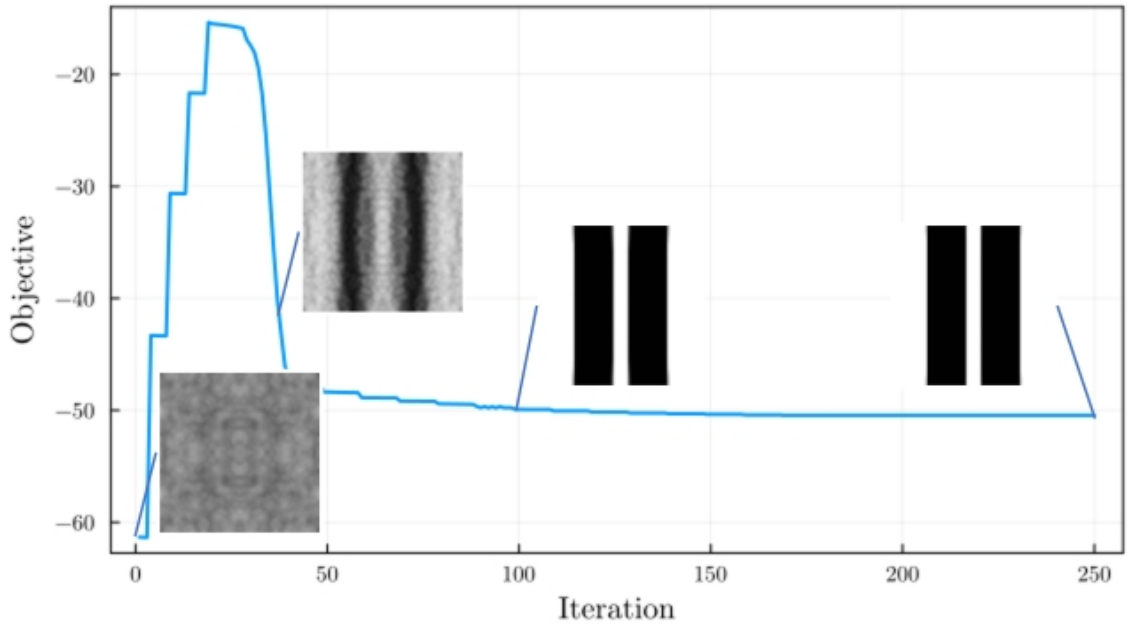

Figure 7.5: Figure illustrating the optimization history, initial topology, intermediate topology at 35th and 100th iterations and final topology.

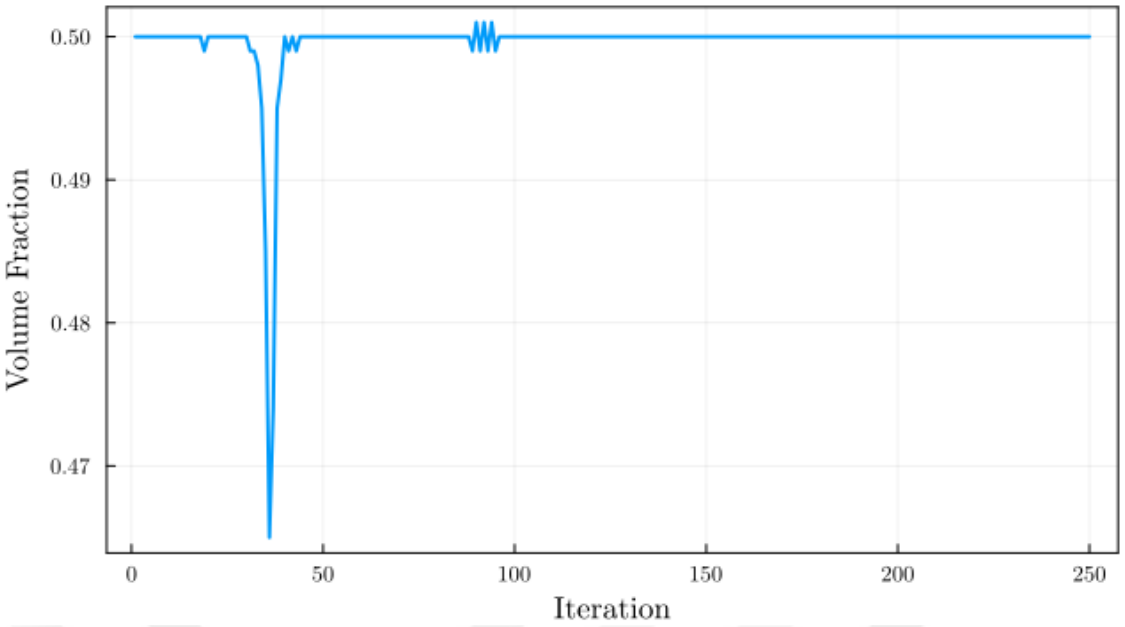

Figure 7.6: Figure illustrating the volume fraction history of the optimization process.

As expected, the initial design that is rotated 90° produced identical results for the A_{2222} case. As seen from Figure 7.8 and Figure 7.9, almost identical evolution curves (as compared to the previous case) are obtained, which could be considered as a strong sign of the robustness of the implementation.

As mentioned before, the optimization problem in hand has a non-convex nature and may lead to a different optimum topology depending on the initial design seed. To illustrate this aspect, the maximization of A_{22222} problem is re-considered by taking a different initial design, shown in Figure 7.9 As stated in Table 7.3, all the other parameters are set to the same values used in the previous case.

Table 7.3: Table presenting the parameters used in the optimization process for the current case. Please note that $\beta = 1$ and $p = 1$ values represent the initial value of β. The actual value changes according to the continuation scheme throughout the optimization.

$\mathbf{F}_M$	(L_x, L_y)	$(\text{Nel}_x, \text{Nel}_y)$	(E, ν)	r	p	(β, ω)	$(\hat{\beta}, \hat{\omega})$
$\begin{bmatrix} 1.00 & 0.00 \\ 0.00 & 1.05 \end{bmatrix}$	$(2, 2)$	$(80, 80)$	$(100.0, 0.3)$	1.5	1.0	$(1.0, 0.5)$	$(200.0, 0.05)$

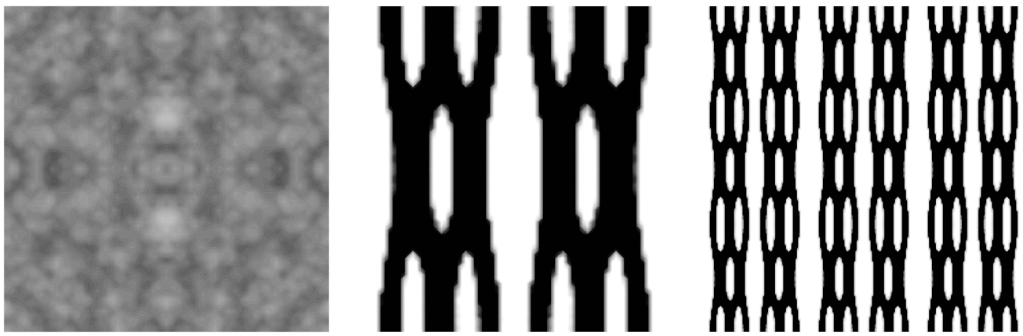

(a) (b) (c)

Figure 7.7: (a) Initial design, (b) Optimized design, (c) 3x3 array of optimized design

It is obvious that the resulting optimum microstructure is not identical to the previous one. Although the tendency to distribute all the material in some sort of 'bars' along the y-direction is visible, a different central pattern emerges from this initial seed. The qualitative behavior of the evolution of objective function and volume fraction constraint curves are identical to the previous case. Again these observations could be considered as strong indicators of the robustness of the implementation.

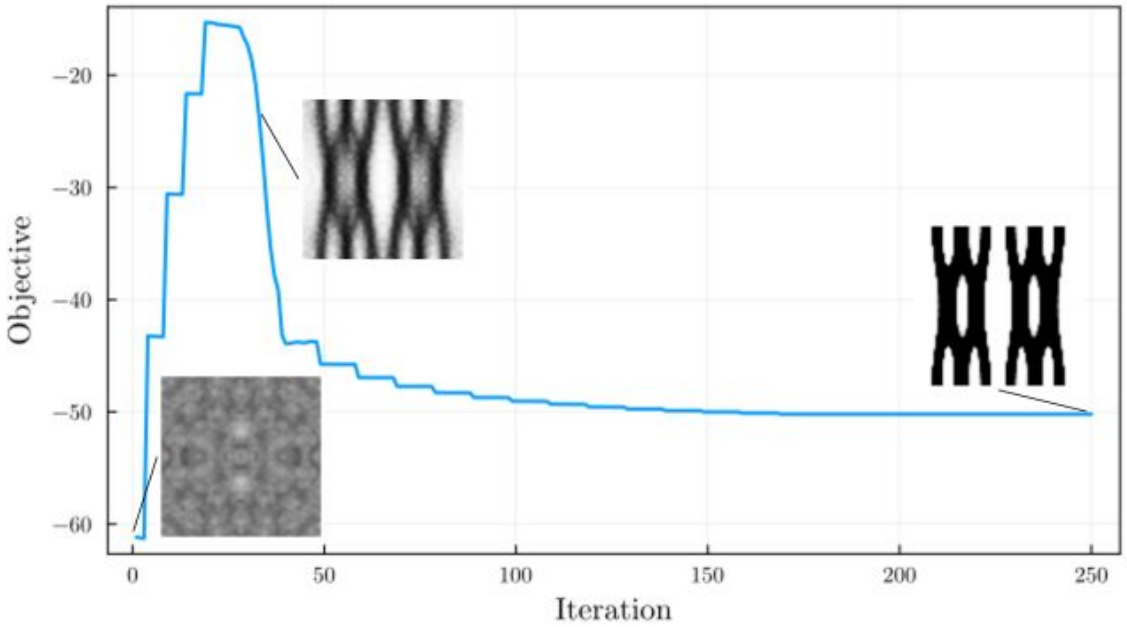

Figure 7.8: Figure illustrating the optimization history, initial topology, intermediate topologies at 35th iteration and final topology.

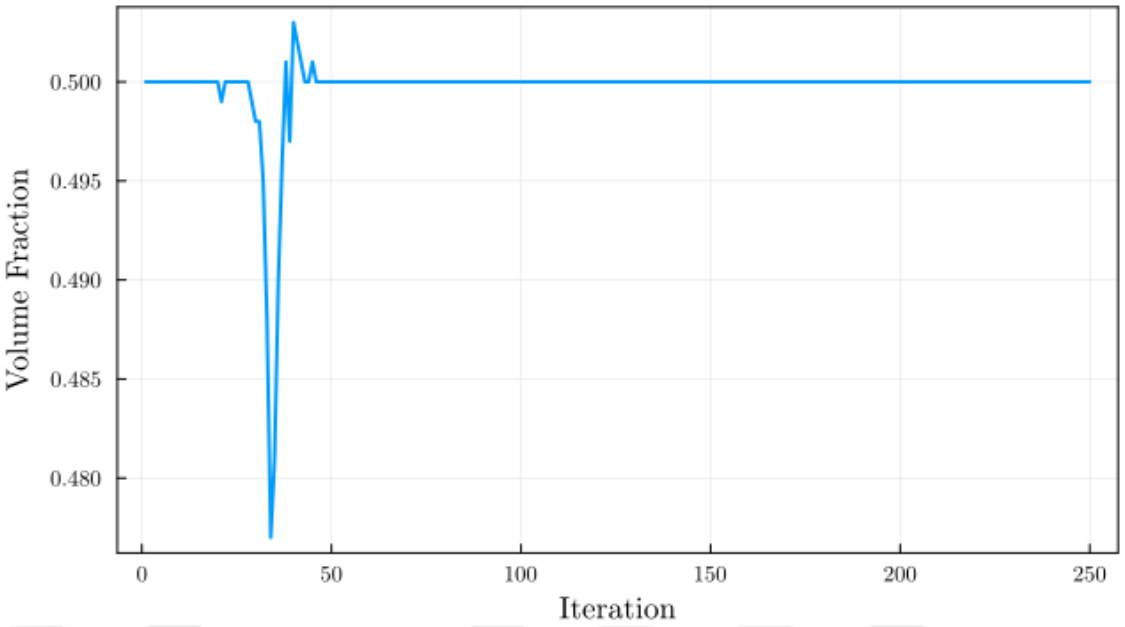

Figure 7.9: Figure illustrating the volume fraction history of the optimization process.

7.2. Maximizing the Shear Stiffness

Shear stiffness and bulk modulus maximization cases are two frequently used case studies in the literature (Kollmann et al., 2020; Xia and Breitkopf, 2015). First, the maximization of shear stiffness is going to be addressed.

The optimization problem is formulated to maximize the shear stiffness of the unit cell with a constraint on the volume fraction. The objective function, constraint, and limits are presented below.

$$\begin{aligned} \min_{\rho} \quad & -\frac{1}{2}(A_{1212} + A_{2121}) \\ \text{subject to} \quad & \frac{1}{|\Omega_m|}\int_{\Omega_m} H_{\beta,\omega}(\widetilde{\rho})\, dv - 0.5 \leq 0 \\ & 0 \leq \rho \leq 1 \end{aligned} \tag{7.3}$$

Table 7.4: Table presenting the parameters used in the optimization process for the current case. Please note that $\beta = 1$ and $p = 1$ values represent the initial value of β. The actual value changes according to the continuation scheme throughout the optimization.

$\mathbf{F}_M$	(L_x, L_y)	$(\text{Nel}_x, \text{Nel}_y)$	(E, ν)	r	p	(β, ω)	$(\hat{\beta}, \hat{\omega})$
$\left[\begin{smallmatrix} 1.00 & 0.05 \\ 0.05 & 1.00 \end{smallmatrix}\right]$	$(2, 2)$	$(80, 80)$	$(100.0, 0.3)$	1.5	1.0	$(1.0, 0.5)$	$(200.0, 0.05)$

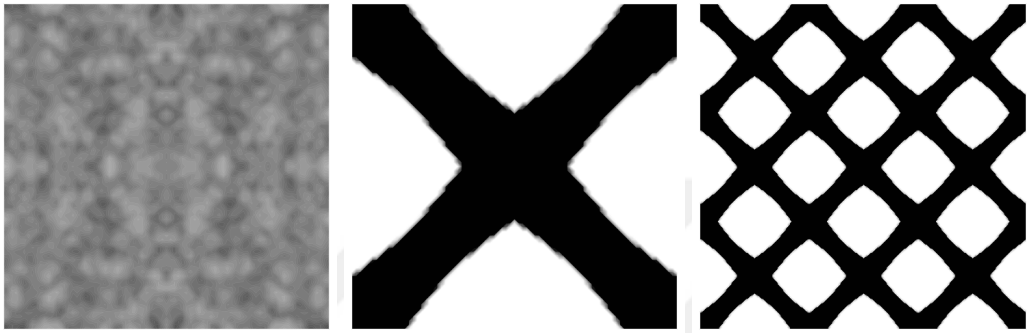

(a) (b) (c)

Figure 7.10: (a) Initial design, (b) Optimized design, (c) 3x3 array of optimized design

The resulting optimum topology, shown in Figure 7.10, is composed of 'crossing diagonal bars,' which gives the highest resistance against shear-type deformations, please see Table 7.4 for the imposed deformation gradient. This result is consistent with the optimum topologies obtained both by gradient-based optimization (M. Neves et al., 2000) and evolutionary algorithms (Radman et al., 2012). Since the problem formulation considered here is both materially and geometrically nonlinear, the geometry of the 'arms' of the optimum topology obtained here is slightly different from the references mentioned above.

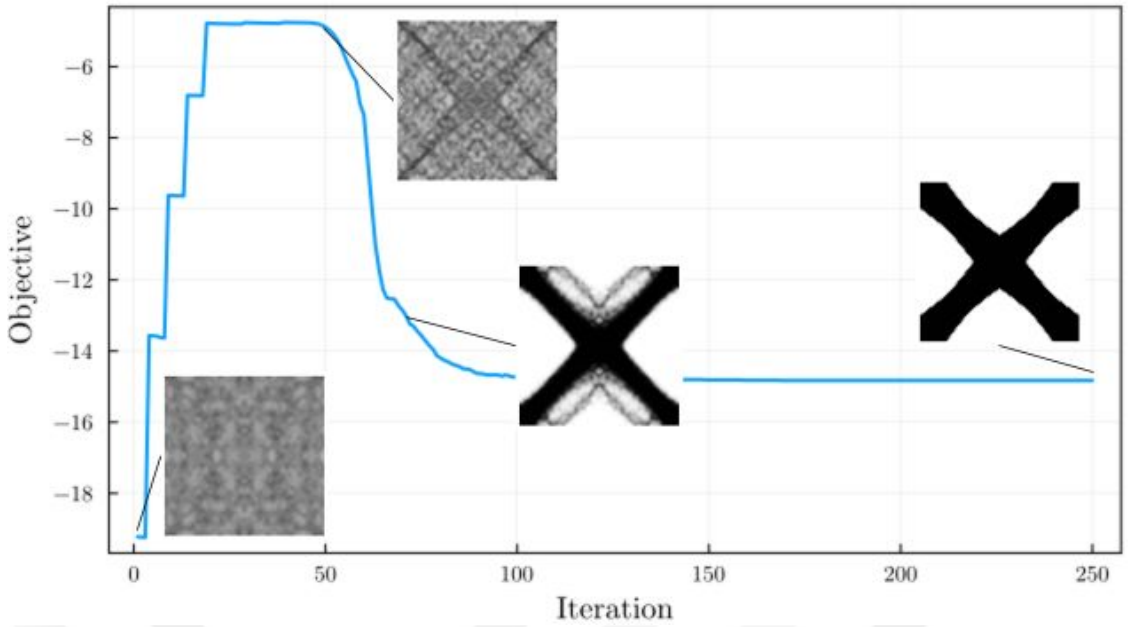

Figure 7.11: Figure illustrating the optimization history, initial topology, intermediate topologies at 50th and 65th iterations and final topology.

Similar to the previous cases, the steps in the evolution of the objective function and the bursts in the volume fraction constraint curve are clearly visible. It is noteworthy again that both the objective function and volume fraction ratio stagnate at almost a constant value after the 150th optimization iteration.

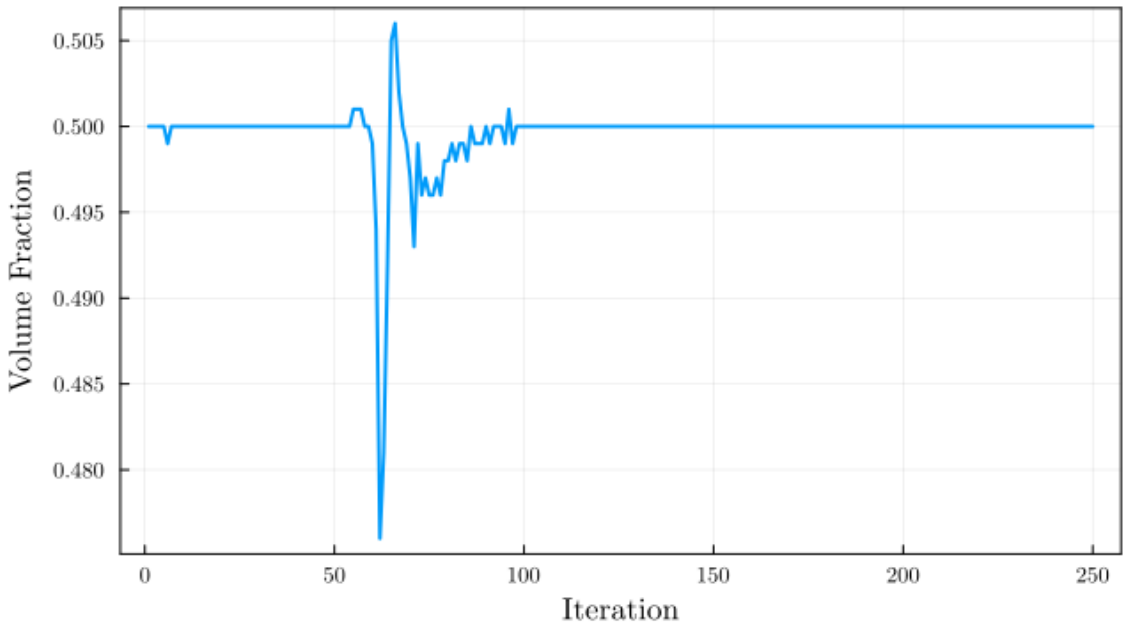

Figure 7.12: Figure illustrating the volume fraction history of the optimization process.

7.3. Maximizing the Bulk Modulus

Bulk modulus can be described as resistance against volume change. Although there exists a different definition of bulk modulus in the context of topology optimization, the particular one used here is given below, along with the constraint on volume fraction.

$$\begin{aligned} \min_{\rho} \quad & -\frac{1}{4}(A_{1111} + A_{2222} + A_{1122} + A_{2211}) \\ \text{subject to} \quad & \frac{1}{|\Omega_m|}\int_{\Omega_m} H_{\beta,\omega}(\widetilde{\rho})\, dv - 0.5 \leq 0 \\ & 0 \leq \rho \leq 1 \end{aligned} \tag{7.4}$$

Table 7.5: Table presenting the parameters used in the optimization process for the current case. Please note that $\beta = 1$ and $p = 1$ values represent the initial value of β. The actual value changes according to the continuation scheme throughout the optimization.

$\mathbf{F}_M$	(L_x, L_y)	$(\text{Nel}_x, \text{Nel}_y)$	(E, ν)	r	p	(β, ω)	$(\hat{\beta}, \hat{\omega})$
$\left[\begin{smallmatrix} 1.05 & 0.00 \\ 0.00 & 1.05 \end{smallmatrix}\right]$	$(2, 2)$	$(80, 80)$	$(100.0, 0.3)$	1.5	1.0	$(1.0, 0.5)$	$(200.0, 0.05)$

(a) (b) (c)

Figure 7.13: (a) Initial design, (b) Optimized design, (c) 3x3 array of optimized design

The optimum topology obtained, please see Figure 7.13, is in agreement with the ones reported in the literature, which is known as Vidgergauz's microstructure after Vidgergauz (Vigdergauz, 1989). It is important to note that this particular problem is very sensitive to the initial design, which could be related (or could be the reason for)

the sudden drop in objective function at the beginning. Volume constraint is very quickly fulfilled with the usual burst observed at early design iterations.

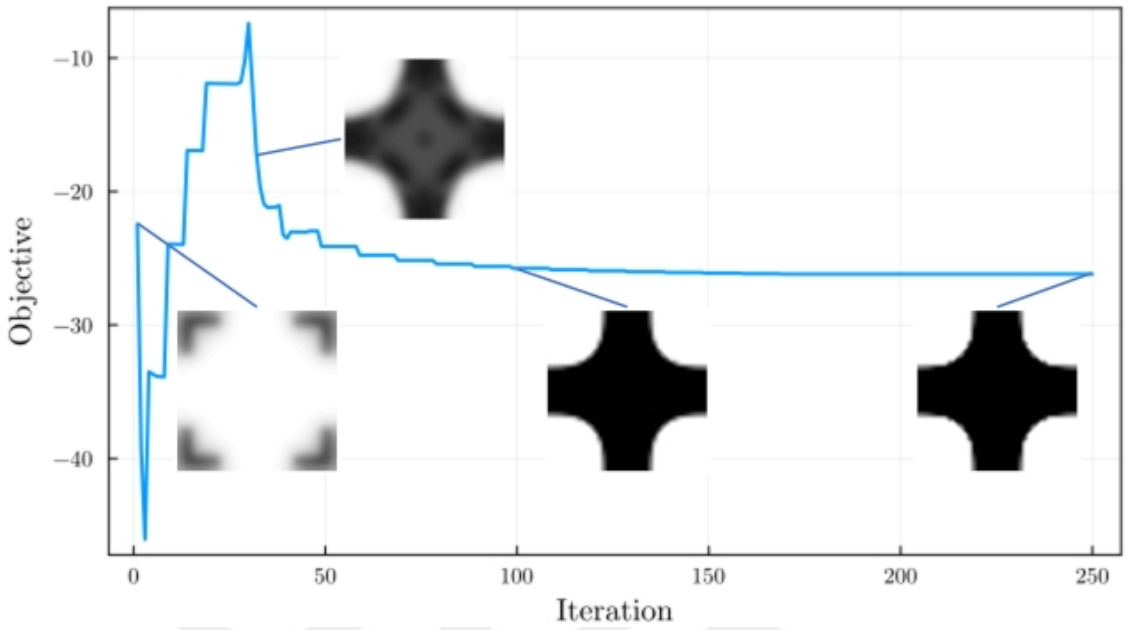

Figure 7.14: Figure illustrating the optimization history, initial topology, intermediate topology at 35th and 100th iterations and final topology.

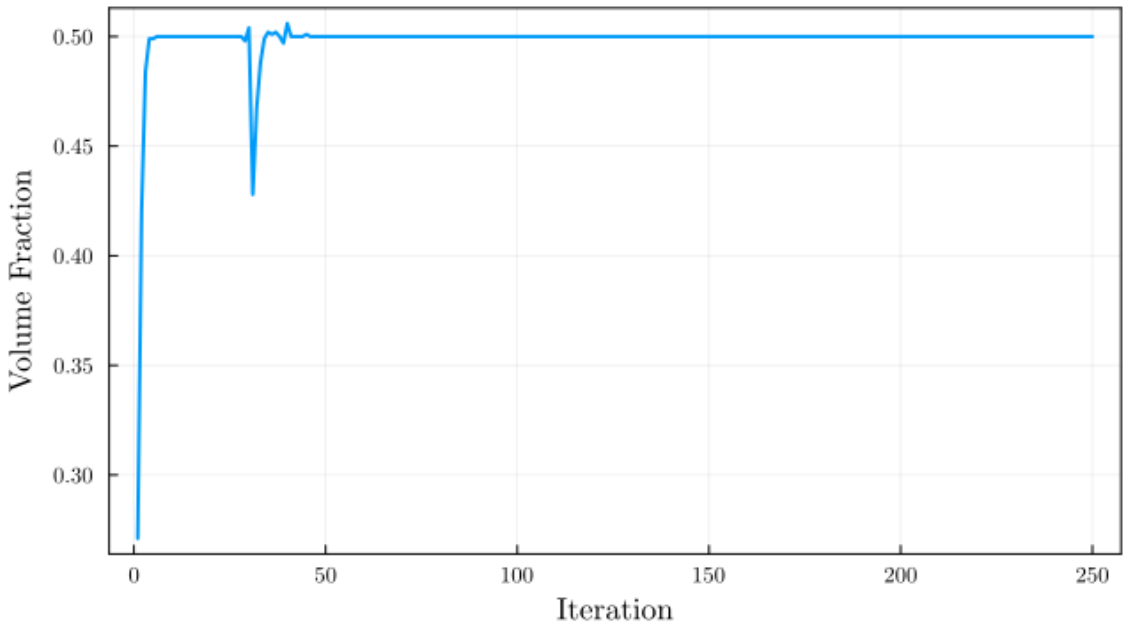

Figure 7.15: Figure illustrating the volume fraction history of the optimization process.

7.4. Negative Poisson's Ratio

One of the most studied subjects in microstructural topology optimization is creating materials with a negative Poisson's ratio. To achieve this, one must choose a suitable Poisson's ratio definition. In this thesis, the following Poisson's ratio definition (Kazemi et al., 2020).

$$\nu_{12} = \frac{2A_{1122}}{(A_{1111} + A_{2222})} \tag{7.5}$$

is used, and the objective function and the volume fraction constraints are defined as

$$\begin{aligned} \min_{\rho} \quad & 100 \cdot (\nu - \nu_0)^2 \\ \text{subject to} \quad & \frac{1}{|\Omega_m|} \int_{\Omega_m} H_{\beta,\omega}(\widetilde{\rho})\, dv - 0.5 \leq 0 \\ & 0 \leq \rho \leq 1 \end{aligned} \tag{7.6}$$

Table 7.6: Table presenting the parameters used in the optimization process for the current case. Please note that $\beta = 1$ and $p = 1$ values represent the initial value of β. The actual value changes according to the continuation scheme throughout the optimization.

$\mathbf{F}_M$	(L_x, L_y)	$(\text{Nel}_x, \text{Nel}_y)$	(E, ν)	r	p	(β, ω)	$(\hat{\beta}, \hat{\omega})$
$\left[\begin{smallmatrix} 1.05 & 0.00 \\ 0.00 & 1.05 \end{smallmatrix}\right]$	$(2, 2)$	$(80, 80)$	$(100.0, 0.3)$	1.5	1.0	$(1.0, 0.5)$	$(200.0, 0.05)$

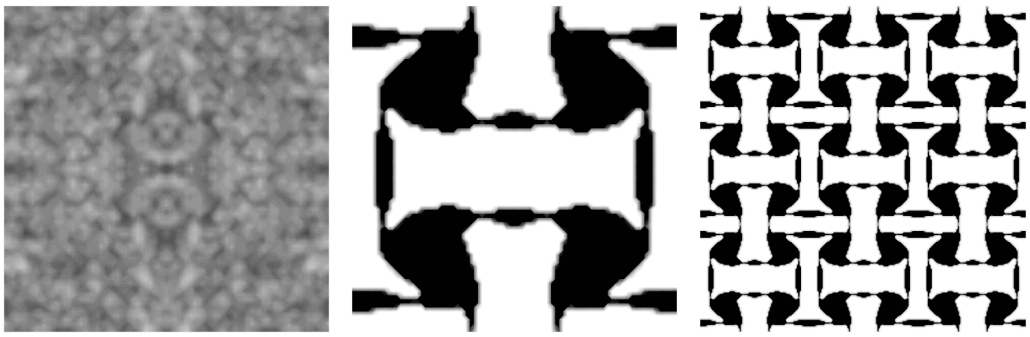

(a) (b) (c)

Figure 7.16: (a) Initial design, (b) Optimized design, (c) 3x3 array of optimized design

Similar to the negative Poisson's ratio unit cells obtained by others, the resulting topology is, in fact, a microstructure with internal flexible hinge-like regions. These flexible hinges allow rotation of the microstructure through which the negative Poisson's ratio effect is achieved. For experimental verification, please see Chapter 8.

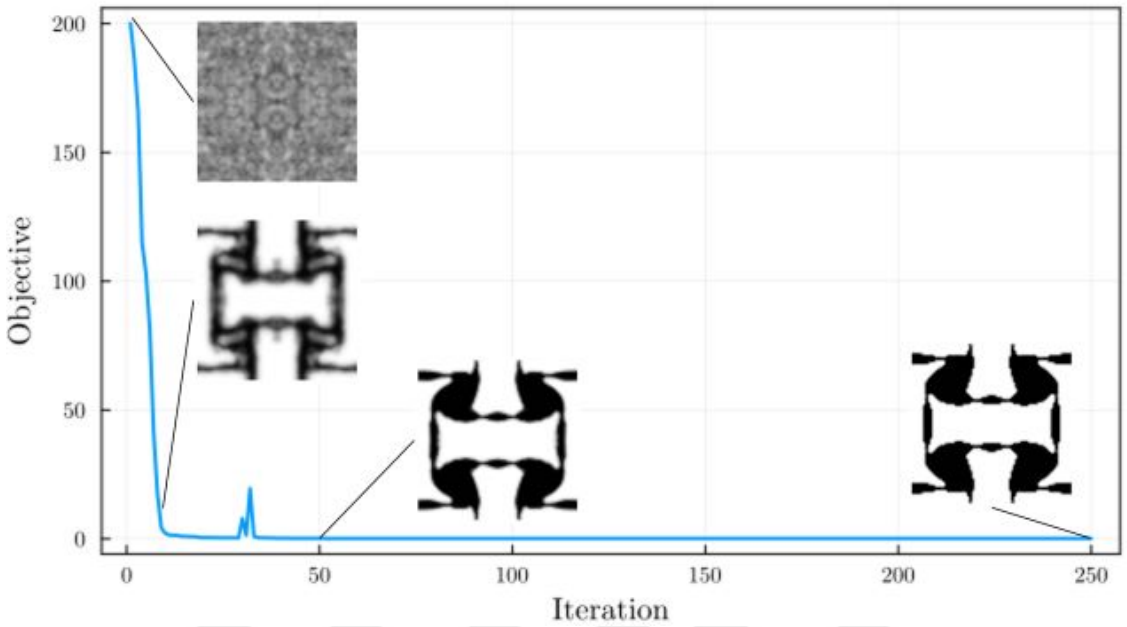

Figure 7.17: Figure illustrating the optimization history, initial topology, intermediate topologies at 10th and 50th iterations and final topology.

Although the evolution of the objective function is relatively smooth in the early iterations, wild fluctuations are observable in the volume fraction evolutions, please see Figure 7.17 and Figure 7.18, respectively. It seems that enforcing the volume constraint and minimizing the objective function is more difficult than in the previous examples. This is partially due to the fact that the optimization process starts with a positive Poisson's ratio, and a sign change has to be realized, which requires a transition of zero Poisson's ratio.

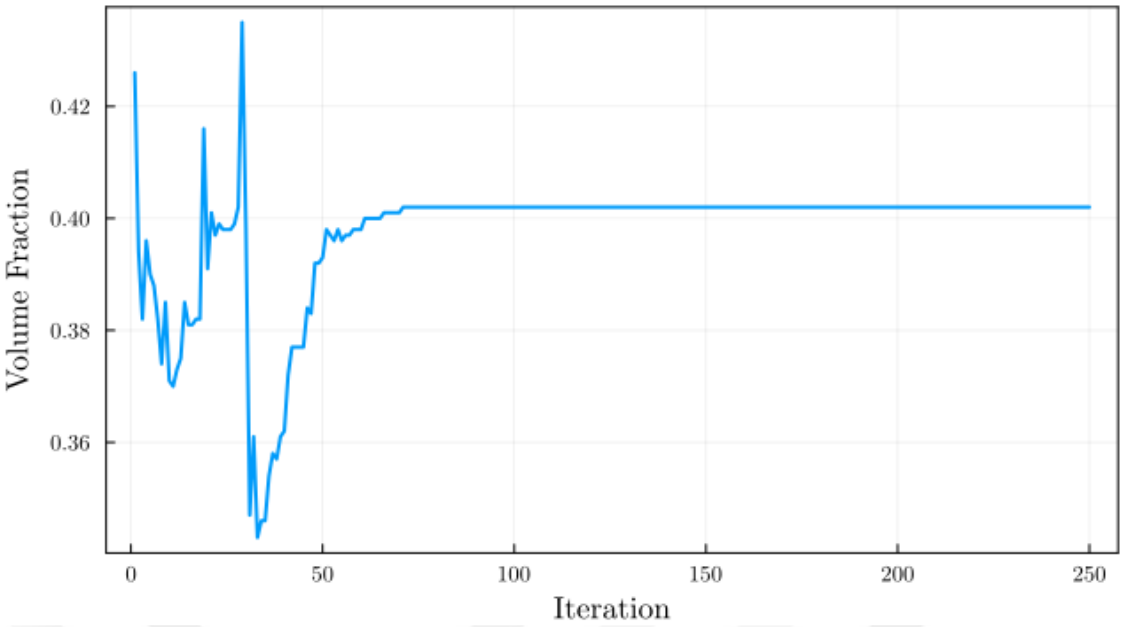

Figure 7.18: Figure illustrating the volume fraction history of the optimization process.

The negative Poisson's ratio problem is particularly suitable to investigate the effect of nonlinear response on resulting optimum topology. This is essentially due to the rather complicated geometry of the optimum unit cell compared to shear stiffness and bulk modulus optimization case studies. To this end, the proposed framework is reduced to a form suitable for optimization with the linear response by following several trivial steps which are not reported here. Using exactly the same objective function and constraint definitions, i.e., Eq.(7.6), the optimization problem is resolved by considering a geometrically and materially linear response. Starting with the same initial design, the obtained optimum topology is presented in Figure 7.19.

(a) (b) (c)

Figure 7.19: (a) Initial design, (b) Optimized design, (c) 3x3 array of optimized design

For comparison purposes, the optimized topologies for linear and nonlinear cases are presented in Figure 7.20

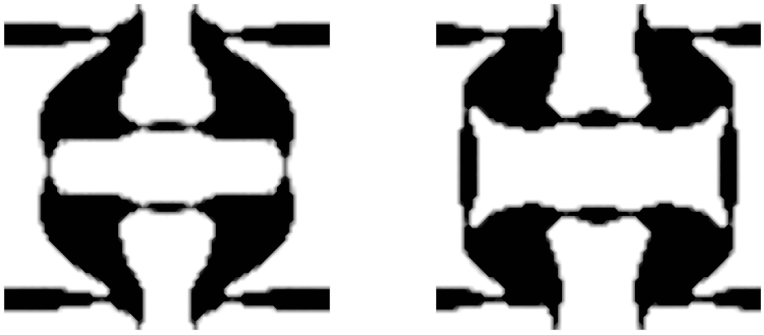

(a) (b)

Figure 7.20: (a) The optimum topology of a unit cell optimized for negative Poisson's ratio under linear behavior, (b) Optimum topology of the same unit cell with identical optimization parameters, under nonlinear behavior.

As can be seen in the figures, the number of flexible hinge-like regions is larger in the case of nonlinear response. Furthermore, although the same filter radius is used for both cases, the thickness of these regions is thicker than the linear response. Relatively larger axial and bending stiffnesses of these regions might be instrumental in transmitting "deformations" to the transverse direction under large displacements.

CHAPTER 8

EXPERIMENTAL VALIDATION

In the previous chapters, topologies with negative Poisson's ratio are obtained using the developed computer programs. Even though these topologies show auxetic behavior numerically, in order to validate their behavior in the real world, experiments are conducted.

For this purpose, using a CAD software, e.g., AutoCAD, the optimum topology is idealized such that it has smooth curves and high resolution. Figure 8.1 illustrates the original and idealized topologies.

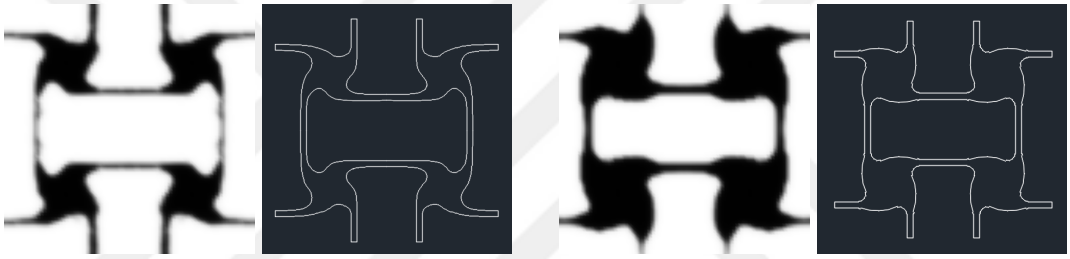

(a) (b) (c) (d)

Figure 8.1: Idealization of the optimum topologies using AutoCAD. Nonlinear topology (a) and its idealization (b). Linear topology (c) and its idealization (d)

Then, idealized topologies are converted into 3D models and 3D printed using a Fused deposition modeling (FDM) printer. For printing the samples, a Polyethylene terephthalate glycol (PETG) filament is preferred as it is readily available and it has more elongation capability compared to an acrylonitrile butadiene styrene (ABS) filament (Sepahi et al., 2021). The 3D printed samples are printed in a 5x5 rectangular grid with 230 mm height, 150 mm width, and thickness of 10 mm. Rigid walls are added to two opposing sides (top and bottom, please see Figure 8.2 and Figure 8.3)

of the sample to ensure that the sample is evenly deformed during the experiment. While the samples undergo deformation, they are recorded by a video camera. This video recording is later used to visually analyze the behavior of the sample. The experiment photos for nonlinear and linear topologies are presented in the following part.

For the experimental validation of the nonlinear topology, the sample is subjected

to tension using an extensometer. It is clear from Figure 8.2 that the 3D printed sample thickens in the direction perpendicular to the loading direction, like an auxetic material under tension, as expected.

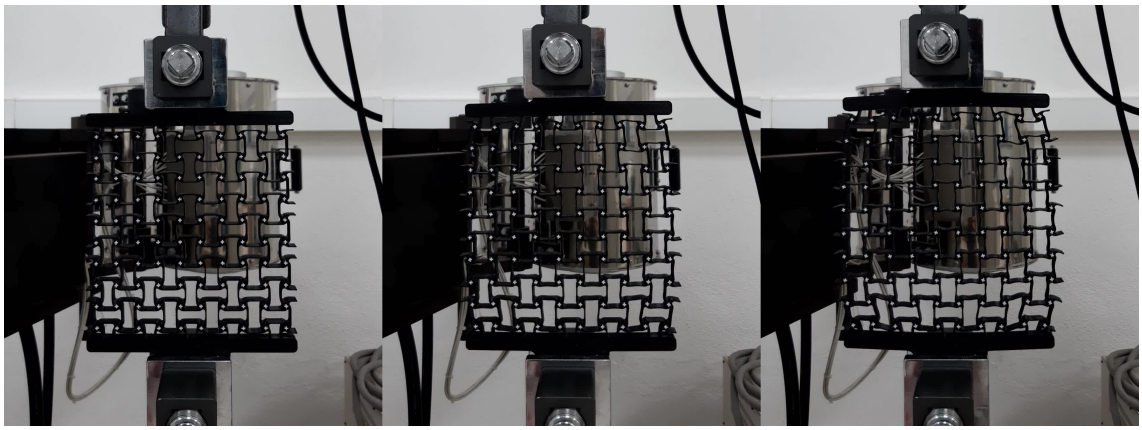

Figure 8.2: Tension test for the 3D printed nonlinear topology.

For the experimental validation of the linear topology, the sample is slowly compressed using a Compression Testing Machine (CTM). It is clear from Figure 8.3, that the 3D printed sample gets thinner in the direction perpendicular to the loading direction, like an auxetic material under compression, as expected.

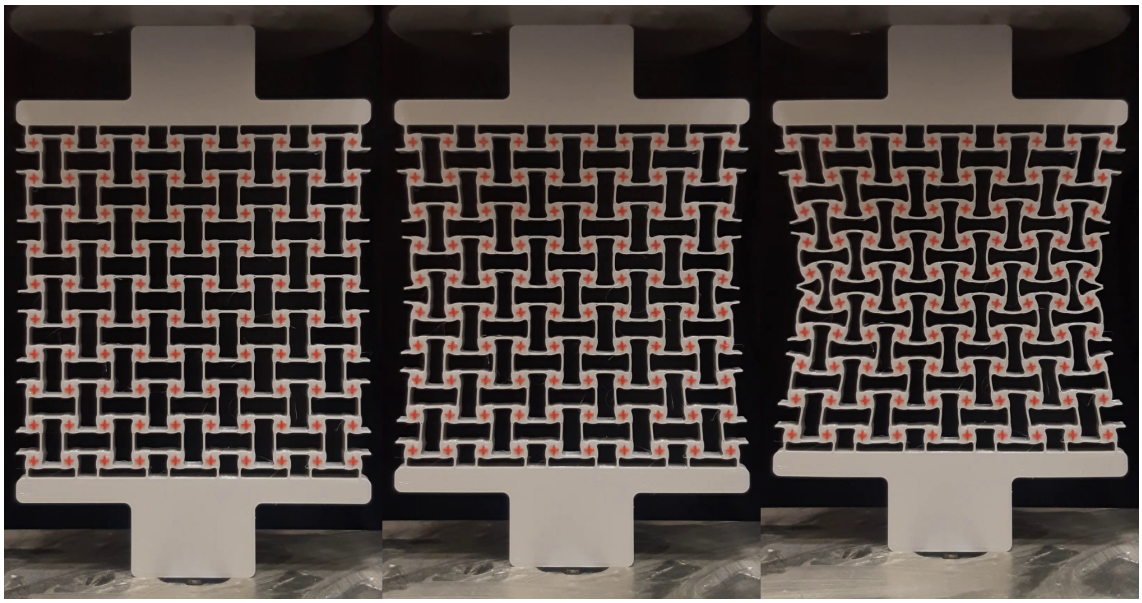

Figure 8.3: Compression test for the 3D printed linear topology.

The intention of the cross-shaped markers on the samples was to calculate the strain field through post-processing of video recordings, similar to Digital Image Correlation (DIC) systems. This process requires dedicated and reliable software which can handle regular grids of markers. This task is tried by means of freely available Matlab-based software, but it turned out that the resulting Poisson's ratio is very sensitive to the region selected for calculation purposes and may easily lead to large differences even a small change, i.e., in the order of few pixels, my easily lead to large differences in the calculated Poisson's ratio. Because of this reason, this step is not presented here and is left as a potential future extension of the study.

CHAPTER 9

CONCLUSION & OUTLOOK

9.1. Summary and Recommendations for Future Work

Although microstructural optimization has been an active research field for several decades, the number of studies considering geometric and material nonlinearities is limited. Departing from this point, this thesis focused on the topology optimization of microstructures with a nonlinear elastic solid phase. Developing an optimization framework and its implementation requires a coherent combination of several components.

Based on the theoretical framework presented by Wallin and Tortorelli (Wallin & Tortorelli, 2020), nonlinear homogenization and adjoint-based sensitivity analysis are combined together within a gradient and density-based topology optimization framework. To update the design variables, a globally convergent version of the method of moving asymptotes (GCMMA) (Svanberg, 2002) is used. A finite element-based topology optimization program is developed in the Julia programming language. Several case studies are considered typically addressed in the literature, including a negative Poisson ratio microstructure.

As an original contribution, the symmetry properties of the resulting orthotropic topologies are exploited to reduce the computational domain by half. This clearly leads to very significant savings in computational time, which is particularly important for optimization with nonlinear response.

As a validation step, optimized microstructures are converted into printable formats, and compression and tension specimens are manufactured using 3D printing. These proof-of-concept type experiments reveal that the physical specimens, in fact, have the expected auxetic behavior.

There are countless ways to enhance and expand the work that is presented in this thesis.

- First of all, instead of a two-dimensional plane-strain formulation, a truly three-dimensional unit cell optimization problem would be considered. Theoretically, this extension requires minimal effort on top of what is presented in this thesis.

Clearly, the computational cost would increase significantly. However, it could be an ideal problem to test and highlight the computational gain achieved by the domain reduction technique presented in Chapter 6.

- The effect of material and geometric nonlinearity is illustrated in Chapter 7. It would be an exciting extension to investigate the effect of different energy density functions on the resulting optimum microstructure. Embedding different elasticity models into the current formulation and the developed code is not a complicated task once the expressions for stress and tangent stiffnesses are obtained.

- The experimental validation presented in Chapter 8 is very limited in scope. It has a qualitative character, and in the future, measurements should be digitized with the aid of reliable digital image correlation software.

- The type of constraint equations considered in this thesis is limited to volume fraction constraint on the solid phase. Different kinds of constraints, particularly stress-based ones, can be considered in the future. One of the critical components, namely sensitivities of stress components, is already presented in this thesis. Therefore this extension seems to be realizable.

- Obviously, there are several different engineering properties for which an optimum microstructure is sought. Therefore the presented work here, particularly the developed code, could be adapted for various field problems, such as thermal conductivity, and can be extended for coupled field problems.

- An extensive parametric study investigating the effect of the initial design, MMA parameters, density filter, and Helmholtz filter parameters must be carried out, particularly for optimization with the nonlinear response.

REFERENCES

Aage, N., Andreassen, E., Lazarov, B. S., & Sigmund, O. (2017). Giga-voxel computational morphogenesis for structural design. *Nature*, *550*(7674), 84–86. https://doi.org/10.1038/nature23911

Abbott, M., Dilum Aluthge, N3N5, Schaub, S., Elrod, C., Lucibello, C., & Chen, J. (2022). Mcabbott/tullio.jl: V0.3.5. https://doi.org/10.5281/ZENODO.7106192

Alexandersen, J., Sigmund, O., Meyer, K. E., & Lazarov, B. S. (2018). Design of passive coolers for light-emitting diode lamps using topology optimisation. *International Journal of Heat and Mass Transfer*, *122*, 138–149. https://doi.org/10.1016/j.ijheatmasstransfer.2018.01.103

Attaran, M. (2017). The rise of 3-d printing: The advantages of additive manufacturing over traditional manufacturing. *Business Horizons*, *60*(5), 677–688. https://doi.org/10.1016/j.bushor.2017.05.011

Bendsøe, M. P., & Sigmund, O. (1999). Material interpolation schemes in topology optimization. *Archive of applied mechanics*, *69*, 635–654.

Bendsøe, M. P., & Sigmund, O. (2004). *Topology optimization: Theory, methods, and applications*. Springer Berlin Heidelberg. https://doi.org/10.1007/978-3-662-05086-6

Bendsøe, M. P., & Kikuchi, N. (1988). Generating optimal topologies in structural design using a homogenization method. *Computer Methods in Applied Mechanics and Engineering*, *71*(2), 197–224. https://doi.org/10.1016/0045-7825(88)90086-2

Bezanson, J., Edelman, A., Karpinski, S., & Shah, V. B. (2017). Julia: A fresh approach to numerical computing. *SIAM Review*, *59*(1), 65–98. https://doi.org/10.1137/141000671

Bignonnet, F., Hassen, G., & Dormieux, L. (2016). Fourier-based strength homogenization of porous media. *Computational Mechanics*, *58*(5), 833–859. https://doi.org/10.1007/s00466-016-1319-6

Blanco, P. J., Sánchez, P. J., de Souza Neto, E. A., & Feijóo, R. A. (2014). Variational foundations and generalized unified theory of RVE-based multiscale models. *Archives of Computational Methods in Engineering*, *23*(2), 191–253. https://doi.org/10.1007/s11831-014-9137-5

Bonet, J., & Wood, R. D. (2008). *Nonlinear continuum mechanics for finite element analysis*. Cambridge University Press. https://doi.org/10.1017/cbo9780511755446

Briseghella, B., Fenu, L., Lan, C., Mazzarolo, E., & Zordan, T. (2013). Application of topological optimization to bridge design. *Journal of Bridge Engineering*, *18*(8), 790–800. https://doi.org/10.1061/(asce)be.1943-5592.0000416

Christ, S., Schwabeneder, D., Rackauckas, C., Borregaard, M. K., & Breloff, T. (2022). Plots.jl – a user extendable plotting api for the julia programming language. https://doi.org/10.48550/ARXIV.2204.08775

Christensen, P. W., & Klarbring, A. (2008). *An introduction to structural optimization* (2009th ed.). Springer.

Dalklint, A., Wallin, M., Bertoldi, K., & Tortorelli, D. (2022). Tunable phononic bandgap materials designed via topology optimization. *Journal of the Mechanics and Physics of Solids*, *163*, 104849. https://doi.org/10.1016/j.jmps.2022.104849

de Souza Neto, E., Blanco, P., Sanchez, P., & Feijoo, R. (2015). An RVE-based multiscale theory of solids with micro-scale inertia and body force effects. *Mechanics of Materials*, *80*, 136–144. https://doi.org/10.1016/j.mechmat.2014.10.007

Diaz, A. R., & Sigmund, O. (2009). A topology optimization method for design of negative permeability metamaterials. *Structural and Multidisciplinary Optimization*, *41*(2), 163–177. https://doi.org/10.1007/s00158-009-0416-y

Drago, A., & Pindera, M. (2007). Micro-macromechanical analysis of heterogeneous materials: Macroscopically homogeneous vs periodic microstructures. *Composites Science and Technology*, *67*(6), 1243–1263. https://doi.org/10.1016/j.compscitech.2006.02.031

Errico, R. M. (1997). What is an adjoint model? *Bulletin of the American Meteorological Society*, *78*(11), 2577–2591. https://doi.org/10.1175/1520-0477(1997)078<2577:wiaam>2.0.co;2

Fanni, M., Shabara, N., & Alkalla, M. (2013). A comparison between different topology optimization methods. *Engineering Journal*, *38*.

Ford, S., & Despeisse, M. (2016). Additive manufacturing and sustainability: An exploratory study of the advantages and challenges. *Journal of Cleaner Production*, *137*, 1573–1587. https://doi.org/10.1016/j.jclepro.2016.04.150

Giles, M. B., & Pierce, N. A. (2000). *Flow, Turbulence and Combustion*, *65*(3/4), 393–415. https://doi.org/10.1023/a:1011430410075

Gu, Q., & Wang, G. (2013). Direct differentiation method for response sensitivity analysis of a bounding surface plasticity soil model. *Soil Dynamics and Earthquake Engineering*, *49*, 135–145. https://doi.org/10.1016/j.soildyn.2013.01.028

Hill, R. (1963). Elastic properties of reinforced solids: Some theoretical principles. *Journal of the Mechanics and Physics of Solids*, *11*(5), 357–372. https://doi.org/10.1016/0022-5096(63)90036-x

Javaid, M., Haleem, A., Singh, R. P., Suman, R., & Rab, S. (2021). Role of additive manufacturing applications towards environmental sustainability. *Advanced Industrial and Engineering Polymer Research*.

Johnson, S. G. (n.d.). NLopt.jl: The nlopt nonlinear-optimization package. http://https://github.com/JuliaOpt/NLopt.jl

Kamiński, B., White, J. M., Bouchet-Valat, M., powerdistribution, Garborg, S., Quinn, J., Kornblith, S., cjprybol, Stukalov, A., Bates, D., Short, T., DuBois, C., Harris, H., Squire, K., Arslan, A., pdeffebach, Anthoff, D., Kleinschmidt, D., Noack, A., . . . Oswald, F. (2023). *Juliadata/dataframes.jl: V1.5.0* (Version v1.5.0). Zenodo. https://doi.org/10.5281/zenodo.7632427

Kato, J., Yachi, D., Terada, K., & Kyoya, T. (2013). Topology optimization of micro-structure for composites applying a decoupling multi-scale analysis. *Structural and Multidisciplinary Optimization*, *49*(4), 595–608. https://doi.org/10.1007/s00158-013-0994-6

Kazemi, H., Vaziri, A., & Norato, J. A. (2020). Multi-material topology optimization of lattice structures using geometry projection. *Computer Methods in Applied Mechanics and Engineering*, *363*, 112895. https://doi.org/10.1016/j.cma.2020.112895

Kollmann, H. T., Abueidda, D. W., Koric, S., Guleryuz, E., & Sobh, N. A. (2020). Deep learning for topology optimization of 2d metamaterials. *Materials & Design*, *196*, 109098. https://doi.org/10.1016/j.matdes.2020.109098

Lanckriet, G., & Sriperumbudur, B. K. (1970). On the convergence of the concave-convex procedure. https://papers.nips.cc/paper/3646-on-the-convergence-of-the-concave-convex-procedure

Lazarov, B. S., & Sigmund, O. (2010). Filters in topology optimization based on helmholtz-type differential equations. *International Journal for Numerical Methods in Engineering*, *86*(6), 765–781. https://doi.org/10.1002/nme.3072

Li, L., & Khandelwal, K. (2015). Volume preserving projection filters and continuation methods in topology optimization. *Engineering Structures*, *85*, 144–161. https://doi.org/10.1016/j.engstruct.2014.10.052

Liang, Y., & Cheng, G. (2019). Topology optimization via sequential integer programming and canonical relaxation algorithm. *Computer Methods in Applied Mechanics and Engineering*, *348*, 64–96. https://doi.org/10.1016/j.cma.2018.10.050

Lin, D., White, J. M., Byrne, S., Bates, D., Noack, A., Pearson, J., Arslan, A., Squire, K., Anthoff, D., Papamarkou, T., Besançon, M., Drugowitsch, J., Schauer, M., & other contributors. (2019). JuliaStats/Distributions.jl: a Julia package for probability distributions and associated functions. https://doi.org/10.5281/zenodo.2647458

Mandel, J. (1971). Plasticité classique et viscoplasticité (cism lecture notes, udine, italy).

Martinez-Frutos, J., Martinez-Castejon, P. J., & Herrero-Perez, D. (2017). Efficient topology optimization using GPU computing with multilevel granularity. *Advances in Engineering Software*, *106*, 47–62. https://doi.org/10.1016/j.advengsoft.2017.01.009

Maxwell, J. C. (1870). I.—on reciprocal figures, frames, and diagrams of forces. *Earth and Environmental Science Transactions of The Royal Society of Edinburgh*, *26*(1), 1–40. https://doi.org/10.1017/S0080456800026351

Michell, A. (1904). LVIII.the limits of economy of material in frame-structures. *The London, Edinburgh, and Dublin Philosophical Magazine and Journal of Science*, *8*(47), 589–597. https://doi.org/10.1080/14786440409463229

Mizzi, L., Attard, D., Gatt, R., Dudek, K. K., Ellul, B., & Grima, J. N. (2020). Implementation of periodic boundary conditions for loading of mechanical metamaterials and other complex geometric microstructures using finite element analysis. *Engineering with Computers*. https://doi.org/10.1007/s00366-019-00910-1

Neves, M. M., Sigmund, O., & Bendsøe, M. P. (2002). Topology optimization of periodic microstructures with a penalization of highly localized buckling modes. *International Journal for Numerical Methods in Engineering*, *54*(6), 809–834. https://doi.org/10.1002/nme.449

Neves, M., Rodrigues, H., & Guedes, J. (2000). Optimal design of periodic linear elastic microstructures. *Computers & Structures*, *76*(1-3), 421–429. https://doi.org/10.1016/s0045-7949(99)00172-8

Ohno, N., Matsuda, T., & Wu, X. (2001). A homogenization theory for elastic–viscoplastic composites with point symmetry of internal distributions. *International Journal of Solids and Structures*, *38*(16), 2867–2878.

Querin, O., Steven, G., & Xie, Y. (1998). Evolutionary structural optimisation (ESO) using a bidirectional algorithm. *Engineering Computations*, *15*(8), 1031–1048. https://doi.org/10.1108/02644409810244129

Radman, A., Huang, X., & Xie, Y. (2012). Topological optimization for the design of microstructures of isotropic cellular materials. *Engineering Optimization*, *45*(11), 1331–1348. https://doi.org/10.1080/0305215x.2012.737781

Saavedra Flores, E., & de Souza Neto, E. (2010). Remarks on symmetry conditions in computational homogenisation problems. *Engineering Computations*, *27*(4), 551–575.

Sepahi, M. T., Abusalma, H., Jovanovic, V., & Eisazadeh, H. (2021). Mechanical properties of 3d-printed parts made of polyethylene terephthalate glycol. *Journal of Materials Engineering and Performance*, *30*(9), 6851–6861. https://doi.org/10.1007/s11665-021-06032-4

Sigmund, O., & Torquato, S. (1997). Design of materials with extreme thermal expansion using a three-phase topology optimization method. *Journal of the Mechanics and Physics of Solids*, *45*(6), 1037–1067. https://doi.org/10.1016/s0022-5096(96)00114-7

Svanberg, K. (1987). The method of moving asymptotes—a new method for structural optimization. *International Journal for Numerical Methods in Engineering*, *24*(2), 359–373. https://doi.org/10.1002/nme.1620240207

Svanberg, K. (2002). A class of globally convergent optimization methods based on conservative convex separable approximations. *SIAM Journal on Optimization*, *12*(2), 555–573. https://doi.org/10.1137/s1052623499362822

Tarek, M. (2023). Nonconvex.jl: A comprehensive julia package for non-convex optimization. https://doi.org/10.13140/RG.2.2.36120.37121

Tcherniak, D. (2002). Topology optimization of resonating structures using simp method. *International Journal for Numerical Methods in Engineering*, *54*(11), 1605–1622.

Tortorelli, D. A., & Michaleris, P. (1994). Design sensitivity analysis: Overview and review. *Inverse Problems in Engineering*, *1*(1), 71–105. https://doi.org/10.1080/174159794088027573

Vatanabe, S. L., Lippi, T. N., de Lima, C. R., Paulino, G. H., & Silva, E. C. (2016). Topology optimization with manufacturing constraints: A unified

projection-based approach. *Advances in Engineering Software*, *100*, 97–112. https://doi.org/10.1016/j.advengsoft.2016.07.002

Vigdergauz, S. (1989). Regular structures with extremal elastic properties. *Mechanics of Solids*, *24*(3), 57–63.

Vogiatzis, P., Chen, S., Wang, X., Li, T., & Wang, L. (2017). Topology optimization of multi-material negative poisson's ratio metamaterials using a reconciled level set method. *Computer-Aided Design*, *83*, 15–32. https://doi.org/10.1016/j.cad.2016.09.009

Wallin, M., & Tortorelli, D. A. (2020). Nonlinear homogenization for topology optimization. *Mechanics of Materials*, *145*, 103324. https://doi.org/10.1016/j.mechmat.2020.103324

Wang, F., Sigmund, O., & Jensen, J. (2014). Design of materials with prescribed nonlinear properties. *Journal of the Mechanics and Physics of Solids*, *69*, 156–174. https://doi.org/10.1016/j.jmps.2014.05.003

Wang, F. (2018). Systematic design of 3d auxetic lattice materials with programmable poisson's ratio for finite strains. *Journal of the Mechanics and Physics of Solids*, *114*, 303–318. https://doi.org/10.1016/j.jmps.2018.01.013

Wang, M. Y., Wang, X., & Guo, D. (2003). A level set method for structural topology optimization. *Computer Methods in Applied Mechanics and Engineering*, *192*(1-2), 227–246. https://doi.org/10.1016/s0045-7825(02)00559-5

Wang, Y., & Sigmund, O. (2023). Multi-material topology optimization for maximizing structural stability under thermo-mechanical loading. *Computer Methods in Applied Mechanics and Engineering*, *407*, 115938. https://doi.org/10.1016/j.cma.2023.115938

Wang, Y., Gao, J., Luo, Z., Brown, T., & Zhang, N. (2016). Level-set topology optimization for multimaterial and multifunctional mechanical metamaterials. *Engineering Optimization*, *49*(1), 22–42. https://doi.org/10.1080/0305215x.2016.1164853

Watts, S., & Tortorelli, D. A. (2016). An n-material thresholding method for improving integerness of solutions in topology optimization. *International Journal for Numerical Methods in Engineering*, *108*(12), 1498–1524. https://doi.org/10.1002/nme.5265

Xia, L., & Breitkopf, P. (2014). Concurrent topology optimization design of material and structure within fe2 nonlinear multiscale analysis framework. *Computer Methods*

in Applied Mechanics and Engineering, *278*, 524–542. https://doi.org/10.1016/j.cma.2014.05.022

Xia, L., & Breitkopf, P. (2015). Design of materials using topology optimization and energy-based homogenization approach in matlab. *Structural and Multidisciplinary Optimization*, *52*(6), 1229–1241. https://doi.org/10.1007/s00158-015-1294-0

Xie, Y. M., & Steven, G. P. (1997). *Evolutionary structural optimization*. Springer London. https://doi.org/10.1007/978-1-4471-0985-3

Xie, Y., & Steven, G. (1993). A simple evolutionary procedure for structural optimization. *Computers & Structures*, *49*(5), 885–896. https://doi.org/10.1016/0045-7949(93)90035-c

Zhang, X., & Zhu, B. (2018). *Topology optimization of compliant mechanisms* (1st ed.). Springer.

Zhang, Y., Xiao, M., Li, H., & Gao, L. (2019). Topology optimization of material microstructures using energy-based homogenization method under specified initial material layout. *Journal of Mechanical Science and Technology*, *33*(2), 677–693. https://doi.org/10.1007/s12206-019-0123-6

Zhu, B., Skouras, M., Chen, D., & Matusik, W. (2017). Two-scale topology optimization with microstructures. *ACM Transactions on Graphics*, *36*(4), 1. https://doi.org/10.1145/3072959.3095815

ZHU, J., ZHOU, H., WANG, C., ZHOU, L., YUAN, S., & ZHANG, W. (2021). A review of topology optimization for additive manufacturing: Status and challenges. *Chinese Journal of Aeronautics*, *34*(1), 91–110. https://doi.org/10.1016/j.cja.2020.09.020

Zuo, W., & Saitou, K. (2017). Multi-material topology optimization using ordered simp interpolation. *Structural and Multidisciplinary Optimization*, *55*, 477–491.

APPENDIX A

Derivations

A.1. Homogenization Operator

Homogenization of microscopic total displacements is as follows.

$$\begin{aligned}
\mathcal{H}(\mathbf{u}_m) &= \frac{1}{|\Omega_m|}\int_{\Omega_m} \mathbf{u}_m(\mathbf{y})\, dv \\
&= \frac{1}{|\Omega_m|}\int_{\Omega_m} (\overline{\mathbf{u}}_m(\mathbf{y}) + \widetilde{\mathbf{u}}_m(\mathbf{y}))\, dv \\
&= \frac{1}{|\Omega_m|}\int_{\Omega_m} \overline{\mathbf{u}}_m(\mathbf{y})\, dv + \frac{1}{|\Omega_m|}\int_{\Omega_m} \widetilde{\mathbf{u}}_m(\mathbf{y})\, \mathrm{dv} \\
&= \frac{1}{|\Omega_m|}\int_{\Omega_m} (\mathbf{u}_M(\mathbf{x}) + \nabla_x \mathbf{u}_M \cdot \mathbf{y})\, dv + \frac{1}{|\Omega_m|}\int_{\Omega_m} \widetilde{\mathbf{u}}_m(\mathbf{y})\, dv \\
&= \frac{1}{|\Omega_m|}\int_{\Omega_m} \mathbf{u}_M(\mathbf{x})\, dv + \frac{1}{|\Omega_m|}\int_{\Omega_m} \nabla_x \mathbf{u}_M \cdot \mathbf{y}\, dv + \frac{1}{|\Omega_m|}\int_{\Omega_m} \widetilde{\mathbf{u}}_m(\mathbf{y})\, dv \\
&= \mathbf{u}_M(\mathbf{x}) \cdot \frac{1}{|\Omega_m|}\int_{\Omega_m} dv + \nabla_x \mathbf{u}_M \cdot \frac{1}{|\Omega_m|}\int_{\Omega_m} \mathbf{y}\, dv + \frac{1}{|\Omega_m|}\int_{\Omega_m} \widetilde{\mathbf{u}}_m(\mathbf{y})\, dv \\
&= \mathbf{u}_M(\mathbf{x}) + \nabla_x \mathbf{u}_M \cdot \frac{1}{|\Omega_m|}\int_{\Omega_m} \mathbf{y}\, dv + \frac{1}{|\Omega_m|}\int_{\Omega_m} \widetilde{\mathbf{u}}_m(\mathbf{y})\, dv
\end{aligned} \tag{A.1}$$

Homogenization of gradient of microscopic total displacements is as follows.

$$\begin{aligned}
\mathcal{H}(\nabla_y \mathbf{u}_m) &= \frac{1}{|\Omega_m|}\int_{\Omega_m} \nabla_y \mathbf{u}_m(\mathbf{y})\, dv \\
&= \frac{1}{|\Omega_m|}\int_{\Omega_m} (\nabla_y \overline{\mathbf{u}}_m(\mathbf{y}) + \nabla_y \widetilde{\mathbf{u}}_m(\mathbf{y}))\, dv \\
&= \frac{1}{|\Omega_m|}\int_{\Omega_m} \nabla_y \overline{\mathbf{u}}_m(\mathbf{y})\, dv + \frac{1}{|\Omega_m|}\int_{\Omega_m} \nabla_y \widetilde{\mathbf{u}}_m(\mathbf{y})\, \mathrm{dv} \\
&= \frac{1}{|\Omega_m|}\int_{\Omega_m} (\nabla_y \mathbf{u}_M(\mathbf{x}) + \nabla_y(\nabla_x \mathbf{u}_M \cdot \mathbf{y}))\, dv + \frac{1}{|\Omega_m|}\int_{\Omega_m} \nabla_y \widetilde{\mathbf{u}}_m(\mathbf{y})\, dv \\
&= \frac{1}{|\Omega_m|}\int_{\Omega_m} \nabla_x \mathbf{u}_M\, dv + \frac{1}{|\Omega_m|}\int_{\Omega_m} \nabla_y \widetilde{\mathbf{u}}_m(\mathbf{y})\, dv \\
&= \nabla_y \mathbf{u}_M(\mathbf{x}) \cdot \frac{1}{|\Omega_m|}\int_{\Omega_m} dv + \frac{1}{|\Omega_m|}\int_{\Omega_m} \nabla_y \widetilde{\mathbf{u}}_m(\mathbf{y})\, dv \\
&= \nabla_y \mathbf{u}_M(\mathbf{x}) + \frac{1}{|\Omega_m|}\int_{\Omega_m} \nabla_y \widetilde{\mathbf{u}}_m(\mathbf{y})\, dv
\end{aligned} \tag{A.2}$$

A.2. Divergence of $\mathbf{v} \cdot \mathbf{P}_m$

Consider a vector $\mathbf{v}$, the divergence of the dot product of this vector and $\mathbf{P}_m$ can be written as the double dot product of $\mathbf{P}_m$ and the gradient of $\mathbf{v}$

$$\begin{aligned}
\nabla_y \cdot (\mathbf{v} \cdot \mathbf{P}_m) &= \nabla_y \cdot (\mathbf{v} \cdot \mathbf{P}_m) : \mathbf{I} \\
&= \frac{\partial (v_i (P_m)_{ij})}{\partial y_k} (\mathbf{e}_j \otimes \mathbf{e}_k) : \delta_{pq} (\mathbf{e}_p \otimes \mathbf{e}_q) \\
&= \frac{\partial (v_i (P_m)_{ij})}{\partial y_k} \delta_{pq} \delta_{jp} \delta_{kq} \\
&= \frac{\partial v_i}{\partial y_j} (P_m)_{ij} + v_i \underbrace{\frac{\partial (P_m)_{ij}}{\partial y_j}}_{\nabla_y \cdot \mathbf{P}_m = 0} \\
&= \mathbf{P}_m : \nabla_y \mathbf{v}
\end{aligned} \tag{A.3}$$

A.3. Indicial Form of $\mathbf{A}_M$

The homogenized tangent stiffness tensor, $\mathbf{A}_M$ can be expressed in the indicial form by the following procedure.

$$\begin{aligned}
(\mathbf{A}_M)_{mnrs} &= \mathbf{E}_{mn} \cdot \mathbf{A}_M \cdot \mathbf{E}_{rs} \\
&= \mathbf{E}_{mn} \cdot \frac{1}{|\Omega_m|} \int_{\Omega_m} \mathbf{A}_m \cdot \left(\mathbf{E}_{ij} \otimes \mathbf{E}_{ij} + \nabla_y \widetilde{\chi}_m^{(ij)} \otimes \mathbf{E}_{ij} \right) dv \cdot \mathbf{E}_{rs} \\
&= \frac{1}{|\Omega_m|} \int_{\Omega_m} \mathbf{E}_{mn} \cdot \mathbf{A}_m \cdot \left(\mathbf{E}_{rs} + \nabla_y \widetilde{\chi}_m^{(rs)} \right) dv
\end{aligned} \tag{A.4}$$

One can transform Eq.(A.4) into a more common form in the literature (M. Neves et al., 2000) by adding the following equality into Eq.(A.4)

$$\frac{1}{|\Omega_m|} \int_{\Omega_m} \nabla_y \widetilde{\chi}_m^{(mn)} \cdot \mathbf{A}_m \cdot \left(\mathbf{E}_{rs} + \nabla_y \widetilde{\chi}_m^{(rs)} \right) dv = 0 \tag{A.5}$$

thus, Eq.(A.4) becomes

$$(\mathbf{A}_M)_{mnrs} = \frac{1}{|\Omega_m|} \int_{\Omega_m} \left(\mathbf{E}_{mn} + \nabla_y \widetilde{\chi}_m^{(mn)} \right) \cdot \mathbf{A}_m \cdot \left(\mathbf{E}_{rs} + \nabla_y \widetilde{\chi}_m^{(rs)} \right) dv \tag{A.6}$$

This expression can also be rewritten in terms of total incremental displacements,

$\chi_m^{(mn)}$ as follows

$$(\mathbf{A}_M)_{mnrs} = \frac{1}{|\Omega_m|}\int_{\Omega_m} \nabla_y \chi_m^{(mn)} \cdot \mathbf{A}_m \cdot \nabla_y \chi_m^{(rs)}\, dv \tag{A.7}$$

A.4. Variation of $\theta_A(\rho;\delta\rho)$

Adding Eq.(4.11) and Eq.(4.13) together, transforms $\delta\theta_A(\rho;\delta\rho)$ into following form

$$\begin{aligned}
\delta\theta_A(\rho;\delta\rho) = \frac{1}{|\Omega_m|}\int_{\Omega_m} \Bigg(& \mathbf{E}_{ij} \cdot \delta\mathbf{A}_m(\mathbf{F}_m,\rho;\delta\rho) \cdot \nabla_y \chi_m^{(rs)}(\rho) \\
& + \mathbf{E}_{ij} \cdot \frac{\partial \mathbf{A}_m(\mathbf{F}_m,\rho)}{\partial \mathbf{F}_m} \cdot \nabla_y \delta\widetilde{\mathbf{u}}(\rho;\delta\rho) \cdot \nabla_y \chi_m^{(rs)}(\rho) \\
& + \mathbf{E}_{ij} \cdot \mathbf{A}_m(\mathbf{F}_m,\rho) \cdot \nabla_y \delta\chi_m^{(rs)}(\rho) \\
& + \delta\mathbf{P}_m(\mathbf{F}_m,\rho;\delta\rho) \cdot \nabla_y \hat{\widetilde{\mathbf{u}}}_m + \mathbf{A}_m(\mathbf{F}_m,\rho) \cdot \nabla_y \delta\widetilde{\mathbf{u}}(\rho;\delta\rho) \cdot \nabla_y \hat{\widetilde{\mathbf{u}}}_m \\
& + \delta\mathbf{A}_m(\mathbf{F}_m,\rho;\delta\rho) \cdot \nabla_y \chi_m^{(rs)}(\rho) \cdot \nabla_y \mathbf{z} + \mathbf{A}_m(\mathbf{F}_m,\rho) \cdot \nabla_y \delta\chi^{(rs)}(\rho;\delta\rho) \cdot \nabla_y \mathbf{z} \\
& + \frac{\partial \mathbf{A}_m(\mathbf{F}_m,\rho)}{\partial \mathbf{F}_m} \cdot \nabla_y \delta\widetilde{\mathbf{u}}(\rho;\delta\rho) \cdot \nabla_y \chi_m^{(rs)}(\rho) \cdot \nabla_y \mathbf{z} \Bigg)\, dv
\end{aligned} \tag{A.8}$$

A.5. Periodic Boundary Relations Derivations

In this section, how the periodic boundary conditions are derived based on the master-slave relations and node numbering scheme described in Chapter 5 are explained in detail.

A.5.1. Corner Node Relations

The displacements of the nodes $\mathbf{U}^{(2)}$, $\mathbf{U}^{(3)}$, $\mathbf{U}^{(4)}$ can be expressed in terms of $\mathbf{U}^{(1)}$ and $\mathbf{F}_M$ using the following relations.

$$\mathbf{U}^{(2)} = \mathbf{U}^{(1)} + (\mathbf{F}_M - \mathbf{I}) \cdot \mathbf{L}_1 \tag{A.9}$$

$$\mathbf{U}^{(3)} = \mathbf{U}^{(1)} + (\mathbf{F}_M - \mathbf{I}) \cdot (\mathbf{L}_1 + \mathbf{L}_2) \tag{A.10}$$

$$\mathbf{U}^{(4)} = \mathbf{U}^{(1)} + (\mathbf{F}_M - \mathbf{I}) \cdot \mathbf{L}_2 \tag{A.11}$$

Eq.(A.9), Eq.(A.10) and Eq.(A.11) can be combined in a single matrix equation,

as follows.

$$\begin{bmatrix} \mathbf{U}^{(2)} \\ \mathbf{U}^{(3)} \\ \mathbf{U}^{(4)} \end{bmatrix} = \begin{bmatrix} \mathbf{I} \\ \mathbf{I} \\ \mathbf{I} \end{bmatrix} \cdot \mathbf{U}^{(1)} + \begin{bmatrix} \mathbf{I} & \mathbf{0} \\ \mathbf{I} & \mathbf{I} \\ \mathbf{0} & \mathbf{I} \end{bmatrix} \begin{bmatrix} (\mathbf{F}_M - \mathbf{I}) \cdot \mathbf{L}_1 \\ (\mathbf{F}_M - \mathbf{I}) \cdot \mathbf{L}_2 \end{bmatrix} \tag{A.12}$$

A.5.2. Edge Node Relations

The displacements of the nodes on the edges $\mathbf{E}^{(3)}$ and $\mathbf{E}^{(4)}$ can be expressed in terms of the nodes on the edges $\mathbf{E}^{(1)}$, $\mathbf{E}^{(2)}$ and the corner nodes, using the following relations.

$$\mathbf{E}^{(3)} = \mathbf{E}^{(1)} + (\mathbf{F}_M - \mathbf{I}) \cdot \mathbf{L}_2 \tag{A.13}$$

$$\mathbf{E}^{(4)} = \mathbf{E}^{(2)} + (\mathbf{F}_M - \mathbf{I}) \cdot \mathbf{L}_1 \tag{A.14}$$

Eq.(A.13) and Eq.(A.14) can be expressed in a single matrix equation as follows

$$\begin{bmatrix} \mathbf{E}^{(3)} \\ \mathbf{E}^{(4)} \end{bmatrix} = \begin{bmatrix} \mathbf{I} & \mathbf{0} \\ \mathbf{0} & \mathbf{I} \end{bmatrix} \begin{bmatrix} \mathbf{E}^{(1)} \\ \mathbf{E}^{(2)} \end{bmatrix} + \begin{bmatrix} \mathbf{0} & \mathbf{I} \\ \mathbf{I} & \mathbf{0} \end{bmatrix} \begin{bmatrix} (\mathbf{F}_M - \mathbf{I}) \cdot \mathbf{L}_1 \\ (\mathbf{F}_M - \mathbf{I}) \cdot \mathbf{L}_2 \end{bmatrix} \tag{A.15}$$

A.5.3. System Matrix Reduction Using Master-Slave Relations

The virtual energy expression involving global stiffness matrix is as follows

$$\begin{bmatrix} \delta\mathbf{U}_M^T & \delta\mathbf{U}_S^T & \delta\mathbf{U}_I^T \end{bmatrix} \begin{bmatrix} \mathbf{K}_{MM} & \mathbf{K}_{MS} & \mathbf{K}_{MI} \\ \mathbf{K}_{SM} & \mathbf{K}_{SS} & \mathbf{K}_{SI} \\ \mathbf{K}_{IM} & \mathbf{K}_{IS} & \mathbf{K}_{II} \end{bmatrix} \begin{bmatrix} \mathbf{U}_M \\ \mathbf{U}_S \\ \mathbf{U}_I \end{bmatrix} \tag{A.16}$$

and the virtual energy expression involving global force matrix is as follows

$$\begin{bmatrix} \delta\mathbf{U}_M^T & \delta\mathbf{U}_S^T & \delta\mathbf{U}_I^T \end{bmatrix} \begin{bmatrix} \mathbf{F}_M \\ \mathbf{F}_S \\ \mathbf{F}_I \end{bmatrix} \tag{A.17}$$

Taking the master-slave relation, i.e., $\mathbf{U}_S = \mathbf{D}_1\mathbf{U}_M + \mathbf{H}$, and applying variation

yields

$$\delta \mathbf{U}_S = \mathbf{D}_1 \cdot \delta \mathbf{U}_M \tag{A.18}$$

$$\delta \mathbf{U}_S^T = \delta \mathbf{U}_M^T \cdot \mathbf{D}_1^T \tag{A.19}$$

Substituting equations Eq.(A.18) and Eq.(A.19) into Eq.(A.16) gives

$$\begin{bmatrix} \delta \mathbf{U}_M^T & \delta \mathbf{U}_M^T \cdot \mathbf{D}_1^T & \delta \mathbf{U}_I^T \end{bmatrix} \begin{bmatrix} \mathbf{K}_{MM} & \mathbf{K}_{MS} & \mathbf{K}_{MI} \\ \mathbf{K}_{SM} & \mathbf{K}_{SS} & \mathbf{K}_{SI} \\ \mathbf{K}_{IM} & \mathbf{K}_{IS} & \mathbf{K}_{II} \end{bmatrix} \begin{bmatrix} \mathbf{U}_M \\ \mathbf{D}_1 \mathbf{U}_M + \mathbf{H} \\ \mathbf{U}_I \end{bmatrix} \tag{A.20}$$

After rearranging Eq.(A.20), Eq.(A.16) takes the form

$$\begin{bmatrix} \delta \mathbf{U}_M^T & \delta \mathbf{U}_I^T \end{bmatrix} \left(\left[\begin{array}{c|c} \mathbf{K}_{MM} + \mathbf{K}_{MS}\mathbf{D}_1 + & \mathbf{K}_{MI} + \mathbf{D}_1^T \mathbf{K}_{SI} \\ \mathbf{D}_1^T \mathbf{K}_{SM} + \mathbf{D}_1^T \mathbf{K}_{SS} \mathbf{D}_1 & \\ \hline \mathbf{K}_{IM} + \mathbf{K}_{IS}\mathbf{D}_1 & \mathbf{K}_{II} \end{array} \right] \left[\begin{array}{c} \mathbf{U}_M \\ \hline \mathbf{U}_I \end{array} \right] + \left[\begin{array}{c} (\mathbf{K}_{MS} + \mathbf{D}_1^T \mathbf{K}_{SS}) \cdot \mathbf{H} \\ \hline \mathbf{K}_{IS} \cdot \mathbf{H} \end{array} \right] \right) \tag{A.21}$$

Following the same procedure for the global force matrix gives the following result.

$$\begin{bmatrix} \delta \mathbf{U}_M^T & \delta \mathbf{U}_I^T \end{bmatrix} \begin{bmatrix} \mathbf{F}_M + \mathbf{D}_1^T \mathbf{F}_S \\ \mathbf{F}_I \end{bmatrix} \tag{A.22}$$

A.6. Helmholtz Filter

Using the Helmholtz filter, the filtered relative densities can be calculated by solving the following equation for $\widetilde{\rho}$. In the following part, the steps to calculate the sensitivities with respect to the unfiltered densities will be explained.

$$\underbrace{\int_{\Omega_m} (\nabla w \cdot r^2 \nabla \widetilde{\rho} + w \cdot \widetilde{\rho}) \, dV}_{A(\widetilde{\rho}(\rho), w)} = \underbrace{\int_{\Omega_m} w \cdot \rho \, dV}_{B(\rho, w)} \tag{A.23}$$

Consider a response function $\theta(\rho)$, using Eq.(A.23) it can be rewritten as

$$\theta(\rho) = \widetilde{\theta}(\widetilde{\rho}(\rho)) - \underbrace{\Big(A(\widetilde{\rho}(\rho), w) - B(\rho, w)\Big)}_{=0} \tag{A.24}$$

Taking the variation of $\theta(\rho)$ gives

$$\delta\theta(\rho; \delta\rho) = \frac{\partial\widetilde{\theta}}{\partial\widetilde{\rho}}\delta\widetilde{\rho} - \Big(\frac{\partial A}{\partial\widetilde{\rho}}\delta\widetilde{\rho} - \frac{\partial B}{\partial\rho}\delta\rho\Big) \tag{A.25}$$

The sensitivities $\delta\theta(\widetilde{\rho})$ have already been calculated using relations given in Chapter 4. Thus it is known that

$$\delta\theta(\widetilde{\rho}) = \frac{\partial\widetilde{\theta}}{\partial\widetilde{\rho}}\delta\widetilde{\rho} \tag{A.26}$$

Substituting above equation into Eq.(A.25) gives

$$\delta\theta(\rho; \delta\rho) = \int_{\Omega_m} w \cdot \delta\rho \; dV - \Big(\frac{\partial A}{\partial\widetilde{\rho}}\delta\widetilde{\rho} - \frac{\partial\widetilde{\theta}}{\partial\widetilde{\rho}}\delta\widetilde{\rho}\Big) \tag{A.27}$$

If the second part of Eq.(A.27) can be equated to zero by finding the appropriate w, the sensitivities in terms of the unfiltered densities can be obtained. Thus, the following equation must be solved.

$$\Big(\frac{\partial A}{\partial\widetilde{\rho}}\delta\widetilde{\rho} - \frac{\partial\widetilde{\theta}}{\partial\widetilde{\rho}}\delta\widetilde{\rho}\Big) = 0 \tag{A.28}$$

The variation of A can be found by taking the directional derivative of A in the direction of $\delta\widetilde{\rho}$

$$\begin{aligned}
DA[\delta\widetilde{\rho}] &= \delta A \\
&= \frac{\partial A}{\partial\widetilde{\rho}}\delta\widetilde{\rho} \\
&= \frac{d}{d\epsilon}\left[\int_{\Omega_m}\Big(r^2\nabla w \cdot \nabla(\widetilde{\rho} + \epsilon\cdot\delta\widetilde{\rho}) + w\cdot(\widetilde{\rho} + \epsilon\cdot\delta\widetilde{\rho})\Big)\,dV\right]_{\epsilon=0} \\
&= \frac{d}{d\epsilon}\left[\int_{\Omega_m}\Big(r^2\nabla w \cdot (\nabla\widetilde{\rho} + \epsilon\cdot\nabla\delta\widetilde{\rho}) + (w\cdot\widetilde{\rho} + \epsilon\cdot w\cdot\delta\widetilde{\rho})\Big)\,dV\right]_{\epsilon=0} \\
&= \int_{\Omega_m}\Big(r^2\nabla w\cdot\nabla\delta\widetilde{\rho} + w\cdot\delta\widetilde{\rho}\Big)\,dV
\end{aligned} \tag{A.29}$$

Substituting this expression into Eq.(A.28) gives

$$\int_{\Omega_m} (r^2 \nabla w \cdot \nabla \delta\widetilde{\rho} + w \cdot \delta\widetilde{\rho})\, dV - \delta\theta(\widetilde{\rho}) = 0 \tag{A.30}$$

Using finite element formulation it is possible to write $\delta\theta(\widetilde{\rho})$ in terms of nodal quantities

$$\delta\theta(\widetilde{\rho}) = [\delta\widetilde{\rho}]^T \cdot [\widetilde{\mathbf{S}}] \tag{A.31}$$

Eq.(A.30) can also be written in finite element formulation as follows

$$[\delta\widetilde{\rho}]^T \cdot \Big(\sum_e \int_{\Omega_e} r^2 [\mathbf{B}]^T [\mathbf{B}][\mathbf{w}] + [\mathbf{N}]^T [\mathbf{N}][\mathbf{w}]\, dV - \widetilde{\mathbf{S}} \Big) = 0 \tag{A.32}$$

Using the arbitrariness of $[\delta\widetilde{\rho}]^T$, and rearranging gives

$$\underbrace{\Big(\sum_e \int_{\Omega_e} r^2 [\mathbf{B}]^T [\mathbf{B}] + [\mathbf{N}]^T [\mathbf{N}]\, dV \Big)}_{[\mathbf{K}]} \cdot [\mathbf{w}] = [\widetilde{\mathbf{S}}] \tag{A.33}$$

After solving this system of equations for adjoint field $[\mathbf{w}]$, and substituting into Eq.(A.27) and rewriting in the finite element formulation gives

$$[\delta\rho]^T \cdot [\mathbf{S}] = [\delta\rho]^T \cdot \sum_e \int_{\Omega_m} [\mathbf{N}][\mathbf{w}]\, dV \tag{A.34}$$

Thus, the nodal sensitivities of the unfiltered densities can be found by the following expression.

$$[\mathbf{S}] = \sum_e \int_{\Omega_m} [\mathbf{N}][\mathbf{w}]\, dV \tag{A.35}$$

APPENDIX B

Julia Code

The computer programs developed and used throughout this thesis can be accessed from the links provided below.

Julia Package for Nonlinear Elastic Microstructural (Topology) Optimization [NEMOpt.jl]: https://github.com/likemaestro/NEMOpt.jl

Julia Package for Linear Elastic Microstructural (Topology) Optimization [LEMOpt.jl]: https://github.com/likemaestro/LEMOpt.jl